TECHNISCHE UNIVERSITÄT MÜNCHEN

Fakultät für Chemie

Fachgebiet Physikalische Chemie

On Improvements of Sodium Manganese Oxide Materials as Sodium-Ion Battery Cathode

Nicolas Joachim Bucher

Vollständiger Abdruck der von der Fakultät für Chemie der Technischen Universität München zur Erlangung des akademischen Grades eines

Doktors der Naturwissenschaften

Genehmigten Dissertation.

Vorsitzende(r): Univ.-Prof. Dr. U. K. Heiz

Prüfer der Dissertation:

1. Univ.-Prof. Dr. M.-E. Michel-Beyerle (i. R.)

2. Univ.-Prof. Dr. F. E. Kühn

3. Prof. M. Srinivasan, Ph.D.
   Nanyang Technological University Singapore

Die Dissertation wurde am 26.11.2015 bei der Technischen Universität München eingereicht und durch die Fakultät für Chemie am 11.01.2016 angenommen.

Table of Contents

1 Abstract 1

2 Introduction 2

2.1 Primary Battery Systems 2

2.1.1 Zinc-Carbon (Zn-Mn) and Alkaline Battery (Zn-OH)[1–4] 3

2.1.2 Metal-Air Battery: Aluminium-Air Battery (Al-Air/O_2)[6–8] 3

2.2 Secondary Battery Systems 5

2.2.1 Lead-Acid Battery (Pb-Acid)[14,15] 6

2.2.2 Rechargeable Alkaline Battery: Nickel-Metal Hydride (Ni-MH) Battery[16–21] 7

2.2.3 Insertion-Type Battery with Organic Electrolyte[5,11,23–25] 8

2.3 Sodium-Ion Battery 10

2.3.1 Cathode Materials for NIBs 13

2.4 Improving P2-type Na_xMnO_2 - Motivation and Approaches 18

3 Methods 20

3.1 X-ray Diffraction[94–102] 20

3.1.1 Working Principle 20

3.1.2 Laboratory X-ray Source 21

3.1.3 Synchrotron as X-ray Source 23

3.2 Electron Microscopy and Spectroscopic Methods[103–107] 24

3.2.1 Scanning Electron Microscopy 25

3.2.2 Transmission Electron Microscopy 26

3.2.3 Energy Dispersive Spectroscopy (EDS) and X-ray Fluorescence (XRF)[107–110] 27

3.2.4 Inductively Coupled Plasma Optical Emission Spectroscopy (ICP-OES)[111,112] 28

3.3 Viscosity Measurements[113] 28

3.4 Thermogravimetric Analysis[114,115] 29

3.5 Electrochemical Measurements 29

3.5.1 Electrochemical Cell[116] ... 29
3.5.2 Electrode Preparation and Coin-Cell Assembly ... 30
3.5.3 Galvanostatic Cycling[116,118] ... 31
3.5.4 Galvanostatic Intermittent Titration Technique[119–123] ... 33
3.5.5 Linear Sweep- and Cyclic Voltammetry (LSV & CV)[116,118,123,125] ... 35
3.5.6 Electrochemical Impedance Spectroscopy (EIS)[118,126] ... 36
4 Results ... 38
4.1 Combustion-Synthesised Sodium Manganese (Cobalt) Oxides as Cathodes for Sodium-Ion Batteries ... 39
4.2 Layered Na_xMnO_{2+z} in Sodium-Ion Batteries – Influence of Morphology on Cycle Performance ... 49
4.3 Electrochemical Cell for *in operando* X-ray Diffraction Measurements on a Conventional X-ray Diffractometer ... 62
4.4 P2-$Na_xCo_yMn_{1-y}O_2$ (y = 0, 0.1) as Cathode Materials in Sodium-Ion Batteries – Investigation of Doping and Morphology to Enhance Cycling Stability ... 68
4.5 A Novel Ionic Liquid for Li-Ion Batteries – Uniting the Advantages of Guanidinium and Piperidinium Cations ... 90
5 Conclusion ... 101
6 References ... 104
7 List of Acronyms ... 113
8 List of Figures ... 115
9 List of Tables ... 116
10 List of Publications ... 117

1 Abstract

Mainly due to potential cost advantages sodium-ion batteries have the potential to become an alternative to lithium-ion batteries. In this work strategies to improve cycling stability of the cathode material P2-Na_xMnO_2 are presented. Cobalt-doping on the order of 10% leads to a suppression of structural changes, resulting in improved cyclability, and enhanced Na^+ diffusion kinetics. Moreover, capacity and cyclability can be increased by an optimization of the morphology. A combination of both strategies leads to a material with comparably best discharge capacity and cycling stability.

Natrium-Ionen-Batterien gelten hauptsächlich aufgrund potenzieller Kostenvorteile als mögliche Alternative zu Lithium-Ionen-Batterien. Diese Arbeit beschreibt Strategien zur Verbesserung der Zyklenstabilität von P2-Na_xMnO_2 als Kathodenmaterial. Eine ~10%ige Cobalt-Substitution bewirkt eine Unterdrückung von Strukturumwandlungen und eine Verbesserung der Na^+-Diffusion. Des Weiteren kann die Kapazität und Zyklenstabilität durch eine Optimierung der Morphologie verbessert werden. Die Kombination beider Strategien vereint die jeweiligen Vorteile und führt zu einem Material mit hoher Kapazität und vergleichsweise bester Zyklenstabilität.

This doctoral thesis is the cumulative integration of the scientific publications resulting from my work as a research associate at TUM CREATE. After a brief overview of different battery technologies, sodium-ion batteries are described in detail, followed by a description of the main experimental methods employed in this work. Subsequently, my four scientific publications, as well as one further publication in which my contribution was crucial, are presented. The thesis is concluded with a discussion of the presented results.

2 Introduction

The aspiration to have access to energy in the form of electricity, independently of the electrical grid, has sparked a variety of inventions and was the basis for several leaps with regard to the development of novel technologies in the field of energy storage. The dominant principle for portable energy storage devices is electrochemical energy storage, for which batteries are the most prominent example. Here, energy is stored in the active material of a battery, and energy, in the form of electricity is provided as a result of electrochemical reactions within the cell (Figure 1). In the course of these reactions, the active materials are reduced and oxidised, which means they take up or release electrons. These electrons 'transfer' from one side of the battery to the other side via an external circuit. Charge neutrality of the system is ensured by ionic charge carrier in the electrolyte. While the electrons pass through this external circuit, physical work is performed, and can be used to power a variety of devices. By convention, the negative electrode is typically referred to as anode (oxidation during discharge), and the positive electrode as cathode (reduction during discharge). Naturally, the amount of energy that is stored in a battery is limited – when all redox-active centres in the active material have reacted, the system cannot provide further energy. Depending on the nature of the electrochemically active material, the battery can either be restored to its charged state (secondary battery), or its material is depleted and cannot be used anymore to provide electrical currents (primary battery). In the following, the most prominent types of single use primary and rechargeable secondary systems will be shortly portrayed.

2.1 Primary Battery Systems

Batteries that cannot be recharged are called primary batteries. The electrochemical reactions taking place during discharge are either fully or partially irreversible, or the provided energy to bring the system to its initial status cannot be provided by simply applying an external voltage. To restore the materials to their initial states most of them have to be recycled in an "external" chemical process, are incinerated or go into landfill after hazardous constituents are either removed or contained.

2.1.1 Zinc-Carbon (Zn-Mn) and Alkaline Battery (Zn-OH)[1–4]

The working principle of the first historical primary battery, the Leclanché-element (1866)[5], is still the basis for Zn-Mn and Zn-OH batteries today. Together, they still contribute the main share to the global battery community market (30.5% for Zn-Mn and 60.3% for Zn-OH with respect to tonnes sold in 2006)[3]. Both are widely used for simple applications like radios, remote controls and other objects for which small quantities of energy are sufficient. The alkaline battery, which was commercialised in 1949[2], is often favoured over the Zn-Mn battery due to its higher capacity and durability. The underlying chemical reactions in a Zn-OH battery are as follows:

Cathodic reaction

$$2MnO_2 + 2H_2O + 2e^- \rightarrow 2MnOOH + 2OH^-$$ $E^0 = 0.12$ V *vs.* SHE (SHE: Standard hydrogen electrode)

Anodic reaction

$$Zn + 4OH^- \rightarrow [Zn(OH)_4]^{2-} + 2e^-$$ $E^0 = -1.33$ V *vs.* SHE

Overall cell reaction

$$Zn + 2MnO_2 + 2H_2O + 2OH^- \rightarrow [Zn(OH)_4]^{2-} + 2MnOOH$$

Even though the calculated potential from these half-cell reactions, *i.e.* the difference between the cathodic and the anodic potential, gives a working potential of 1.45 V, the actual potential of commercial batteries is ~1.6 V. This deviation is due to the fact that the reactions shown above are only a simplification of the more complex cell chemistry. Depending on concentration effects and the state of charge, further reactions can occur which increase the potential of the cell.

2.1.2 Metal-Air Battery: Aluminium-Air Battery (Al-Air/O_2)[6–8]

Metal-air batteries are classified by the use of metal as an anode and the oxygen (which is usually obtained from the air) as cathode. Metal-air batteries have always been a desirable approach to increase energy density as the cathode material basically is the oxygen taken from the air and could potentially save up to 65 % of the battery weight.[9] Therefore, the energy densities achieved with a metal-air battery is one of the highest discussed (For Al-O_2: 1 - 2 kWh kg^{-1}) and can be easily several times higher than a common lithium-ion battery technology, which is between 100 – 200 Wh kg^{-1}.[5] For comparison the theoretical energy density of gasoline is 13 kWh kg^{-1}

(practical: 1.7 kWh kg^{-1}). Li-Air, with a theoretical energy density of 12 kWh kg^{-1} would be the prime candidate of the metal – air batteries to replace gasoline.[8,10] However, due to many challenges in the design and chemistry, no viable prototype is available as of now. Whereas Al-Air systems on the other hand is a serious candidate to compete with fossil-fuel based combustion engines, with a theoretical voltage 2.75 V and theoretical energy density of the Al reaction of 8.1 kWh kg^{-1} and a practical achievable energy density of the battery of 1.3 kWh kg^{-1} (2 kWh kg^{-1} projected).[6,10] Although the standard potential of Li (-3.04 V *vs*. SHE)[11] is much lower than Al (-1.68 V *vs*. SHE) the ability to transfer three electrons by a smaller atomic/ionic radius gives aluminium the advantage of the higher charge density over lithium. The first Al-O_2 system was demonstrated in the 1960`s by Zaromb and Trevethan.[7] Main disadvantages are that the battery is non-rechargeable – therefore a primary battery and that high self-discharge occurs due to anode corrosion. Nevertheless, it was shown in literature that with a proper recycling chain the life-cycle cost could potentially be limited to only 114% than that of internal combustion engines.[7] Therefore, owing to the low cost of the used materials, environmentally benignity of all components and the recyclable products, this technology is considered promising. The underlying chemical reaction in an alkaline solution is as follows:

Cathodic reaction

$$O_2 + 2H_2O + 4e^- \rightarrow 4OH^-$$ E^0 = 0.4 V *vs*. SHE

Anodic reaction

$$Al + 3OH^- \rightarrow Al(OH)_3 + 3e^-$$ E^0 = -2.35 V *vs*. SHE

Overall cell reaction

$$4Al + 3O_2 + 6H_2O \rightarrow 4Al(OH)_3$$

The theoretical voltage from this reaction is 2.75 V. However, practically the cell operates at potentials of 1.2 – 1.6 V.[7] This is due to layers of aluminium oxide on the electrode, which results in an internal resistance and causes a delay in reaching a steady voltage. In addition corrosion of the aluminium leads to the incomplete utilisation of the metal and evolution of hydrogen. Various approaches to address these two issues, the electrolyte and the anode metal are investigated. Using aluminium alloys with small amounts (50 – 1000 ppm) of *e.g.* magnesium, calcium, zinc, tin, indium and gallium has been shown to supress the oxide layer formation and hinder

the corrosion mechanism (so-called activation).[7,8] The electrolytes are typically aqueous alkaline solutions. Saline solutions are also used, with the anode discharge reaction in saline lowered to E^0 = -1.66 V.[7] Both electrolytes have been tested with various additives including metal oxides (CaO, ZnO, to Na_2SnO_3) and salts like $CaCl_2$, sodium citrate for alkalines; phosphate, sulphate, fluoride and organic salt additives for brine solutions.[7,8]

Given the high energy and the low volume requirement of the battery, the Al-air system has found its way into several applications which require a long lasting energy supply and a light weight device. Thus, it can be encountered in military applications, such as field-portable batteries for remote applications. It is mostly transported in a 'dry state', and the aqueous solution is only added on demand. It can also be mechanically recharged, by adding new aluminium metal sheets and water to the system. Most of the batteries on the market are designed as reserve batteries. Underwater vehicles or space application have been using this technology as well, taking the oxygen from pressurised tanks or cryogenic oxygen, respectively.[7,8] In 2014 the technology received renewed attention due to a press releases by the Phinergy and Alcoa company, claiming a range of 1000 miles (~1600 km) for electric vehicles with a 100 kg battery.[12] a fifth of the battery weight installed in a Tesla Type S and a range extension by a factor of 4.

2.2 Secondary Battery Systems

In contrast to primary systems, batteries that can be recharged are coined secondary batteries. In secondary batteries, the chemical reactions of the active materials during discharge can be reversed by applying an electrical current from an external source. Thus, previously oxidised materials are reduced, and previously reduced materials are oxidised. Hence, the energy is 'fed' back into the system (neglecting losses as a consequence of parasitic side reactions *etc.*) so that the battery can be used again to provide electric charge. However, the electrodes that are involved in this process act not only as a mediator for charge transfer as they are in fuel cells, but undergo chemical reactions. As a consequence, they tend to degrade over time, which limits the cycle number (*i.e.* number of charge-discharge reactions) for which they can be used. This is one reason for research on different types of materials. Table 1 gives an overview of the most important battery chemistries. In the following chapters, the most prominent examples are briefly outlined.

Battery		Discharge cell reaction	Energy density / Wh kg^{-1}
(+)	(–)		
Acidic Aqueous Solution			
PbO_2	Pb	$Pb + PbO_2 + 2H_2SO_4 \rightarrow 2PbSO_4 + 2H_2O$	170
Alkaline Aqueous Solutions			
NiOOH	Cd	$2NiOOH + 2H_2O + Cd \rightarrow 2Ni(OH)_2 + Cd(OH)_2$	217
NiOOH	Fe	$2NiOOH + 2H_2O + Fe \rightarrow 2Ni(OH)_2 + Fe(OH)_2$	267
NiOOH	Zn	$2NiOOH + 2H_2O + Zn \rightarrow 2Ni(OH)_2 + Zn(OH)_2$	341
NiOOH	H_2	$2NiOOH + H_2 \rightarrow 2Ni(OH)_2$	387
MnO_2	Zn	$2MnO_2 + H_2O \rightarrow 2Ni(OH)_2$	317
O_2	Al	$4Al + 6H_2O + 3O_2 \rightarrow 4Al(OH)_3$	2815
O_2	Fe	$2Fe + 2H_2O + O_2 \rightarrow 2Fe(OH)_2$	764
O_2	Zn	$2Zn + 2H_2O + O_2 \rightarrow 2Zn(OH)_2$	888
Flow			
Br_2	Zn	$2Zn + Br_2 \rightarrow ZnBr_2$	436
Cl_2	Zn	$2Zn + Cl_2 \rightarrow ZnCl_2$	833
$(VO_2)_2SO_4$	VSO_4	$(VO_2)_2SO_4 + 2HVSO_4 + 2H_2SO_4 \rightarrow 2VOSO_4 + V_2(SO_4)_3 + 2H_2O$	114
Molten Salt			
S	Na	$2Na + 3S \rightarrow Na_2S_3$	760
$NiCl_2$	Na	$2Na + NiCl_2 \rightarrow 2NaCl + Ni$	790
FeS_2	LiAl	$4LiAl + FeS_2 \rightarrow 2Li_2S + 4Al + Fe$	650
Organic Lithium Solution			
$LiCoO_2$	Li–C	$Li(y + x)C_6 + Li(1 - (y - x)CoO_2 \rightarrow LiyC_6 + Li(1 - y)CoO_2$	320*

Table 1. Overview of different battery chemistries and their theoretical energy density.[13] (*Calculated for a maximum of x = 0.5; y = 0)

2.2.1 Lead-Acid Battery (Pb-Acid)[14,15]

The lead-acid battery, which was developed in 1859 by Gaston Planté, was the first rechargeable battery and is the oldest system for electrochemical energy storage that is still used commercially.[14] The basic electrochemical reactions of this battery type during discharge are as follows:[15]

Cathodic reaction

$PbO_2 + H_2SO_4 + 2H^+ + 2e^- \rightarrow PbSO_4 + 2H_2O$ E^0 = 1.6 V *vs.* SHE

Anodic reaction

$Pb + H_2SO_4 \rightarrow PbSO_4 + 2H^+ + 2e^-$ E^0 = -0.3 V *vs.* SHE

Overall cell reaction

$Pb + PbO_2 \rightarrow 2PbSO_4 + 2H_2O$

Its advantages are availability of raw materials and low cost. Thus, this technology is still being used for a wide range of applications, such as uninterruptible power sources (UPS-devices), starting/lighting/ignition power sources (*e.g.* a car battery), or for large-scale grid storage systems (10 MW/40 MW h).[14] Its inherent disadvantages are mainly based on concerns regarding toxicity of the materials that are used, namely lead and H_2SO_4. However, to alleviate these concerns, a reliable recycling chain is established that achieves recycling rates of up to 98%.[14] The main disadvantage in terms of performance is capacity loss over time, which is due to parasitic reactions like degassing (O_2 / H_2 evolution on the positive / negative electrode), corrosion, or, most importantly, the so-called sulfation. Sulfation describes the formation of a layer of large grains of $PbSO_4$ on the electrode surface, which effectively blocks the electrode, reduces the amount of active material and leads to a loss of contact. Current research successfully addresses this problem by incorporating carbon into the negative electrode, which improves both stability and capacity. Mechanistically, it is believed that carbon additives improve conductivity, inhibit the growth of large $PbSO_4$ crystals, facilitate electrolyte diffusion, and add a capacitive component which effectively transforms the battery into a hybrid device, leading to an increase in capacity.

2.2.2 Rechargeable Alkaline Battery: Nickel-Metal Hydride (Ni-MH) Battery[16–21]

Even though Ni-Cd batteries were developed much earlier than Ni-MH batteries, the latter have dominated the automotive sector since the 1990's due to their good trade-off between performance characteristics, such as capacity, power density or cycle life, better environmental tolerance, and cost. The metal hydride anode consists of a metal alloy mix with a huge hydrogen storage capability. A commonly used alloy is of the AB_5 - type where the A is a hydride forming rare earth metal (*e.g.* La, Ce, Nb, Pr) and B a non-hydrate forming alloy basis – mostly Nickel with dopants of *e.g.* Co, Al, Sn and Mn. The hydrogen storage capability of such an alloy is up to 5.5 H/AB_5.[20,21] Ni-MH batteries were developed with the intention of replacing the toxic Cd in Ni-Cd batteries with hydrogen; the storage mechanism is similar. In addition to decreasing toxicity, a better cycle life and higher specific capacity were achieved. The chemical reactions within a Ni-MH cell during discharge are as follows:

Cathodic reaction

$NiOOH + H_2O + e^- \rightarrow Ni(OH)_2 + OH^-$ E^0 = 0.49 V *vs.* SHE

Anodic reaction

$MH + OH^- \rightarrow M + H_2O + e^-$ E^0 = -0.83 V *vs.* SHE

Overall cell reaction

$NiOOH + MH \rightarrow (OH)_2 + M$

Particularly for hybrid electric vehicles, the Ni-MH-technology dominates over LIBs, Pb-acid and Ni-Cd chemistries, owing to its advantages in cycle life and safety. The mechanism of storing and releasing energy is based on shuffling OH-ions between a metal hydride (MH) and a NiO(OH) electrode. This working principle enables high power densities, eliminates the risk of dendrite formation, and provides a natural safeguard against over-(dis-)charging by recombining accruing O_2 and H_2 to H_2O within the cell.[17,18] Even though the cell voltage is only 1.32 V, Ni-MH-batteries are still considered to be a cheap and reliable option for electrochemical energy storage, based on their high energy density (350 Wh l^{-1} / 95 W h kg^{-1}), inexpensive electronic controls and low maintenance requirements.[22] Their main disadvantages are corrosion processes and degradation of MH - alloy particles on the negative electrode. Moreover, the rate of self-discharge is rather high compared to other battery chemistries.[16,19]

2.2.3 Insertion-Type Battery with Organic Electrolyte[5,11,23–25]

Insertion type batteries are based on the movement of a charge carrier in an organic electrolyte between two electrodes, *i.e.* the cathode and anode and the insertion of the redox active host structure. By using an organic instead of an aqueous electrolyte higher voltages can be achieved leading to a higher energy density. The most prominent examples for this class of energy storage devices are lithium-ion batteries (LIBs) and sodium-ion batteries (NIBs). Due to their light weight, high energy density and proven performance LIBs are the technology of choice for a variety of applications, such as portable consumer electronics, or batteries for electric vehicles. The first commercial LIB consists of $LiCoO_2$ as the cathode and graphite as the anode material. The chemical reaction during discharge is as follows:

Cathodic reaction

$Li_{(1-\frac{1}{2}x)}CoO_2 + \frac{1}{2}xLi^+ + \frac{1}{2}xe^- \rightarrow LiCoO_2$ | 0≤ x ≤ 1 E^0 = 3.8-4.2V *vs.* Li (~1 V *vs.* SHE)

Anodic reaction

$Li_{(x)}C_6 \rightarrow C_6 + xLi^+ + xe^-$ | 0≤ x ≤ 1 E^0 = ~0.2 V *vs.* Li (~-2.8 V *vs.* SHE)

Overall cell reaction

$2Li_{(1-\frac{1}{2}x)}CoO_2 + Li_{(x)}C_6 \rightarrow 2LiCoO_2 + C_6$ | 0≤ x ≤ 1

The advantage of LIBs over, for example, Ni-MH is that Li is the lightest and smallest of all metals and has a high thermodynamic potential. Therefore, Li-based batteries can provide a practical cell voltage of 3.6 V and gravimetric energy densities which are roughly twice the value of Ni-MH or Ni-Cd battery. Disadvantages of LIBs are the cost, the impeded performance at low temperature; the aging processes during storage and the fragility of the system *i.e.* the potential safety risks. In commercial batteries, graphite is used for most anode materials, and layered oxides as cathode. The electrolyte is typically carbonate based, *i.e.* various mixtures of ethylene carbonate, dimethyl carbonate, diethyl carbonate, propylene carbonate, *etc.*. The conducting salt is typically $LiPF_6$. In the charged state, the graphite is filled with Li-ions up to a ratio of LiC_6, and crystal sites in the cathode are (partially) vacated. Upon discharge, Li-ions vacate the graphite, accompanied by the release of an electron into the external circuit. Li-ions migrates through the electrolyte and separator to the cathode, where it is incorporated into the crystal structure of the cathode material. Concurrently, the electron in the outer circle also migrates to the cathode, performs work, and finally reduces the redox active centre in the cathode material, *e.g.* Co in $LiCoO_2$. This process can continue until either the graphite side is totally vacated of Li-ions, or every crystal structure site in the layered oxide is occupied. Ideally, the mass loading of anode and cathode, *i.e.* graphite and layered oxide are balanced such that the respective absolute capacities match, with a slight anode excess to avoid Li-dendrite formation. The incorporation of Li-ions into the crystal structure is reversible, so by applying an external current, the redox centre on the cathode side is oxidised again, and Li^+ vacates the crystal structure to migrate back to the graphite side.

For the related insertion-type batteries – the NIBs, the (de-)insertion processes are similar, even though the materials that are used as anode and cathode materials are different. This insertion process is presented in Figure 1 below. The specific advantages and disadvantages of Na-ion batteries will be elaborated on in the following chapter.

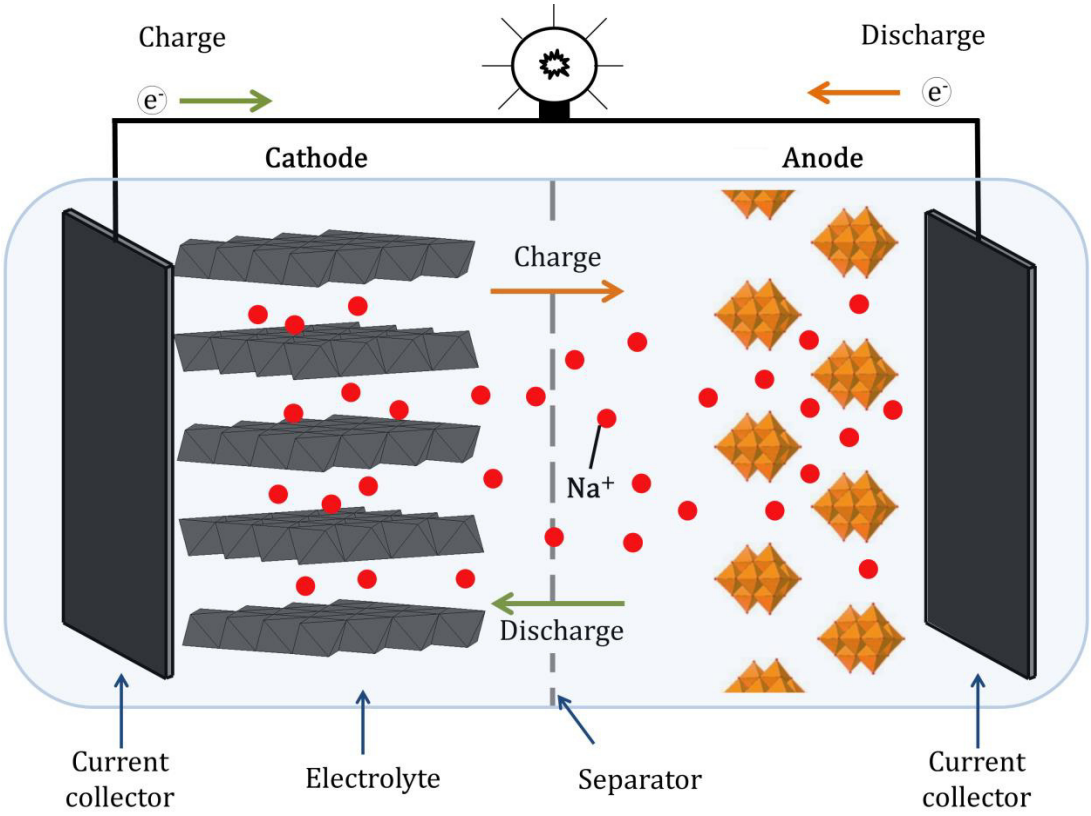

Figure 1. Schematic of an insertion type battery (cathode: Na_xMnO_2[26], anode: $Na_6V_{10}O_{28}$[27]). A prototype of this full-cell configuration has been published by Hartung *et. al.*.[27]

2.3 Sodium-Ion Battery

The working principle of NIBs is similar to that of LIBs (Figure 1). However, in contrast to LIBs, NIBs do not yet have a commercial market (apart from some minor start-up companies like Aquion and Faradion). After the first insertion-type materials were investigated in the 1970's,[28,29] research focused on intercalation of Li-ions into a variety of compounds, as Li-ion batteries promised higher gravimetric and volumetric capacities due to the smaller mass and size of Li-ions as compared to Na-ions. In addition, the standard electrode potential (*i.e.* the differential potential *vs.* SHE at standard conditions) for sodium is 0.33 V higher as for lithium, which, theoretically speaking, decreases the possibility to reach similar operating potentials for any NIB compared to LIBs.[11] Therefore, a huge variety of Li-insertion materials were discovered, synthesised, optimised and developed for commercial applications. With an increasing number of potential applications, and as a consequence of increasing

resource requirements, concern about the abundance, availability and price of Li-resources have manifested. As a consequence, research interest in Na-based batteries has increased tremendously in recent years, which is mirrored by the exponential increase of publications on this topic (Figure 2).

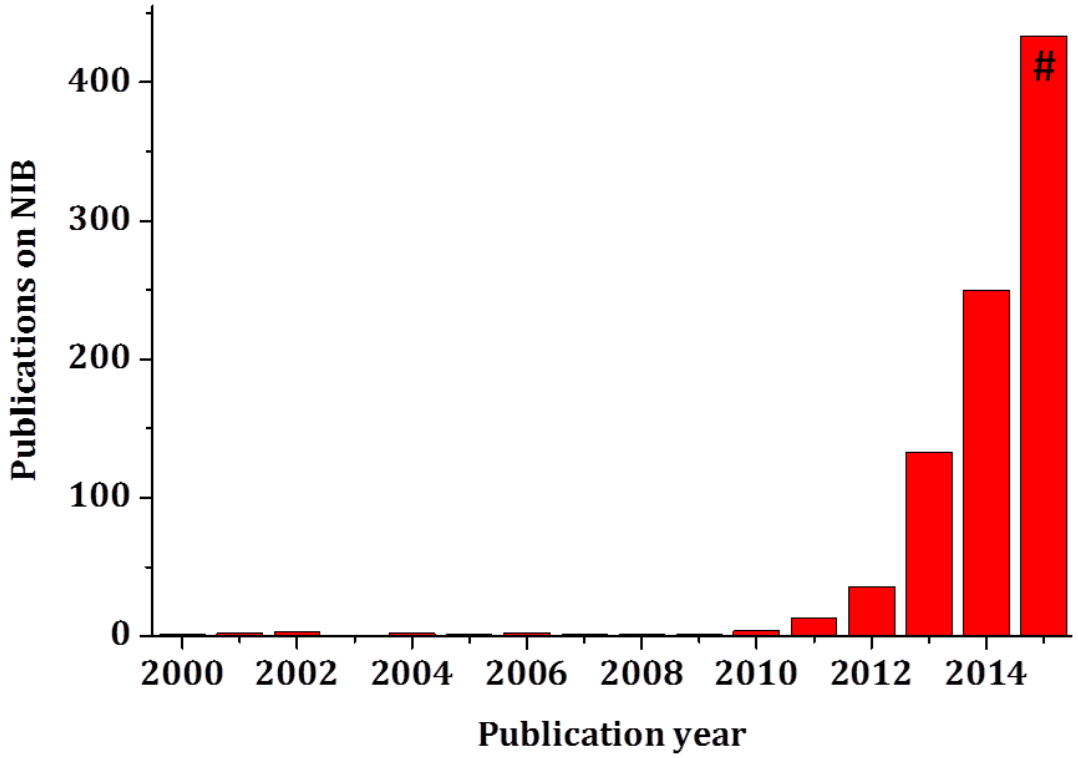

Figure 2. Number of publications for the specific search term: "sodium ion batter*" in the Scopus database, including truncation (*). # until date of search: 22.11.2015.

Sodium-resources, *i.e.* sodium-containing minerals or salts, are not only very abundant; they are also spread out globally. Sodium is the 6th most common element in the earth's crust, with an abundance of 26,000 ppm – Li, in contrast, ranks as the 33rd most common element, and its abundance is lower by a factor of ~1,000. [26] In addition, Na constitutes 1.1% (by mass) of ocean waters, approximately 10,000 more than Li.[30] Moreover, while sodium is found all around the globe, lithium resources are found mainly in Chile, Bolivia and Argentina. Out of these three, Chile holds the majority of mined output followed by Argentina; first large-scale mining operations in Bolivia are on the way. However, Lithium-mining has been shown to have severe environmental and social consequences.[31]

Even though Na^+ has the disadvantage of having a mass which is approximately three times the mass of Li^+, this does not linearly translate into lower gravimetric capacities for NIBs. For commercial applications, the crucial factor is the ratio of absolute capacity to the mass of the whole battery. As several other elements also contribute to the mass of the active material, the negative influence of the mass of Na^+ is reduced. $LiCoO_2$, for

example, which is a well investigated and commercialised material for LIBs, has a theoretical capacity of 274 mA h g^{-1} in LIBs assuming full reduction of Co^{4+} to Co^{3+}.[32] The Na-analogue, $NaCoO_2$, which has the same crystal structure, has a theoretical capacity of 235 mA h g^{-1} for Na^+-insertion, based on the same premise of a 1-e^--transfer for the Co-ion.[32] Thus, capacity of the electrode material is reduced by only 14%. This trend is similar for volumetric energy density. While the molar volume of Na is 18 $Å^3$ larger than the atomic volume of Li (39.3 $Å^3$ as compared to 21.3 $Å^3$), the difference in unit cell volume between $LiCoO_2$ and $NaCoO_2$ is only 5 $Å^3$ (37.3 $Å^3$ as compared to 32.3 $Å^3$). Thus, differences in performance as a result of different ionic radii and masses are negligible. In addition, sodium does not alloy with aluminium in the lower voltage region as it is the case for lithium (0.25 – 0.0 V *vs*. Li).[33–37] Therefore, Cu, which is typically used as current collector in NIBs, can be replaced with the lighter and cheaper aluminium. Particularly, it is worth noting, that the comparison between $LiCoO_2$ and $NaCoO_2$ is based on a material which is not only employed in commercial batteries, but has been researched and optimised for several decades. Other material classes, whose structural and chemical characteristics deviate from the layered alkali metal cobalt oxide, exhibit a better performance in NIBs than in LIBs.[38] In general, the structural variety of Na-compounds is more diverse than of Li-compounds.[30] Many naturally occurring minerals are based on Na-containing structure, and therefore, a significant amount of information on structural properties is readily available. The large variety comes partially with the larger ionic radius which enhances the flexibility of *e.g.* polyanionic and layered transition metal oxide materials.[32,39] Even for the ubiquitous LIB, certain electrode materials are synthesised via the Na-analogue as precursor.[40–42] The more stable Na-containing analogue is synthesised first, followed by a subsequent ion exchange.

However, apart from structural variety, the larger ionic radius of Na-ions provides some further inherent advantages. Viscosity is lower for Na-based electrolytes, and therefore ionic conductivity of the charge carrier is enhanced, as shown by Kuratani *et al.* for the case of propylene carbonate, which is also the basis of the electrolyte used in this work, and γ-butyrolactone.[43] This is due to a stronger attraction of Li-ions to the solvent molecules then Na-ions, leading to a larger cationic drifting volume. As a consequence, kinetics of ion transport in the electrolyte is improved when switching from Li- to Na-ions. This is particularly helpful for the rate capability of batteries, *i.e.* the ability of the system to provide high current rates. This kinetic advantage is substantiated by studies which show that, apart from enhanced transport characteristics in the electrolyte, diffusion is also enhanced for some materials within

the electrode. While Na^+-transport is hindered, as compared to Li^+-transport, in materials with an olivine crystal structure, the diffusion barrier for Na-ions is lower in the respective layered Co-oxide.[38] In addition to the promising kinetics in the electrolyte and in the electrode material, the charge transfer from the electrolyte to the electrode has also been shown to be advantageous for Na-based materials. Okoshi *et al.* showed that Na^+ has a smaller de-solvation energy than Li^+.[44] In the electrolyte, the charge carrier is coordinated by solvent molecules. Prior to insertion of the respective Li- or Na-ion into the crystal structure the charge carrier needs to be de-solvated. This de-solvation process can constitute a kinetic barrier, and depends on the strength of the interaction between the respective ion and the solvent molecules.[44–46] Na^+ is a weaker Lewis acid, than Li^+, which suggests weaker adhesive interaction with the solvent molecules. This has been confirmed by theoretical calculations for several organic solvents, including carbonates.[43] Thus, depending on the choice of suitable materials, Na-ions have a kinetic advantage throughout the complete process of ion transport in the electrolyte, ionic transfer from the electrolyte into the electrode material, and diffusion within the electrode materials.

Although various suitable materials for both NIB anodes and cathodes have been presented, a major challenge is still cycling stability. There are promising materials, both for anodes and cathodes, in terms of capacity, potentials *vs.* $Na|Na^+$, and cycling stability. However, finding suitable combinations of the amount of Na in the system (*i.e.* capacity), operating potential and stability, remains challenging, which calls for further research into suitable materials for NIBs.

2.3.1 Cathode Materials for NIBs

As the materials presented in this work are cathode materials, a short overview on other NIB cathodes reported in literature is given. The variety of cathode materials for NIBs is immense, and ranges from polyanionic compounds like transition metal phosphates or sulphides, organic polymer materials, Prussian blue analogues, to a variety of transition metal oxides. In the following chapters some example cathode materials are briefly portrayed. For a more in depth insight into the vast material pool the interested reader is directed to some excellent review literature [32,36,47–50].

Polyanionic Compounds. Polyanionic compounds have gained prominence LIB applications based on the success of the olivine $LiFePO_4$ (LFP). Therefore, this material class, comprising pyro-, carbo-, fluoro- or 'normal' phosphates and (fluoro-)sulphates have been studied in NIBs as well. For example, the Na analogue to the famous LFP, $NaFePO_4$, has been studied.[51–53] In this stoichiometry the thermodynamically stable

material allotrope is the maricite structure, which is a rather closed network and does not allow proper Na^+ movements.[38] To employ the iron phosphate as NIB material an anion exchange starting with the olivine type $LiFePO_4$ has been investigated.[51] However, the rather strong volume change leads to poor kinetic behaviour.

Incorporation of F-anions into the phosphate structure, as in Na_2FePO_4F, a layered structure was achieved with unexpected solid solution behaviour.[54] Even though kinetic properties were enhanced, reported capacities are still rather low even at a slow current rate. Incorporation of the strongly electronegative fluoride-ions is in general a good strategy to elevate the potential for the redox active material. This approach has been studied for various transition metal phosphate materials, like Na_2FePO_4F[54,55], $Na_{1.5}VPO_{4.8}F_{0.7}$[56] or representatives of the NASICON (Na^+ Super Ionic Conductor) structure, e.g. $Na_3V_2(PO_4)_2F_3$[57,58]. Although capacities are relatively low and electronic conductivity is poor, due to the elevated potential the theoretically obtainable energy density makes the materials attractive. Nanostructuring these materials appears to be a promising approach to enhance electronic conductivity of these materials and to extract their full potential.[59,60]

For sulphates, particularly Fe-based sulphates have shown one of the highest electrochemical redox potential for NIBs (~3.8V), although only low capacities were achieved (100 mA h g^{-1} at C-rate = C/20, 2.0 – 4.5 V; C-rated is defined under Chapter 3.5.3).[39,61,62]

Prussian Blue Analogues. In addition to phosphates and sulphates, various other materials have been investigated as positive electrodes in NIBs. These materials include different Prussian Blue analogues, which were first reported in 2012 by Lu *et al.*,[63] and can be subsumed under the formula $(Na_{2-x})M_A[M_B(CN_6)]_{1-y}\cdot zH_2O$.[36,63–67] The unique structure with its open framework provides the advantage of a relatively facile cation insertion/extraction as compared to layered materials or polyanionic structures. Up to now, most of the reports have shown a rather low capacity around ~100-120 mA h g^{-1} at slow C-rates. However, recently increased capacities were reported with an $Na_2Mn^{2+}[Mn^{2+}(CN)_6]$ material with a minimal amount of vacancy sites and an increased amount of Mn^{2+} in the synthesis process. The achieved performance was 209 mA h g^{-1} at C/5 and 167 mA h g^{-1} at 2C with a capacity retention of 75% after 100 cycles at an average voltage of 2.65 V.[66]

Oxide Compounds. Furthermore, a variety of oxides has been reported. Vanadium, for example, is known to have several stable oxidation states, and is therefore used in an oxide form to obtain high capacity materials. Orthorhombic V_2O_5 for example spurred attraction as a Na^+ host material in the 1980`s, but showed low initial coulombic efficiencies and only moderate stability.[68,69] A challenge for these materials is the rather low capacity retention over the course of cycling. This is attributed to the large amount of intercalated sodium which causes increased strain on the mostly layered structure.[70,71] A recent approach was to form a rather amorphous V_2O_5 layer a nickel foil via electrodeposition in order to increase the layer distance and thus enhance cyclability.[71] Several ternary alkali metal vanadium oxides have been reported as well, where the alkali metal often serves as both, a structural stabilisation ion between the layers and (partially) as source of the charge carrier ion.[72–75] Even though high capacities were achieved, cycling stability was insufficient. Moreover, the intrinsic problem of the vanadium based material is the high toxicity of the V^{5+}.

Layered Oxides. One of the most promising material classes is layered oxides with the chemical composition Na_xMeO_{2+z} (Me: transition metal). A huge variety of transition metals have been incorporated into this structure, including Mn, Co, Fe, Ni, Mg, V, Ti, Cr.[76–78] Even though compositional variety is immense, basic structural characteristics are similar. MO_6-octahedra form layers, which are separated by Na-ions. In general, this material class consists of several subgroups, which are defined on the basis of the coordination of the Na^+ between the layers. In addition to differences in the coordination of Na^+, the MO_6 layers can also be stacked differently. This is considered by incorporating the number of layers that needs to be included in the respective unit cell into the structural denomination (Figure 3). This classification was introduced by Delmas *et al.* in 1980.[78] In O3-type materials, for example, Na-ions between the layers are coordinated octahedrally and the unit cell consists of three MO_6-layeres, whereas in P2-type materials, two MO_6-layers and Na^+ with a prismatic coordination make up the unit cell (see Figure 3). The Na-ions on triangular prismatic sites can again be classified. If the triangles of the prism are formed by faces or edges of the MO_6-octahedra, Na^+ is denoted as Na_f or Na_e, respectively (f = face-sharing, e = edge-sharing).[79] The large Na-ions stabilise the prismatic sites in the structure; upon charge (*i.e.* Na^+-de-insertion) the MO_x – layers glide within the c-plane so that octahedral sites are formed. Thus, the P2 structure is transformed into the O2 structure during cycling.

However, a change from the P3/O3-phase to the P2 phase is not possible during reversible Na-(de-)insertion, because bonds between the transition metal and the oxygen need to be broken and reformed.[80] The NIB cathode materials presented in this work all belong to the class of P2-type layered oxides.

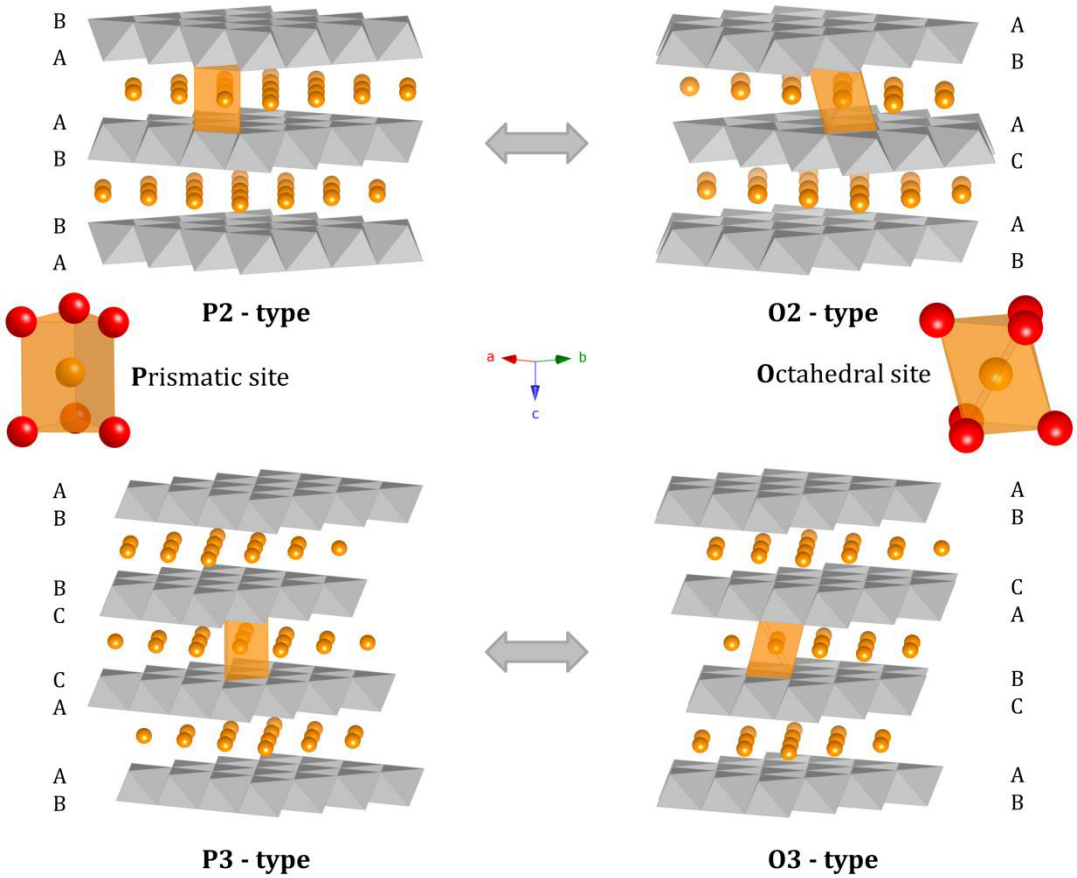

Figure 3. Schematic illustration of the different stacking types for MO_6 octahedra (grey). Orange spheres correspond to sodium atoms, red to oxygen atoms. For reasons of clarity only the Na_e are indicated.

Early research on Na^+-insertion into this material class dates back to 1980's, when the group of Delmas and Hagenmuller reported on the electrochemical insertion of Na^+ into Na_xCoO_2; studies on Na_xMnO_2 followed in 1985.[77,78,81–84] Initially, these compounds were mainly used as precursor for O2 Li^+-insertion compounds, which were synthesised by ion exchange.[40–42] P2-type materials have not been found among layered Li-intercalation compounds, as the lithium and transition metal ions are too small to form the trigonal prismatic sites between the MO_x-layers. Moreover, unlike for Li_xMnO_2 in LIBs, a transition from the layered to the spinel structure is thermodynamically and kinetically disfavoured for Na_xMnO_2. Especially in recent years, when research on NIBs gained momentum, a tremendous compositional variety of layered transition metal oxides has been investigated. However, probably due to structural reasons, all of them contain either Mn, Co, or Ti as oxide.[78,80] This is attributed to difficulties in obtaining the P2 phase with tetravalent ions. Due to initial

Na-deficiency in the P2-$Na_{0.66}MeO_2$ structure, transition metal ions with higher oxidation states are possible; however, they typically exhibit low capacities and operating potentials as in the case of P2-$Na_{2/3}Co_{2/3}Mn_{1/3}O_2$.[85] Thus, identifying suitable transition metal oxides and optimising their respective metal ratios is crucial in advancing this material class. Very recent research has focussed on incorporating several transition metals into one structure to combine the respective advantages of the individual constituents. Mn, for example, is chosen due to its high abundance and low price as well as its redox activity in an adequate voltage region. Moreover, it combines high capacities of up to 190 mA h g^{-1} with an acceptable cycling stability. Ni contributes a redox centre at high potentials; above 4.0 V *vs*. Na|Na^+. However, capacity is reduced to approximately 140 mA h g^{-1} (2.3 – 4.5 V, at C/100), and cycling stability suffers as well.[79,80,86] Promising results have been obtained by incorporating Fe into the structure, for example in P2-$Na_{2/3}[Fe_{1/2}Mn_{1/2}]O_2$[35,87,88] Capacity is increased, as compared to Ni-substitution, to 190 mA h g^{-1} (1.5 – 4.2 V, at 13 mA g^{-1}). Average potential, however, is lowered to 2.75 V *vs.* Na|Na^+. Still, the resulting energy densities exceed those of some commercial LIB cathode materials. In addition, Fe suppresses Na^+-ordering processes in the Na-layers during (de-)insertion, which has a positive effect on cycling stability, even though it is still far from being sufficient for commercial applications. Mg is another metal whose effect has been tested in this structure. Even though it increases cycling stability, capacity is reduced. Several studies on incorporating Mg into the P2-Na_xMeO_2 have demonstrated that the ratio between Mg and the baseline atom, which is mostly Mn, plays an important role in achieving a good compromise between capacity and cycling stability. [89–91] In general, increasing the Mg-content increases cycling stability, but decreases capacity.

Naturally, based on findings obtained by combining two transition metals, approaches to combine more than two transition metals in one structure have been presented recently, and proven rather successful. For example, P2-$Na_{0.5}Ni_{0.23}Fe_{0.13}Mn_{0.63}O_2$, delivers capacities of approximately 200 mA h g^{-1} (15 mA g^{-1}), with a capacity retention of roughly 150 mA h g^{-1} after 70 cycles. Probably due to polarisation effects, the capacity gets reduced drastically to roughly 120 and 100 mA h g^{-1} at C-rates of 1 and 2C, respectively (1C ≙ 143 mA g^{-1}; calculation based on 0.5 Na^+ per formula unit). The authors assume that this could be addressed by a modification of the morphology.[92] P2-$Na_xNi_{0.22}Co_{0.11}Mn_{0.66}O_2$, in comparison, has an elevated average discharge potential of 3.3 V when cycled between 4.3 – 2.1 V; capacity is lowered to 141 mA h g^{-1} (15 mA g^{-1}), depending on the annealing temperature.

At elevated C-rates of 1 and 2C (1C ≙ 123 mA g^{-1}; calculation based on 0.46 Na^+ per formula unit) the capacity gets reduced to 98 and 88 mA h g^{-1}, respectively. After 150 cycles, 116 mA h g^{-1} are retained.[93]

2.4 Improving P2-type Na_xMnO_2 - Motivation and Approaches

As outlined in the introduction to Chapter 2, 2.2.3 and 2.3 the interest in electrochemical energy storage has been growing in recent years, and lithium-ion batteries have been at the centre of attention. However, in light of the prospect that an increasing number of applications, such as portable consumer electronics, electric vehicles, or stationary energy storage require electrochemical energy storage devices, concerns about cost and availability of LIB materials have arisen. Besides the intrinsic advantages of NIB described in Chapter 2.3, sodium is significantly more abundant than lithium and Na-based resources have, as a consequence, an advantage in terms of cost. This is one major reason why research on NIBs as an alternative to LIBs has been intensified recently. It was explained that one of the most promising material classes is layered sodium transition metal oxides, as they provide both adequate capacity and stability (Chapter 2.3.1). However, cycling stability of these materials is still not sufficient for commercial applications. Therefore, strategies to mitigate capacity fading are needed, and, particularly, a thorough understanding of the effects of various strategies is required.

The scope of this work was to investigate different approaches to address the low cycling stability of the base material of this structural class, *i.e.* P2-Na_xMnO_{2+z} ($x \approx 0.7$, $z = 0.05 - 0.25$) and to identify levers for improvements. Two successful strategies are presented in this work. One approach is the incorporation of a low amount of cobalt (~10%) into the host structure; the other is an optimisation of the morphology. Both effects were investigated by applying various techniques. The doping strategy has been shown to provide good results for layered materials in LIBs and was therefore recently intensified on the P2 layered manganese oxides for NIB. The first approach investigated here is in line with the recently reported strategies to incorporate other transition metal ions into the host structure. The positive effect of a cobalt dopant addition (~10%) was first investigated electrochemically. It was concluded that sodium ordering processes between the oxide layers are supressed but the average discharge voltage is not significantly affected (Chapter 4.1). Moreover, it was shown that the cobalt enhances Na^+ kinetics in the active material (Chapter 4.4). To investigate structural effects, a new *in operando* X-ray diffraction (XRD)

electrochemical cell was constructed (Chapter 4.3).The obtained data indicated a phase change for the basic undoped manganese oxide material in a low voltage region. A lack of this phase change for the cobalt doped manganese oxide was found in Chapter 4.4 in synchrotron *in operando* XRD experiment. In combination with the suppression of the Na^+-ordering this elimination of structural heterogeneity is identified as the key aspect for higher cycling stability.

The approach to modify the morphology of the active material presented in this work is the first report in literature for the application of this strategy for layered sodium manganese oxides (Chapter 4.2). The change from a flake-like to a spherical morphology was achieved by a newly developed two-step synthesis approach. The capacities achieved over the course of cycling are higher for the optimised morphology. This is attributed to a better retention of morphological features as shown by scanning electron microscopy It is concluded, based on synchrotron *in operando* XRD measurements, that the main cause of this advantage seems to be lower volume expansion during Na^+ insertion compared to the common flake-like morphology and therefore a better accommodation of structural stress for the spheres (Chapter 4.4). A combination of both strategies, Co-doping and morphological optimisation was successfully implemented and proven to combine both effects in a superior material. These insights pave the way for further improvement of cycling performance for this material class.

The results of these investigations are presented in Chapter 4 after a description of the methods employed in this work.

3 Methods

The work described in the main part of this thesis comprises physical and electrochemical characterisation of a variety of materials. Thus, various methods were employed. In the following chapters, the most important methods for the completion of this work are briefly portrayed. First, methods employed for physical characterisation (X-ray diffraction, electron microscopy, inductively coupled plasma optical emission spectrometry, energy-dispersive X-ray spectroscopy, X-ray fluorescence, viscosity, thermogravimetric analysis) are explained, followed by electrochemical methods (galvanostatic cycling, galvanostatic intermittent titration technique, voltammetry, electrochemical impedance spectroscopy).

3.1 X-ray Diffraction[94–102]

3.1.1 Working Principle

The technique of X-ray diffraction (XRD) might be the most applied method in material science to investigate condensed matter. It is the method of choice to investigate the structural properties of materials. This includes the detection of impurities (and their respective ratio) in a compound, or identification of coexisting structural phases of the same stoichiometry, such as distinguishing between rutile and anatase phase of TiO_2. Furthermore XRD can provide information about the atomic size and bond-length in a structure. The principle behind XRD is interference of an electromagnetic wave with matter whose wavelength and size, respectively, have the same order of magnitude. The wavelength of X-rays used for diffraction measurements are in the range of Ångstroms (10^{-10} m) which is roughly the size of the electron shell of an atom / ion or the distance of the atomic planes in a crystal structure. Incident X-rays interfere coherently with the electron shell of atoms along a periodic structural plane. As a consequence of constructive interference occurring from diffracted X-rays from a periodic array (*i.e.* a crystal lattice), diffracted radiation intensifies at certain angles according to Bragg's Law (defined below in Equation 1), resulting in the signal, which is commonly denoted as either a peak, reflex, or reflection.

As a polycrystalline material consists of a variety of several periodic arrays in the plane of the measurement, this gives rise to multiple reflections. The entirety of these reflections is called a *XRD* pattern.The arrangement of the periodic planes in a crystal structure is unique for specific structures, so that the pattern can be used to identify

the structure of a material. The underlying geometric relation (Figure 4) between periodic planes and the interference phenomena is described in Bragg`s law:

$$n \cdot \lambda = 2d \cdot sin\theta$$

Equation 1: (n = integer, λ = X-ray wavelength, d = periodic plane distance, θ = glancing angle [angle between incident beam and reflecting crystallite planes])

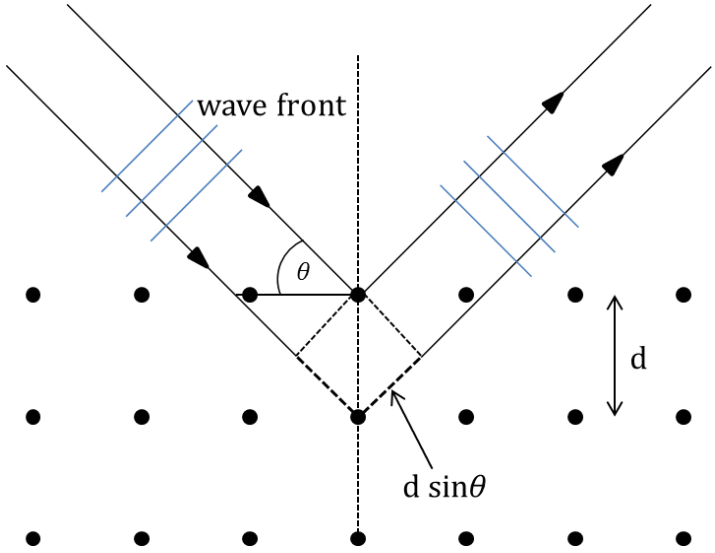

Figure 4. Geometric relation of a crystal structure and incident X-rays.

The diffraction pattern of a solid material can be thought of as a fingerprint for a specific structure, various structural characteristics can be deducted from it:

- The positions of the reflections, *i.e.* the angle θ, gives information on the crystallite lattice size and unit cell;
- The intensity ratios can give information on the exact position and elements in the structure;
- The shape of the reflections can give some information on microstructural properties (crystallite size, strain, *etc.*).

3.1.2 Laboratory X-ray Source

Different kinds of X-ray sources can be used to obtain a diffraction pattern. Depending on the X-ray source, the energy and the wavelength of the X-ray beam is different. In laboratory XRD instruments, a copper anode is often used as an X-ray source. In this set-up, electrons are accelerated from a filament under vacuum towards the positively charged copper target. Due to the interaction of the accelerated electrons with the electron shell of the target atoms, the incident electrons are slowed down and Cu emits energy in the form of X-rays. This so-called 'Bremsstrahlung' is usually a multiple event

leading to a continuous spectrum (white X-rays). The smallest obtained wavelength does thereby depend on the accelerating voltage and the total intensity is given by the filament current.

If the energy of the accelerated electrons is high enough to elevate/eject electrons from the inner electron shell of the target atom, an electron from an outer position will occupy this vacancy, leading to a second superimposed characteristic radiation event (Figure 5).

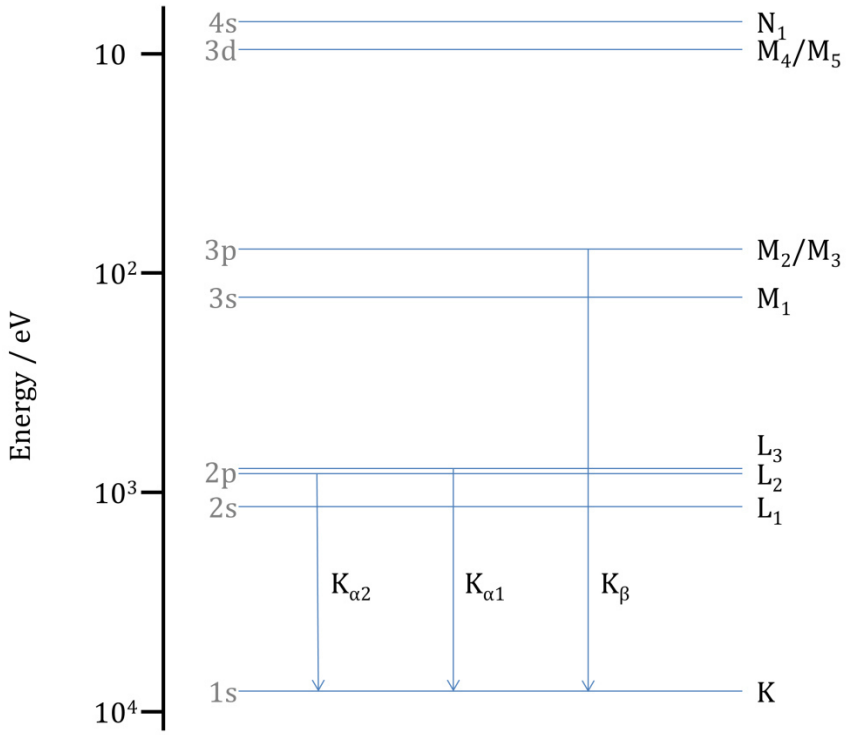

Figure 5. Generation of X-rays in a copper anode.

The energy of the emitted X-rays depends on the energy difference of involved electronic levels within the respective X-ray source. With the help of a single-crystal monochromator (*e.g.* Ge 111) most of the white X-rays and for a Copper target most of the K_β radiation can be filtered out, and mainly the wavelength of $K_{\alpha1}$ can be used for an XRD investigation.

3.1.3 Synchrotron as X-ray Source

In a synchrotron, a charged particle is accelerated to relativistic speeds along a curved trajectory. As a consequence, electromagnetic radiation, the so-called synchrotron radiation is emitted. The complete theory for synchrotron radiation was first described by G. A. Schott in 1912. The principles behind synchrotron radiation are based on Maxwell`s equation for charged particle dynamics in electromagnetic fields, and the theory of the Lorentz force describing particle dynamics in electromagnetic fields – especially the dependence on the direction of the force with respect to the particle direction. A detailed explanation can be found in literature, for example in reference [101]. Synchrotron radiation consists of coherent, polarised photons of high brilliance (common quality measure of X-ray sources) and can have a tuneable wavelength. X-rays generated in a synchrotron are roughly 5-orders of magnitude more intense than X-rays from common laboratory XRD source. Therefore sharp signals with high signal-to-noise ration can be achieved. In addition, as the energy of synchrotron X-rays are more intense the ability to penetrate through matter is much higher than for common lab sources – measurements can be performed in transmission mode. Thus, the behaviour of the bulk of the sample is probed, as opposed to reflection mode, where only a few μm of material are probed. The obtained data is more representative of the processes that occur in the material.

In this work XRD has been extensively employed as structural analysis tool for the identification of newly synthesised materials. Moreover, using *in operando* XRD measurements, it was possible to withdraw conclusions on intercalation mechanism of the investigated materials.

3.2 Electron Microscopy and Spectroscopic Methods[103–107]

Phenomena of interaction of electrons or X-rays with matter led to the development of several applications. One of which is electron microscopy. Electron microscopy is able to resolve features of particles or materials that cannot be resolved anymore by optical microscopy. Figure 6 depicts the set-up of the different microscopy techniques.

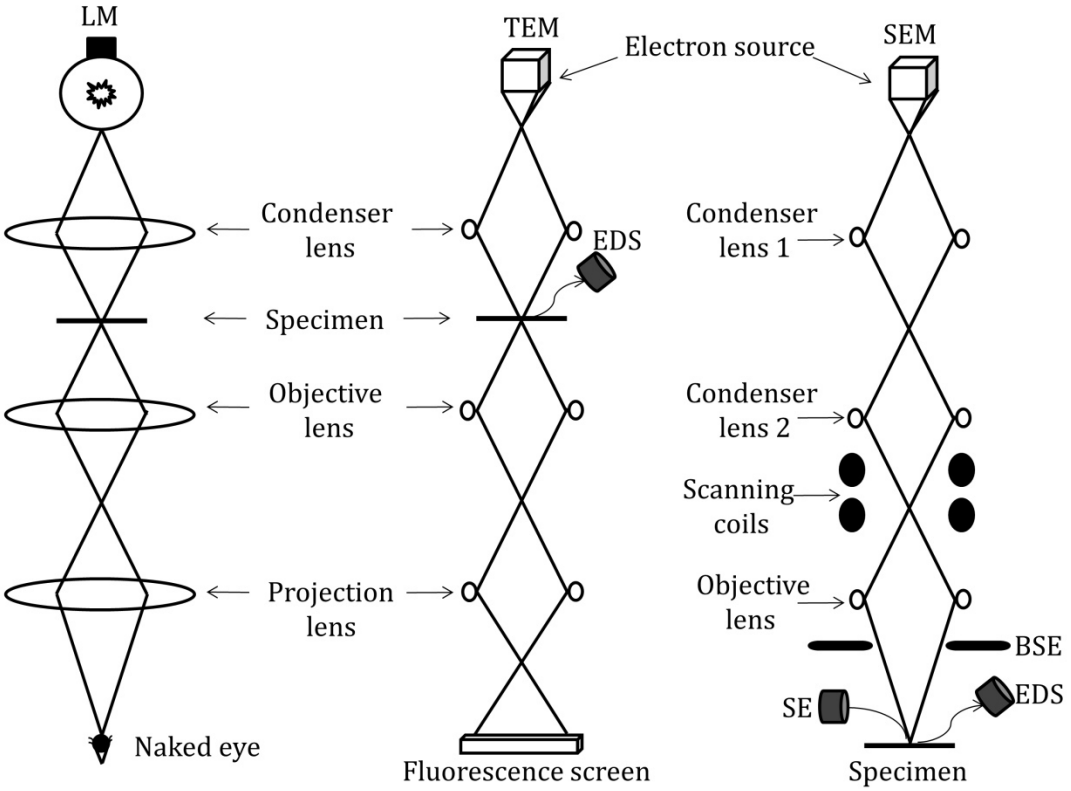

Figure 6. Set-up of an optical light microscope (LM), a transmission electron microscope (TEM), and a scanning emission microscope (SEM). The indicated detectors are secondary electron (SE), energy dispersive spectroscopy (EDS), back scattered electron (BSE) and a fluorescence screen.

Resolution, according to the classical Rayleigh criterion for light microscopy, is roughly half of the used wavelength. As optical microscopy uses the visible spectrum of light (~ 400 – 700 nm), it cannot resolve samples that are smaller than approximately 200 nm. As a consequence, for smaller particles, visible light is replaced with a flux of electrons, as the wavelength of an electron is significantly smaller (due to the de-Broglie relation) than the aforementioned wavelengths in the visible spectrum. The electrons are directed towards the sample with magnetic lenses. This leads to different interactions between electrons and sample, which results in a various signals which can be used to give you information about the sample.

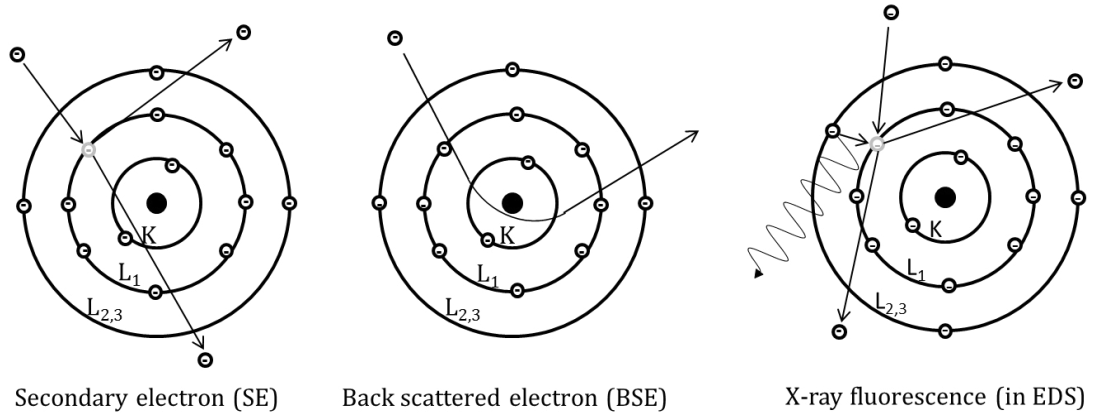

Figure 7. Different ways of electron – matter interaction.

During **elastic interaction**, electrons interact with matter without transferring energy. The incoming electrons interact with the positively charged nuclei of the sample, which leads to a deviation from the initial trajectory. As the interaction is purely coulombic, the deflected electrons still have the same energy which they had initially before the interaction. The most extreme elastic interaction leads to a back scattered electron (BSE, see Figure 7).

The main difference for the case of **inelastic interaction** is the transfer of energy between electron and sample. The electron transfers part of its energy to the sample, which can lead to the emission of radiation due to a variety of processes. These include secondary electrons (SE), Auger electrons, X-rays (EDS/XRF), *etc.* This radiation can be detected used for a variety of microscopy techniques.

The microscopy techniques employed in this work are scanning electron microscopy (SEM) and transmission electron microscopy (TEM). Typically these devices include energy dispersive X-ray spectroscopy (EDS) capabilities which were also employed in this work. As the underlying phenomena for EDS and X-ray fluorescence (XRF) are similar, all these techniques are briefly explained below.

3.2.1 Scanning Electron Microscopy

SEM is mainly based on inelastic interaction of electrons and matter. In this work, SEM measurements were conducted mainly to give morphological and topographical information about the samples. A beam of electrons is rastered over the surface and upon interaction with the sample, the incoming electrons transfer energy to the electron shell of the sample atoms; this leads to an emission of electrons from the sample. These electrons are detected and an SEM image is created. For SEM,

particularly electrons which occupy the valence or conduction band, *i.e.* slow secondary electrons, are used for the generation of the signal.

In addition to the information generated from inelastically scattered electrons, interaction based on elastic interaction can also provide valuable insights into material properties. For elements with "high" atomic numbers, backscattering occurs more frequent. This means that incident electrons are significantly deflected from their path, so that they are scattered backwards and can also be used to generate an image. This is often used to improve the contrast in a sample that consists of different elements. Measuring in backscattering mode is particularly useful when the elements which are present in the sample differ with regard to their atomic number.

SEM imaging was used as a very powerful technique to investigate morphological character of active materials as an as prepared powder or even as a composite electrode. Examining the specimen in various magnification levels, information on the shape, the homogeneity, the granulometry and compactness can be gained.

3.2.2 Transmission Electron Microscopy

In TEM, the so-called direct beam is used for imaging. When the sample is irradiated with electrons, the electrons interact with the nuclei of the sample elements and are subsequently detected by, *e.g.* a fluorescence or semiconductor detector after transmission. To collect the signal by transmission the specimen has to be "electron transparent', *i.e.* thin enough (100 nm) to obtain an interpretable image on the detector. Based on the nature of the sample, the strength of this interaction varies - the higher the atomic number, the stronger the interaction. Concurrently, interaction obviously also varies with sample thickness – when the sample is thicker, more nuclei are in the way of the electrons. Thus, only part of the incident electrons are not deflected – this is the direct beam. As heavier elements and thicker samples result in increased deflection (mass-thickness contrast), fewer electrons reach the detector placed behind the sample, so that the result is a darker image. Consequently, to ensure adequate signal intensity, thin samples are required.

When crystalline samples are measured, incident electrons interfere incoherently and coherently with the electronic shell of the sample. For coherently interference crystallographic information can be collected. The underlying principle is the same as described above for XRD.

The transmission electron microscopy is ideal for a nanoscale analysis of powders. Not only can the morphology can be identified, but also the distribution of crystallite planes within a particle can be visualised, and a diffraction pattern can be obtained. As the particles of the materials used in this study are mostly micron sized and rather polycrystalline.

TEM analysis was predominantly used for morphological analysis (*e.g.* whether spherical particles are hollow), and identification of preferred crystallographic orientation.

3.2.3 Energy Dispersive Spectroscopy (EDS) and X-ray Fluorescence (XRF)[107–110]

As described in Chapter 3.1.2, if an electron hit the sample, the energy can lead to an elevation of a secondary electron (ionisation). This in turn can induce an electron from an outer shell to fall back to the energetically favoured inner shell position, leading to an emission of characteristic X-ray radiation (Figure 8).

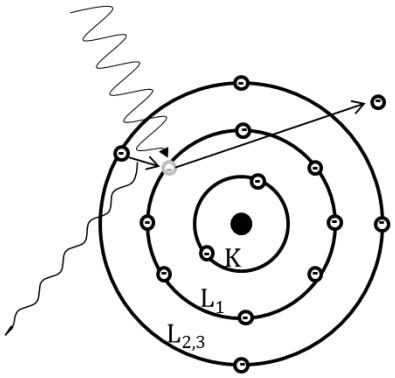

Figure 8. X-ray – matter interaction resulting in fluorescence.

As this X-ray radiation is like a fingerprint for an element species, an element analysis can be conducted on the materials surface. The ionisation energy to excite the inner electron can be reached via electrons with a high kinetic energy (principle of EDS) or via X-rays or gamma rays with a wavelength of $\sim 10^{-12}$ m (principle of XRF).

Both EDS and XRF have been applied in this thesis to identify the composition of materials and elemental ratios.

3.2.4 Inductively Coupled Plasma Optical Emission Spectroscopy (ICP-OES)[111,112]

Inductively coupled plasma (ICP) gained attention as an activation source in the field of atomic emission spectroscopy (AES) in the 1970`s. AES identifies and quantifies elements in a sample by radiative de-excitation of electrons of the respective elements, leading to characteristic spectra. Due to its properties as an ionised gas, plasma has been found to be the most suitable to excite electrons. A plasma is a domain of high energy (~5000 – 7000 K) in which ions and electrons coexist in equilibrium next to each other and is often considered as fourth state of matter, besides solid, liquid and gas. In an ICP the plasma is stimulated by argon atoms with a high kinetic energy and is sustained by an induction coil emitting a high-frequency electrical field. Argon gas is predominately used due to its high ionisation energy, its noble character (*i.e.* it does not to form any bonds with specimen elements) and its simple emission spectrum. The residence time of the sample in the ionising plasma is only in the range of milliseconds. Therefore only small liquid droplets (aerosols) or small solid particles can be introduced to ensure vaporisation and ionisation. Therefore either solutions or small particle dispersions are introduced via a nebuliser system before entering the plasma with the gas flow. After excitation and de-excitation of the specimen the intensity of characteristic spectral lines is detected by a dispersive system. As the intensity is not an absolute value, standard samples for each element of interest must be measured to gain a calibration. The detection limit in solution is in the range of 0.01 to 50 μg L^{-1}, depending on the sample conditions and the specific element.

In this thesis ICP-OES was used to determine the specific elements and their ratio in the synthesised active materials.

3.3 Viscosity Measurements[113]

Viscosity describes the resistance of fluids towards a shear strain or stress. The resistance can be seen as internal friction caused by interactions and attractions forces on atomic/molecular level. As this resistance applies also for the moving object within the fluid, *e.g.* charge carrier transported in an electrolyte, the viscosity is an important characteristic for the presented ionic liquid under Chapter 4.5. The viscosity has been measured by an Anton Paar Rheometer, where a specific shear rate was applied by a rotating circular cone of 25 mm diameter, with the cone surface completely immersed into the ionic liquid. As ionic liquids are discussed for their potential applications at elevated temperature and battery performance are tested under different temperature conditions the high depends of viscosity on temperature was investigated.

3.4 Thermogravimetric Analysis[114,115]

Thermogravimetric Analysis (TGA) measures the relative weight change of the sample in relation to a temperature gradient under a controlled atmosphere. Therefore, TGA can provide information on *e.g.* evaporation, temperature depended oxidation or reduction and decomposition processes of the sample or parts of it. In combination with a mass spectrometer (TGA-MS) the volatile sample parts or fragments get ionised get ionised and separated based on their charge to mass ratio $\left(\frac{q}{m}\right)$ under the influence of electrostatic and magnetic field separators. The decomposition mechanism can be inferred from the masses of the detected fragments.

Under Chapter 4.5 TGA-MS was used to define the decomposition point of the investigated ionic liquid and to monitor the sequence of decomposition.

3.5 Electrochemical Measurements

3.5.1 Electrochemical Cell[116]

An electrochemical cell (or battery) has already been shown in Chapter 2.2.3, Figure 1. In order to study the characteristics of an electroactive material or of the electrolyte, different cell schematics can be used. As the observable 'electrochemical potential' is based on a differential measurement, the investigated redox process induced on the working electrode (WE) is relative to a reference electrode (RE) which has a known and stable potential. As a current flow via the reference electrode changes its potential, the respective current is balanced by a third electrode, the counter electrode (CE). The electrical circuit of such a set-up is shown in Figure 9. Three electrode setups have been applied for stability measurements for electrolytes (Chapter 4.5) and for impedance measurements in Chapter 4.4.

For water based systems many stable reference electrodes of the first and second kind are known. The former only depend on the redox interfacial potential like a metal in its solution or the standard hydrogen electrode. The latter depend on two equilibria: the redox equilibrium and the solubility equilibrium of the cation in solution and its sparely soluble salt. Common secondary electrodes are the saturated calomel electrode or the silver/silver chloride electrode. As the intercalation processes described in this work occur in organic electrolytes, the aforementioned reference systems cannot be used. Thus, a pseudo-reference electrode was typically employed. For NIBs, this was the redox couple $Na|Na^+$ immersed in the respective electrolyte. In this thesis, a two-

electrode coin cell set-up was used for most of the electrochemical tests, where the counter and reference electrode are identical, and the potential is measured directly between RE and WE. In this case, the current flow via the reference electrode leads to a deviation from the reference potential due to overpotential. By the use of the respective alkali metal the overpotential is rather small and negligible. Figure 9 shows schematically the components of a three and a two electrode circuit.

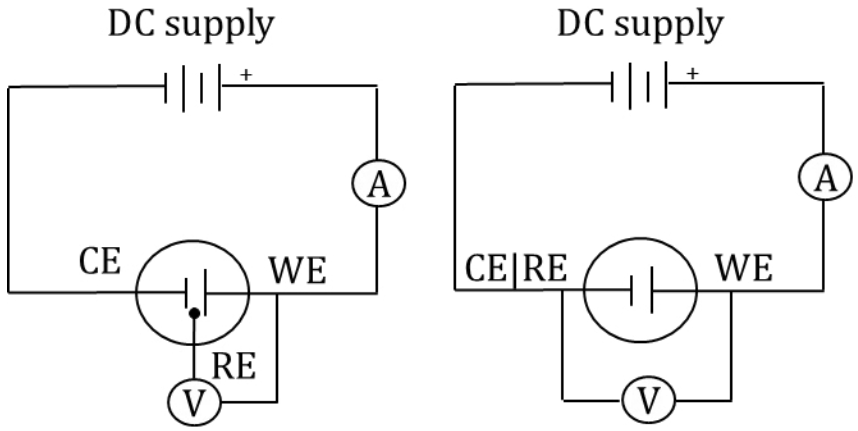

Figure 9. Schematic circuit of a three (left) and a two (right) electrode cell. (A): current-, (V): potential measurement.

3.5.2 Electrode Preparation and Coin-Cell Assembly

In order to obtain a comparable data basis and ensure that preparation-related limitations, such as conductivity or adhesion, did not impede the measurements, a high ratio of activated carbon and binder was chosen to ensure a proper contact and similar performance for different materials. Polyvinylidene difluoride (PVDF), which acts as binder, was dissolved in N-methylpyrrolidone (NMP). The active materials where mixed with activated carbon (20 wt%) to improve conductivity. PVDF solution was added (20 wt%) and mixed with the active material / carbon mixture. Additional NMP was added to reduce viscosity and form a homogeneous slurry. After rigorous mixing, this slurry was places on an Al foil and evenly distributed with the help of a doctor blade. Subsequently, the NMP was evaporated. Circular electrodes were punched (16 mm) from this coating, pressed to gain a higher packing density and dried overnight in a Buchi oven under vacuum at 110 °C before being transferred into the glovebox.

For the electrochemical tests the electrodes were installed in a two electrode coin-cell construction as shown in Figure 10. The used coin-cell housing was of the 2016-type (diameter: 20 mm, height: 1.6mm).

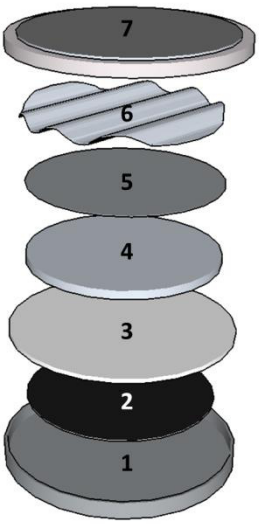

Figure 10. Illustration of a coin-cell setup: 1) bottom part, 2) cathode electrode, 3) separator, 4) Na-metal anode, 5) spacer, 6) spring, 7) top part (schematic adapted from [117]).

For consistency the following set up was used for each cell (Figure 10). At first the previously prepared electrode is placed in the bottom part of the housing (#2 into #1). Then, 75 µL of electrolyte was dropped onto the active material of the electrode. As electrolyte a 1M $NaClO_4$ solution in ethylene carbonate/propylene carbonate (wt% = 50:50) was used. Number 3 is the separator circular punched from a Whatman glass fibre filter paper (19 mm in diameter), which was soaked with further 75 µL of electrolyte. A circular metallic sodium piece (#4, 16 mm in diameter) was placed on top, supported by a 100 µm stainless steel spacer disk (#5). Afterwards the cell was closed and crimped with the top part (#7), which was spot-welded to a rippled stainless steel spring (#6) to ensure uniform pressure on the electrodes.

3.5.3 Galvanostatic Cycling[116,118]

In galvanostatic measurements, a constant current is applied to the system until a pre-defined limit of another variable, typically time or voltage, is reached. This type of measurement is often used to determine the voltage limits and capacity of new battery materials. Suitable voltage ranges can be determined by varying the lower and upper voltage limits and observing the amount of current that is flowing, as well as reversibility of these currents. Capacity is proportional to the absolute current during a measurement, and thus to the number of transferred electrons.

This correlation is expressed by Faraday's law:

$$Q = \frac{m * z * F}{M}$$

Equation 2. Faraday's law. Q is the total charged transferred in the observed process, m is the mass of electrode material, z is the number of electrons, F is Faraday's constant: 96485 A s mol^{-1}, and M is the molar mass of the electrode material.

Typically, as electrode masses often differ, capacities are normalised to the mass of the electrode material and expressed in mA h g^{-1}.

A good indication of the reversibility of the electron transfer is the Coulomb efficiency, which is defined as the ratio of the current transmitted during discharge and the current transmitted during charge:

$$\eta = \frac{Q_{discharge}}{Q_{charge}} * 100\%$$

Equation 3. Coulombic, or Coulomb efficiency $\boldsymbol{\eta}$, $Q_{discharge}$ is the discharge capacity (or current), and Q_{charge} is the charge capacity (or current).

Thus, this variable indicates what percentage of the current that is being 'fed' into the system during charge can be recuperated during discharge. As this property is indicative of how reversible cycling, *i.e.* periodic charge / discharge processes, is, it is closely related with another crucial quantity: cycling stability. Cycling stability describes how much of the initial capacity is retained during cycling, and is calculated as follows:

$$cycle\ stability = \sqrt[n]{\frac{Q_n}{Q_0}}$$

Equation 4. Cycling stability described by: n is the number of cycles considered, Q_n is the discharge capacity after n cycles, and Q_0 is initial discharge capacity.

Following this equation, a cycling stability of 1, *i.e.* 100%, describes a constant discharge capacity over the course of n cycles without any decrease of capacity. Obviously, for commercial applications cycling stabilities close to 100% are targeted. For some materials, cycling stability can be larger than 100% for the first cycles. As this means that the amount of charge that is retrieved from a system exceeds the amount of charge that was initially fed into the system, irreversible processes during the discharge process occur. This can be attributed to several factors, such as parasitic side reactions (*e.g.* undesired decomposition of the electrolyte). Especially for anode materials, a solid-electrolyte interphase layer is formed in the first few cycles. Even though this process is based on partial decomposition of the electrolyte, it is necessary

for the stability of a variety of anode materials and is therefore a desired process. The result of this is a coulombic efficiency that can significantly exceed 100% in the first cycles.

In galvanostatic measurements, the applied current is the independent variable, *i.e.* the current is controlled throughout the measurement. There are different systematics to describe this current. Particularly for new materials which are not yet well known, absolute mass-normalised values are chosen for the current, as no previous knowledge about the respective materials is required and they ensure good comparability. For example, materials can be (dis-)charged at a current rate of 50 mA g^{-1}. Another popular systematic is based on the absolute capacity a material can provide, and classifies the rate at which a material is (dis-)charged based on the so-called C-rate. When a material is discharged at a C-rate of 1 (*i.e.* at 1C), the duration of one complete discharge is one hour. In other words, the applied current is set to a value at which it takes theoretically one hour to extract 100% of the capacity ('C'). Accordingly, when a material is cycled at 2C, theoretically 100% of the total capacity can be extracted within 0.5 hours, and at a C-rate of 0.5, it takes theoretically two hours to completely discharge the system. The same logic is applied for the charge process. As this classification is based on the theoretical or initial capacity of the material, it is particularly helpful for optimised materials with a very high cycling stability. When capacities decrease continuously, C-rates, strictly speaking, change during the course of cycling. Thus, as the materials presented in this work are new materials with a certain degree of capacity fading, the current rate methodology is used.

3.5.4 Galvanostatic Intermittent Titration Technique[119–123]

Galvanostatic intermittent titration technique (GITT) is one of the most applied chronoamperometry techniques.[124] The theory behind this measurement in its basic form was developed by Weppner and Huggins for electrochemical alloy formation.[120] Under certain assumptions it has been shown that the GITT technique can also be used also for insertion materials. These assumptions include diffusion according Fick`s law and a uniform current distribution throughout the material. Furthermore, an estimation of the electroactive area has to be done. Thus, the transfer of this technique to insertions processes is particularly problematic if a first order phase chance is taking place during insertion of Li^+ or Na^+, respectively. However, by a proper adaption of the conditions, GITT can still be employed to identify certain trends.[122]

The procedure is the alternation of two processes. At first a constant current flux is applied for a limited time to induce diffusion towards the active material and (de)intercalation processes. Secondly, it is followed by a relaxation period at open circuit conditions, to give the system time reach its thermodynamic equilibrium state.

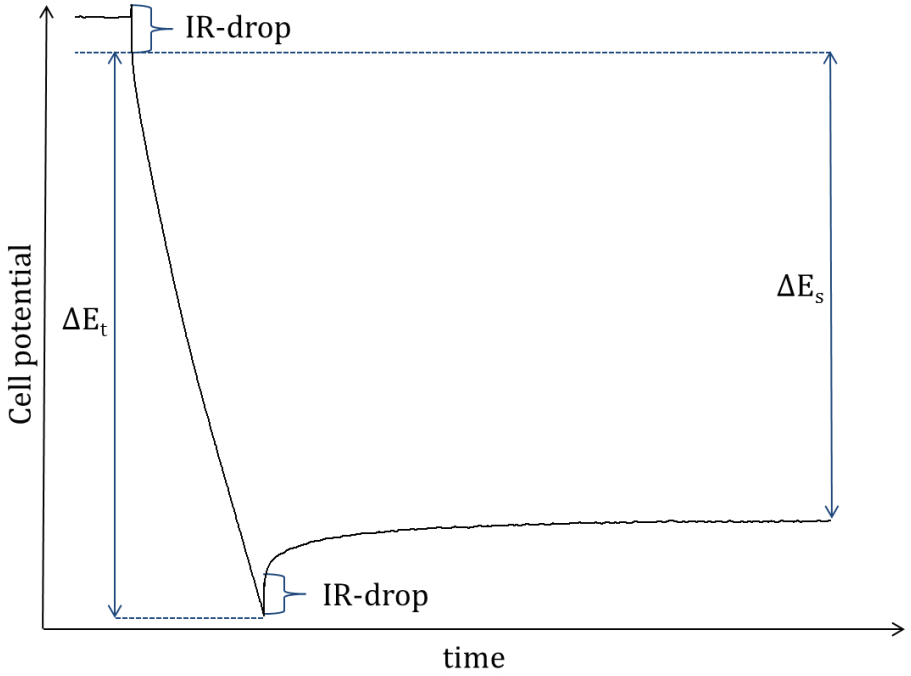

Figure 11. Applied current pulse and subsequent relaxation period in an actual GITT experiment performed under Chapter 4.4. $\Delta \boldsymbol{E_t}$ is the total transient voltage change for the current pulse and $\Delta \boldsymbol{E_s}$ is the steady state voltage change of the step.

$$D = \frac{4}{\pi}\left(\frac{i\,V_m}{z_A\,F\,S}\right)^2\left[\frac{(\Delta E_s)}{(\Delta E_t)}\right]^2$$

Equation 5. D is the diffusion coefficient, V_m is the molar volume of the unit cell, i is the applied current, z_A is the charge number, F is Faraday's constant, S is the electrode / electrolyte contact area which is mostly assumed to be the geometric surface of the electrode, $\Delta \mathbf{E_t}$ is the total transient voltage change for the current pulse and $\Delta \mathbf{E_s}$ is the steady state voltage change for this step.

By alternating between the (dis)charge current and the relaxation period, the equilibrium potential as a function of Li/Na content can be achieved. Moreover, the estimation of the diffusion coefficient $D_{Li/Na}$ can be calculated applying Equation 5, where ΔE_s in this equation can be expressed by the slope of the coulometric titration curve$\left(\frac{dE}{d\delta}\right)$, and ΔE_t is the slope of the linearised plot of the potential E (V) during the current pulse $\left(\frac{dE}{d\sqrt{t}}\right)$. The calculation for the diffusion coefficients is based on the volume of the initial unit cell.

In this thesis GITT measurements have been used for the comparisons of the kinetic behaviour of materials presented in Chapter 4.4.

3.5.5 Linear Sweep- and Cyclic Voltammetry (LSV & CV)[116,118,123,125]

LSV and CV are related techniques and are employed to investigate the nature of redox processes in an electroactive material. In addition, information on the underlying electron transfer in terms of its kinetic or diffusion characteristics can be obtained. In a LSV experiment a linear sweep rate of potential vs time $\left(\frac{dE}{dt}\right)$ is applied for a fixed potential range (between V_1 and V_2) and the current is recorded. An increase in potential (anodic scan) is accompanied by oxidation reactions. For the case of (de-)intercalation processes in a cathode material, this corresponds with the de-insertion of the charge carrier from the structure. A decrease in potential (cathodic reaction scan) is accompanied by the respective reduction process. This corresponds with the intercalation of the charge carrier into the electrode material. In a typical CV experiment both scan directions are applied subsequently. Figure 12 shows a typical triangular shape of the potential plot *vs*. time of a CV experiment and the current response of an induced reversible single electron transfer for oxidation and reduction.

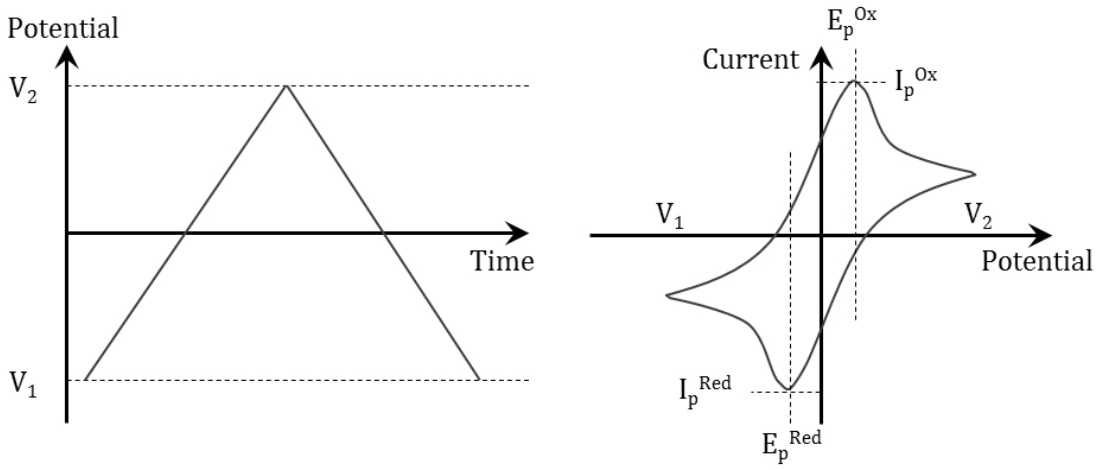

Figure 12. Left side shows the applied voltage scan; right side the respective voltammogram.

By plotting the relation between the scanned potential range *vs*. the current response in a voltammogram, preferably for different scan rates, various data can be withdrawn. The evaluation of the CV data can lead to information regarding the reversibility of a process, the coulomb efficiency, the aforementioned kinetic characteristics of the electron transfer, diffusion coefficient of the underlying process as well as indications to the nature of the active material. While in basic electrochemistry the underlying redox process is the reaction of an electroactive species in solution on ideal electrodes some assumptions have to be made to apply similar principals for intercalation electrode materials. Ideally, a large flat electrode with only Faradaic processes and

negligible capacitive currents with a linear diffusion of the redox species towards/from the electrode is desirable. Realistically, besides the charge transfer reaction, other scan rate dependent effects on the voltammetric signal have to be considered to properly investigate battery materials. These include transfer processes from/to the surface of the electrode, as well as the transport inside the material, adsorption and other surface processes, structural rearrangements inside the material and chemical reactions interposed between two charge transfer reactions.

In addition certain terms are used differently for the investigation of battery materials as compared to classic electrochemistry. In an ideal reversible redox process the difference of the peak maxima from Ox (E_p^{Ox}) and Red (E_p^{Red}) are independent of the scan rate with a value of 59 mV. In addition, the ratio of the peak currents (I_p^{Ox} / I_p^{Red}) is one. Reversibility for the case of electrode materials means a reversible intercalation process, *i.e.* integration of the current of the positive and negative scan are equal.

CV experiments have been employed for all here investigated materials. LSV was only employed to determine the voltage stability range of the newly introduced ionic liquid described in Chapter 4.5.

3.5.6 Electrochemical Impedance Spectroscopy (EIS)[118,126]

Electrochemical impedance is a powerful method to probe the dynamic characteristics of an electron transfer in an active material. The current response (I) of an electrochemical system towards an alternating potential (U) is typically a nonlinear relation. EIS is a tool to describe this. To keep the system as close as possible in a linear relation the applied amplitude of the sinusoidal potential is usually small (~5-20 mV). A schematic model for the interfacial electron transfer reaction is given by an electrical circuit (Figure 13).

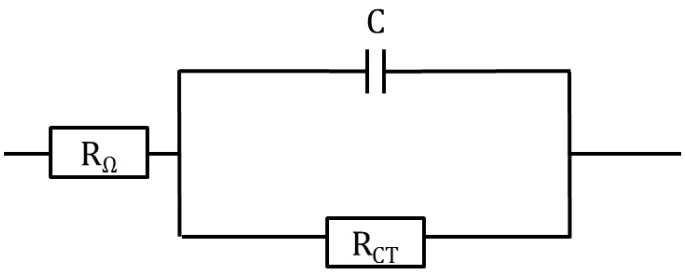

Figure 13. Electrical circuit scheme equivalent for interfacial electrochemical reactions, where R_Ω corresponds to the Ohmic resistance, C correspond to the double layer capacitance and R_{CT} corresponds to the charge transfer resistance.

The electron transfer at the electrolyte | electrode interface is expressed by a polarisation or charge transfer resistance R_{CT}. R_{CT} is combined in series with the Ohmic resistance (R_{Ω}), *i.e.* the sum of all cell component resistances (*e.g.* electrolyte, *etc.*), and in parallel with a capacitive element (C) for the double layer capacitance. The complex frequency dependence of the impedance $Z(i\omega)$ can be described in following equations:

$$Z(i\omega) = \frac{E}{I} = Z_0(cos\phi + i\, sin\phi) = R_{\Omega} + \frac{R_{CT}}{1 + i\, 2\pi\, \omega\, R_{CT}\, C}$$

Equation 6. Relation of impedance *Z* with the applied potential *E* and corresponding current *I*, or expressed by a complex function combining the real and imaginary portion. The third complex function relates *Z* with the frequency dependent R_{CT} and *C*, ω stands for the frequency, *i* correspond to an imaginary number ($\boldsymbol{i} = \sqrt{-\mathbf{1}}$).

Although the theory is technically only applicable for negligible capacitance dispersion, meaning a flat, non-porous electrode surface, certain trends can be still obtained for porous intercalation materials. Is the frequency (ω) high the equation can be simplified to $Z = R_{\Omega}$, whereas if the frequency is low, simplification gives $Z \approx R_{\Omega} + R_{CT}$. In this work most of the impedance was presented in the so-called Nyquist plot based on Cartesian coordinates, with the imaginary part ($-\mathrm{Im}(Z) = \mathrm{i}\sin\phi$) on the y-axis and the real part ($\mathrm{Re}(Z) = \cos\phi$) on the x-axis. The first x-intercept in such a plot corresponds to R_{Ω} and the second x-intercept to $R_{\Omega} + R_{CT}$. By subtraction of R_{Ω} from $R_{\Omega} + R_{CT}$ the charge transfer resistance of a system can be determined.

In Chapter 4.4 EIS was applied to compare the kinetics of the Co-doped and undoped flake material and in 4.5 to gain information on the solid electrolyte interphace development for the ionic liquid electrolyte, respectively.

4 Results

As described in Chapter 2.3.1 and 2.4, layered sodium manganese oxide are a material class which are suitable candidates for future NIB cathodes, owing to the low cost and high abundance of manganese. However, cycling stability still remains a problem in NIBs. In the following chapters my peer-reviewed publications that originated from my research on this topic are presented. The main focus was on selecting strategies for synthesis and structure variations. For positive findings, the fundamental causes of the improvements were investigated. In Chapter 4.1, the positive effect of 11% cobalt doping of P2-type Na_xMnO_2 and the difference of the electrochemical behaviour is described. Chapter 4.2 presents the first investigation of morphology optimisation for the material class of P2 Na_xMnO_2. To investigate structural reasons for the positive influence of both strategies an *in operando* XRD cell for laboratory diffractometers was developed. This work is presented in Chapter 4.3. A fundamental study of both strategies, based on various analytical techniques, is presented in Chapter 4.4. The work described in this chapter also includes the description of a successful combinatorial approach, *i.e.* synthesis of a Co-doped spherical material. Besides these two main strategies on structural alterations a third approach to improve cycling stability was investigated. As the interaction between the electrode material and the electrolyte can have an influence on stability, solubility of active material in the used electrolyte was tested (Chapter 4.4). Finally, in Chapter 4.5, a new ionic liquid structure is presented. Successful tests as potential electrolyte in LIBs, as well as first results for Na_xMnO_{2+z} and $Na_xCo_{0.1}Mn_{0.9}O_{2+z}$ spheres are described.

4.1 Combustion-Synthesised Sodium Manganese (Cobalt) Oxides as Cathodes for Sodium-Ion Batteries

This chapter is a summary of the publication "Combustion-synthesized sodium manganese (cobalt) oxides as cathodes for sodium ion batteries" (Journal of Solid State Electrochemistry **2013**, *17*, 1923-1929). It is the first work on NIBs in our group, and was conceived when interest in this material class was increasing tremendously as described in Chapter 2.3. N. Bucher was leading the work that is presented in this publication.

In this publication, we demonstrated that P2-type Na_xMnO_2 (NMO) synthesised via a combustion method, which was previously only used as precursor for LIB materials,[40,42] is a suitable candidate for NIB cathodes. Moreover, the positive influence of Co-doping (11%) on cycling stability was demonstrated.

Both NMO and $Na_{0.7}Co_{0.11}Mn_{0.89}O_2$ (NCO) crystallise in the same structure (space group $P6_3/mmc$), which consist of layers of MnO_6 octahedra separated by Na-ions, and show the same hexagonal flake-like morphology. While the cyclic voltammogram for both materials shows a major transition at approximately 2.0 / 2.5 V *vs*. $Na|Na^+$, the CV of NCO is rather flat throughout the remaining potential range of 1.5 – 3.8 V *vs.* Na, whereas the CV of NMO shows a variety of peaks, indicating different electrochemical processes. Due to reported similar findings for the isostructural P2-$Na_{0.7}CoO_2$, These processes are attributed to Na^+-ordering within the layers. [86,127–129]

The peak in the CV are also reflected in the galvanostatic charge/discharge curve – even though both materials show the same capacity, the galvanostatic courves differ: various minor plateaus in the discharge curve of the NMO shows the same Na^+-ordering processes which were indicated in the CV. During cycling, capacities decrease for both NMO and NCO. However, the decay is more significant for NMO than for the doped analogue.

Coulombic efficiency is similar for both materials. Thus, it is reasoned that suppression of parasitic side reactions is not the cause of the enhanced cycling stability of the Co-doped flakes over the undoped NMO flakes. Therefore, structural reasons were discussed, such as suppression of Na^+-ordering between the layers of MnO_6-octahedra, which could lead to enhanced Na^+-transport within the cathode. In general, the need

for further studies to elucidate the reason(s) for the difference in cycling stability was determined in order to deduce design principles for future NIB cathodes.

In summary, Co-substituted (11%) P2-type Na_xMnO_2 was obtained via a combustion synthesis method and was shown to improve cyclability. The suggested reason for the increased stability was a suppression of the Na^+ ordering processes during cycling.

Combustion-synthesized sodium manganese (cobalt) oxides as cathodes for sodium ion batteries

Nicolas Bucher, Steffen Hartung, Irina Gocheva, Yan L. Cheah, Madhavi Srinivasan and Harry E. Hoster

Springer and Solid State Electrochem. **2013**, *17*, 1923–1929/Combustion-synthesized sodium manganese (cobalt) oxides as cathodes for sodium ion batteries, Nicolas Bucher, Steffen Hartung, Irina Gocheva, Yan L. Cheah, Madhavi Srinivasan and Harry E. Hoster, 6 Figures, © Springer-Verlag Berlin Heidelberg 2013; with kind permission from Springer Science and Business Media.

The publication can be found under the following weblink:

http://dx.doi.org/10.1007/s10008-013-2047-x

J Solid State Electrochem (2013) 17:1923–1929
DOI 10.1007/s10008-013-2047-x

ORIGINAL PAPER

Combustion-synthesized sodium manganese (cobalt) oxides as cathodes for sodium ion batteries

Nicolas Bucher · Steffen Hartung · Irina Gocheva · Yan L. Cheah · Madhavi Srinivasan · Harry E. Hoster

Received: 7 January 2013 / Revised: 15 February 2013 / Accepted: 18 February 2013 / Published online: 13 March 2013

Abstract We report on the electrochemical properties of layered manganese oxides, with and without cobalt substituents, as cathodes in sodium ion batteries. We fabricated sub-micrometre-sized particles of $Na_{0.7}MnO_{2+z}$ and $Na_{0.7}Co_{0.11}Mn_{0.89}O_{2+z}$ via combustion synthesis. X-ray diffraction revealed the same layered hexagonal P2-type bronze structure with high crystallinity for both materials. Potentiostatic and galvanostatic charge/discharge cycles in the range 1.5–3.8 V vs. Na | Na^+ were performed to identify potential-dependent phase transitions, capacity, and capacity retention. After charging to 3.8 V, both materials had an initial discharge capacity of 138 mA h g^{-1} at a rate of 0.3 C. For the 20th cycle, those values reduced to 75 and 92 mA h g^{-1} for Co-free and Co-doped samples, respectively. Our findings indicate that earlier works probably underestimated the potential of (doped) P2-type $Na_{0.7}MnO_{2+z}$ as cathode material for sodium ion batteries in terms of capacity and cycle stability. Apart from doping, a simple optimization parameter seems to be the particle size of the active material.

Nicolas Bucher and Steffen Hartung contributed equally to this manuscript.

Dedicated to Prof. Wolf Vielstich on the occasion of his 90th birthday and in recognition of his contributions to electrochemistry.

N. Bucher · S. Hartung · I. Gocheva · M. Srinivasan (✉) · H. E. Hoster (✉)
TUM CREATE, Singapore 138602, Singapore
e-mail: madhavi@ntu.edu.sg
e-mail: harry.hoster@gmx.de

N. Bucher · S. Hartung · H. E. Hoster
Technische Universität München, 85748 Garching, Germany

Y. L. Cheah · M. Srinivasan
School of Materials Science and Engineering, Nanyang Technological University, Singapore 639798, Singapore

Introduction

Growing interest in the integration of sustainable energy sources into the electricity grid has spurred immense interest in the field of energy storage applications in the recent years. The pre-dominant commercial battery system is the lithium ion battery (LIB), which has become the standard energy source for portable electronic devices and currently gains increasing importance for the electric propulsion of vehicles [1–6]. There are several approaches to remedy the inherent problems of LIBs, like battery cost and safety. One approach that has attracted wide attention is aqueous lithium ion battery systems. Only recently, several water-based batteries with high capacities of approximately 120 mA h g^{-1} and excellent cycle efficiencies using $LiMn_2O_4$ as cathode material have been developed [7–9]. Another promising alternative to conventional LIBs is the sodium ion battery (NIB) [10–13], owing to worldwide abundance of Na metal and lower cost of Na_2CO_3 (€~0.40 kg^{-1}) than that of Li_2CO_3 (€~4 kg^{-1}) [14]. Even more important are potential cost savings for the cathode material. Such cost arguments are even more relevant for larger scale rechargeable batteries as they are currently discussed for the stabilization of electric grids. Though both Li and Na are alkali metals, the best electrode materials for LIBs are not necessarily the best for NIBs. In particular, NIBs offer the potential to avoid the expensive cobalt oxide-based cathodes that are common in LIBs [15]. Two main challenges related to NIBs are (1) the generally lower voltage and (2) the larger volume change due to (de-)intercalation of Na^+ as compared to Li^+ ions. The latter implies additional strain on the crystal structure during cycling, with negative impact on the cycle life. As Na-based chemistry is less well explored than Li-based

chemistry in the field of energy storage, there is a good chance that known structures that do not work in LIBs are found to work in NIBs.

Layered manganese oxides in their manifold structures [16, 17] are used and discussed as cathode materials in lithium ion [18, 19] and sodium ion [20, 21] batteries since long. For Li ion batteries, $LiMnO_2$ with its high theoretical capacity of 285 mA $h g^{-1}$ is an attractive alternative to the common $LiCoO_2$, also due to the much lower price of Mn as compared to Co. An inherent problem of Li_xMnO_2, however, is its instability against a transformation from a layered into a spinel structure in charged state, i.e. at low Li content x [22], which goes along with capacity fading. Ma et al. recently highlighted that for Na_xMnO_2 such a degradation to a spinel structure is thermodynamically and kinetically disfavoured as compared to Li_xMnO_2 [23], i.e. NIBs could be fabricated based on this rather cheap and non-toxic class of cathode materials. Nevertheless, cycling stability remains a central challenge for Na ion batteries [14, 21], and a broad community is tackling this challenge in several ways [24–27]. For layered manganese oxides as cathodes in LIBs, significant improvements of the cycle life were achieved by partial substitution of Mn by other transition metals ("doping") [19]. Interestingly, those cathode materials were prepared via the sodium-containing precursors $Na_{0.7}M_{0.11}Mn_{0.89}O_{2+z}$ (M=Fe, Co, Ni, Cu, Zn, Al; z=0.05 accounts for cation vacancies in the MO_2 layers [16]), but their electrochemical properties were only tested after an ion exchange from Na to Li.

In this paper, we will show that the powders generated by the combustion synthesis method [28] used by Doeff et al. in the cited work [19] are not only useful precursors for the fabrication of LIB cathodes but are also well-performing cathodes for NIBs. As test cases, we will show first results for $Na_{0.7}MnO_{2.05}$ and $Na_{0.7}Mn_{0.89}Co_{0.11}O_{2.05}$, both with the same P2-type layered structure [17]. After a description of synthesis and analysis methods and procedures, we will first present the crystal structure and morphology of the samples as analyzed by X-ray diffraction (XRD) and field emission scanning electron microscopy (FESEM), respectively. We will then evaluate potentiostatic and galvanostatic charge–discharge curves of both materials with respect to their initial Na content, their potential dependent phases, their coulomb efficiency, and their cycling stability. The results will be discussed in comparison to previous findings for P2-$Na_{0.7}MnO_2$ [20], P2-$Na_{0.6}MnO_2$[21], monoclinic $NaMnO_2$ [23], P2-Na_xCoO_2 [29], and P2-$Na_{2/3}Co_{2/3}Mn_{1/3}O_2$ [30].

Experimental

Synthesis

$Na_{0.7}MnO_{2+z}$ was synthesized using the combustion method as described by Doeff et. al. [19, 31, 32]. Sodium nitrate (Sigma Aldrich, ≥99 %) and manganese acetate (Alfa Aesar, anhydrous, 98 %) were mixed in Na/Mn mole ratio of 7:10 before being dissolved in deionized water, followed by the addition of concentrated nitric acid (≥69 %, Honeywell) in excess and 1.5 g of gelatin. The solution was heated to 250 °C until spontaneous combustion occurred. Oxidation of the amino groups of the gelatin not only releases the required heat but also yields substantial amounts of gaseous products (N_2, CO_2, H_2O) that facilitate the reaction and ensure small particle sizes. The product is a dark brownish powder with cotton-wool-like texture. For better crystallization, the powder was annealed in air at 800 °C for 4 h. For the cobalt-doped cathode, cobalt nitrate (Sigma Aldrich, ≥98 %) was added to the precursors in the mole ratio of Na/Co/Mn 7:1.1:8.9. The subsequent synthesis steps were carried out as described above, obtaining $Na_{0.7}Co_{0.11}Mn_{0.89}O_{2+z}$ (according to elemental analysis). In this paper, we will refer to the Co-free and Co-doped samples as NMO and NCO, respectively.

Characterization

The crystal structures of the synthesis products were analyzed by powder XRD using a Bruker X-ray diffractometer with Cu–K_α radiation. Then, 2θ was varied within a range of $10° < 2\theta < 80°$, using a step size of 0.017° and 1.7 s per step. The obtained XRD patterns were analyzed by Rietveld phase analysis using a Lebail approach within the Topas version 3 software, employing the fundamental parameter approach [33–35]. The powder morphology was analyzed by FESEM (JEOL JSM-7600F), including elemental analysis. Brunauer–Emmet–Teller (BET) surface area measurements were carried out with a Nova 3200e surface area and porosity analyzer.

Electrochemical measurements

The composite cathodes were prepared by mixing active material (NMO or NCO), acetylene black (Alfa Aesar, >99 %), and polyvinylidene fluoride (PVdF, Arkema, Kynar HSV 900) binder in the weight ratio of 60:25:15, with N-Methyl-2-pyrrolidone (NMP, Sigma Aldrich, ≥99 %), to form a slurry. The well-mixed, homogenous mixture was coated on an Al foil (16 μm in thickness) using a doctor blade and dried at 80 °C in air to remove the solvent. The dried coating was then roll pressed between twin rollers to improve adherence to the Al foil and then punched into 16-mm-diameter pieces. After drying the electrodes for 4 h under vacuum at 110 °C, the electrodes were assembled in half-cell configuration in 2016 coin cells, using 16-mm circular sodium metal pieces as the anode, separated by glass fibre (Whatman) swollen with sodium ion-conducting electrolyte. That electrolyte consisted of 1 M $NaClO_4$ (Sigma Aldrich, ≥98 %) in propylene carbonate (PC, Sigma Aldrich, ≥99.7 %). Electrochemical studies

were carried out via cyclic voltammetry using a BioLogic potentiostat, while galvanostatic testing were performed using a battery tester system (Neware). All capacities are reported in milliampere hour per gram ($mAhg^{-1}$), related to the mass of the active material. For $Na_{0.7}MnO_2$ with a molar mass of 102.41 $gmol^{-1}$, the extraction/insertion of 1 Na per formula unit is equivalent to 262 $mAhg^{-1}$.

Results and discussion

The crystal structure of P2-$Na_{0.7}MnO_2$ (space group $P6_3mmc$, see ref. [17] for the nomenclature) is depicted in Fig. 1. It consists of MnO_2 slabs made of edge-sharing MnO_6 octahedra. The sodium ions can occupy two different triangular prismatic sites in the plane between these MnO_2 slabs. Following a nomenclature introduced by Carlier et al. [30] for a similar system, these are marked as Na_f and Na_e in Fig. 1. For Na_f, the triangles of the prisms are also triangles of the octahedra above and below, whereas the triangles of the prisms around Na_e are formed by edges of three of the octahedra, respectively. Energetically, the two sites are not equivalent due to their differing number and distance of the $Mn^{3+/4+}$ ions surrounding the respective Na^+. The lower right corner of Fig. 1 exemplarily depicts a substituting CoO_6 octahedron as it appears in NCO. Based on the results of a neutron diffraction analysis published for P2-$Na_{2/3}Co_{1/3}Mn_{2/3}O_2$ [36], we assume that the lateral distribution of CoO_6 and MnO_6 octahedra within the slabs of our $Na_{0.7}Co_{0.11}Mn_{0.89}O_{2+z}$ does not obey any long-range order. As mentioned above, the MO_2 layers have about 1 % cation vacancies [16]. Such a vacancy is illustrated next to the MnO_6 octahedron in Fig. 1.

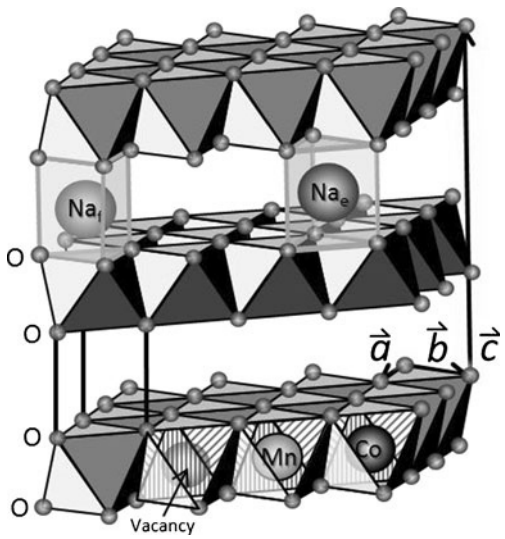

Fig. 1 Crystal structure of P2 layered Na_xMnO_2 and $Na_xCo_yMn_{1-y}O_2$. Two possible sites for intercalated Na and three possible ways of filling the octahedral sites (vacancy, Mn, Co) are shown (see text)

All peaks in the XRD patterns in Fig. 2 can be indexed to the layered P2 structure of Fig. 1. For the lattice vectors a, b, c, a Rietveld analysis yields the lattice parameters $a=b=2.872(2)$ Å and $c=11.167(2)$ Å for NMO, and $a=b=2.848(1)$ Å and $c=11.149(2)$ Å for NCO. FESEM images as those in Fig. 3 revealed that both NCO and NMO consist of flat hexagonal particles after synthesis. This fits to the layered crystal structure detected in XRD. The lateral dimensions (parallel to lattice vectors a and b) of the flakes in Fig. 3 are in the range between 300 and 600 nm, and their thickness (direction of lattice vector c) lies between 100 and 200 nm. Energy-dispersive X-ray spectroscopy confirmed Na, Mn, O, and (for NCO) Co as main constituents of the electrodes. Quantitative analysis revealed a ratio of cobalt to manganese of 1:6.7, resulting in a stoichiometry of $Na_{0.7}Co_{0.11}Mn_{0.89}O_{2+z}$ for NCO. Apart from the microstructure, the two samples also share the same specific surface area of ~50 m^2g^{-1} as measured by BET. In total, the two samples are essentially equal in crystal structure and morphology and thus provide an ideal model system to separately study the effect of the Co substituents in NCO on the electrochemical properties.

After assembly, the coin cells with either material had an open circuit voltage (OCV) of 2.65 V. This indicates that both cathodes have a comparable Na^+ content after synthesis. The voltage is close to the 2.8 V reported by Caballero for P2-$Na_{0.6}MnO_2$ obtained by a sol–gel method [21]. We rationalize our slightly lower OCV as a consequence of a higher Na^+ content of 0.7 as opposed to 0.6 in ref. [21]. As will be shown more below, both of our tested materials take up a charge of 56 $mAhg^{-1}$ when charged up to 3.8 V. This would be equivalent to an extrusion of 0.21 Na^+ per formula unit, i.e. forming $Na_{0.49}MnO_{2+z}$ and $Na_{0.49}Co_{0.11}Mn_{0.89}O_{2+z}$, respectively.

Figure 4 shows cyclic voltammograms (CVs) of NMO and NCO at a scan rate of 0.3 mVs^{-1} in the range between 1.5 and 3.8 V vs. Na | Na^+. Both CVs are dominated by a couple of

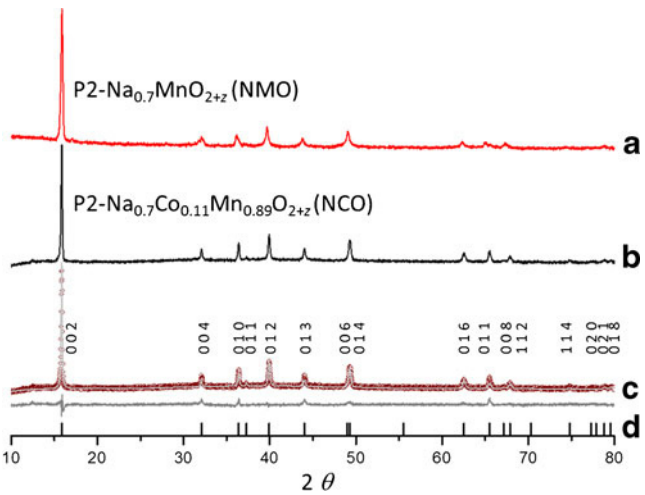

Fig. 2 XRD patterns of **a** NMO and **b** NCO. **c** Rietveld refinement of XRD pattern of NCO and **d** *hkl* positions of space group $P6_3mmc$

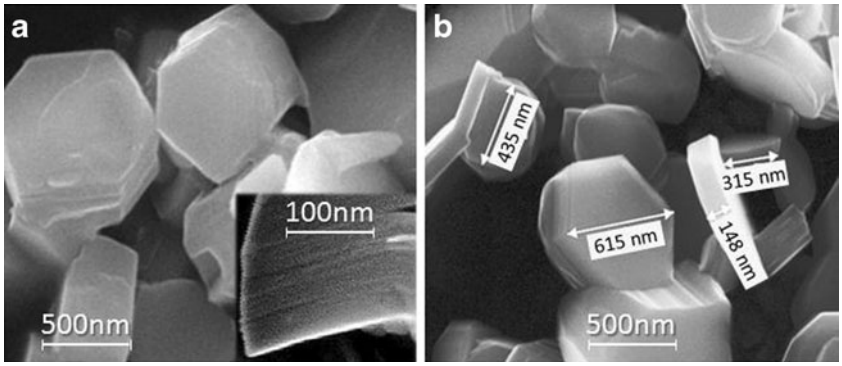

Fig. 3 FESEM images of NMO (**a**) and NCO (**b**); *inset* in (**a**) illustrates the layered structure

redox peaks between 2 and 2.5 V. Both peak positions and the apparent equilibrium potential are slightly more positive for NCO as compared to NMO. A main difference between the two voltammograms is the presence of manifold oxidation and reduction peaks for NMO in Fig. 4a as opposed to the rather smooth voltammogram of NCO in Fig. 4b. Similar features were previously shown in plots of the differential specific capacity of P2-$Na_{0.6}MnO_2$ [21] and also for monoclinic $NaMnO_2$ in potentiostatic intermittent titration patterns [23]. These features can be attributed to phase transitions similar to those intensely studied for P2-Na_xCoO_2 [29, 30, 37, 38]. These transitions do not concern the layered P2 backbone structure itself but the ordering of Na^+ and vacancies between the slabs, specifically their distribution among the two different triangular prismatic sites (see Fig. 1). Apart from the main redox couple, the most pronounced features in the CV in Fig. 4a are the two oxidation peaks A and B at 3.5 and 3.6 V, respectively. These features seem to be a common fingerprint for potentiostatic and galvanostatic charging of sodium layered oxides: they can be found, e.g. in the charging curves for P2-$Na_{0.6}MnO_2$ [21], monoclinic $NaMnO_2$ [23], P2-Na_xCoO_2 [29, 37], P2-$Na_xCo_{2/3}Mn_{1/3}O_2$ [30], or P2-$Na_x[Fe_{1/2}Mn_{1/2}]O_2$ [39]. For P2-Na_xCoO_2 [29, 37] and P2-$Na_xCo_{2/3}Mn_{1/3}O_2$ [30], this feature was already shown to be related to the transition into/out of the very stable phase for a Na^+ content of 0.5. For P2-$Na_{0.5}CoO_2$, experiments [40, 41] and calculations [37, 38, 42] revealed an equal occupancy of Na_e and Na_f sites. Though the Na^+/vacancy patterns for the corresponding manganese lamellar oxides are not yet known, similar ordered and stable structures must exist. As a last point related to the CV profiles in Fig. 4a and b, we would like to underline the similarity to the charging curves of P2-Na_xCoO_2 [29] and P2-$Na_xCo_{2/3}Mn_{1/3}O_2$ [30], where partial substitution of Co by Mn "erased" most of the features apart from the ones around 3.5 V. Our results show that a continuous increase of the Mn content towards P2-Na_xMnO_{2+z} eventually "revives" those features again. This can be explained as follows: The interaction of Na^+ ions with the chemically corrugated landscape of the doped oxides predominates over the interactions between the Na^+ ions. The latter is mainly responsible for the ordered patterns observed at specific Na^+ concentrations. Even for plain P2-Na_xMnO_{2+z}, the Na^+ ions can be expected to be in a chemically less homogeneous landscape as compared to P2-Na_xCoO_2. The cation vacancies in the MnO_2 layers (see Fig. 1) [16] act as effective negative charges that trap intercalated Na^+ ions [43] and thus disturb their arrangement into long-range ordered phases. This would explain why the voltammetric features observed in Fig. 4a are still relatively weak despite the good crystallinity of the cathode material.

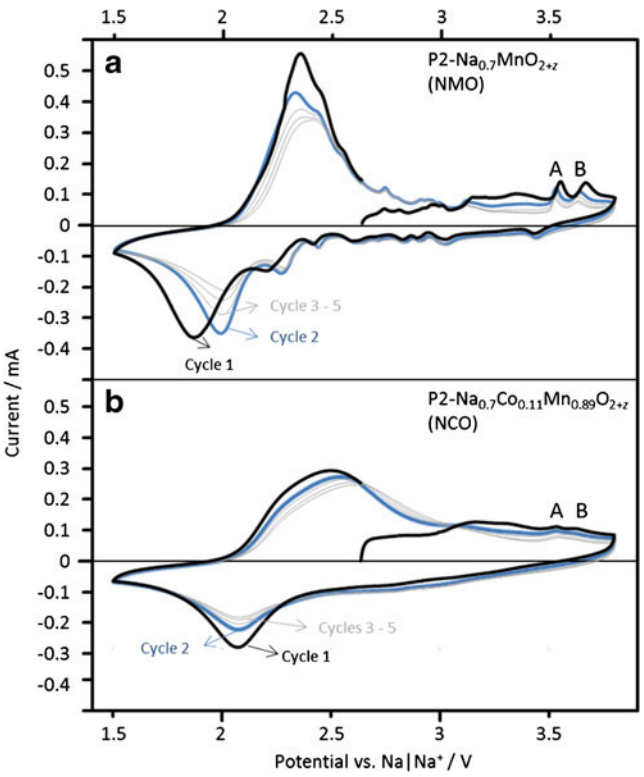

Fig. 4 Cyclic voltammograms of **a** NMO and **b** NCO (scan rate, 0.3 $mV s^{-1}$)

Figure 5 presents galvanostatic charge/discharge cycles of NMO and NCO at 0.3 C (50 $mA g^{-1}$) between 1.5 and 3.8 V vs. Na | Na^+. For NMO, two potential plateaus at 3.5 and 3.6 V are visible for all cycles. In analogy to the

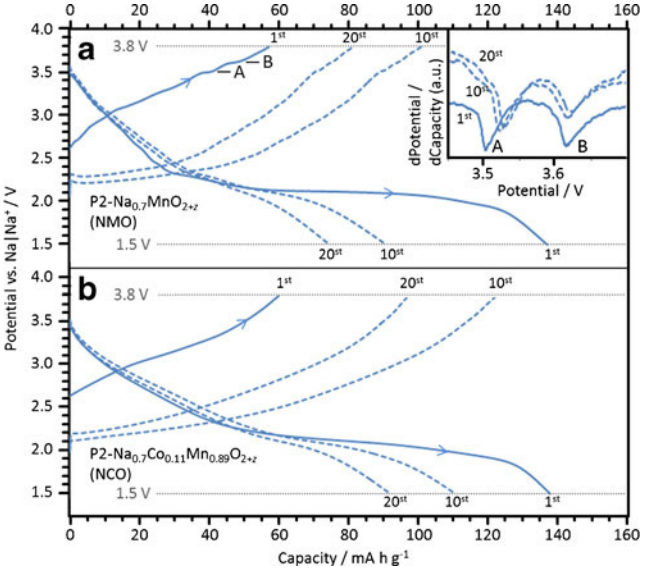

Fig. 5 Galvanostatic charge/discharge profiles of **a** NMO and **b** NCO at 0.3 C. First, 10th, and 20th cycles are shown. *Inset*: derivative of the charging curves in the range 3.45–3.7 V for better visibility of features *A* and *B*

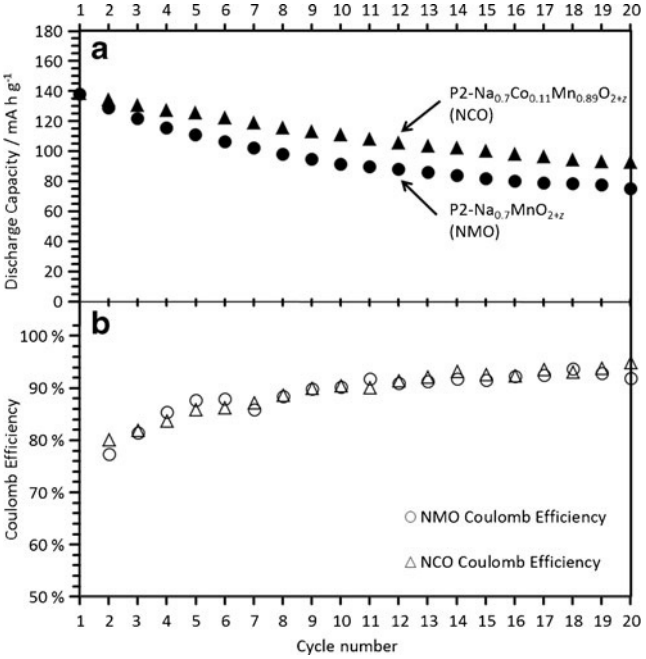

Fig. 6 **a** Integrated charge of galvanostatic discharge at 0.3 C for 20 cycles for both cathode materials; **b** Coulomb efficiencies (discharge capacity divided by preceding charge capacity) for cycles 2–20

respective features in the CVs in Fig. 4, these have been marked as A and B. For the second and all further cycles, the charge curves of NMO exhibit a long plateau at ~2.3 V as dominating features. In agreement to the CVs, the corresponding discharge plateau is at ~2.1 V. As to be expected from the much broader peaks in the CVs of NCO, the galvanostatic charge and discharge curves of that sample in Fig. 5b do not exhibit any pronounced plateaus. NMO and NCO both exhibit a discharge capacity of 138 $mAhg^{-1}$ after initial charging to 3.8 V. This is equivalent to the intercalation of 0.53 Na^+ per formula unit. The capacity is close to the values reported for P2-$Na_{0.6}MnO_2$ (140 $mAhg^{-1}$ [21]), P2-$Na_xCo_{2/3}Mn_{1/3}O_2$ and P2-Na_xCoO_2 (both 120 $mAhg^{-1}$ at C/100 [30]). Only monoclinic $NaMnO_2$, where up to 0.8 Na^+ per formula unit can be reversibly (de-)intercalated, has a significantly higher capacity of 185 $mAhg^{-1}$ (measured for C/10) [23].

After 20 cycles, NMO and NCO have a remaining capacity of 75 and 92 $mAhg^{-1}$, respectively. As illustrated in Fig. 6a, the decay in capacity becomes less steep with increasing cycle number for both cathode materials. This behaviour is different from that reported by Morales et al. for P2-$Na_{0.6}MnO_2$ [21], where the degradation seems to become faster with increasing number of cycles. Since their crystal structure should be the same as ours and the voltage range used in their cycles was even narrower, the most likely explanation for the better stability of our NMO is the electrode structure, specifically, the particle size. Whereas the flakes generated by our combustion method are all <1 μm (cf. Fig. 3), the particles in the cited work are >2 μm. Smaller particles are less sensitive to mechanical deformation due to Na^+ (de-)intercalation. This would explain why we observe a better stability, and it calls for a systematic optimization of the particle size in future studies. However, as Qu et al. [44] recently reported for α-$NaMnO_2$ used in asymmetric aqueous supercapacitors, high cycle efficiencies can also be achieved for larger particles. This might be a hint that part of the fading observed in our work is due to an interaction between the organic electrolyte and the active material.

An interesting quantity to consider in the context of capacity retention is the coulomb efficiency, i.e. the discharge capacity divided by the preceding charge capacity. Figure 6b shows that the coulomb efficiencies for both cathode materials are slowly increasing from 78 % in the second cycle to at most 95 % in the 20th cycle. There is no apparent difference between NMO and NCO with respect to these values. Similar behaviour, yet not quantified over many cycles, was reported for P2-$Na_{0.6}MnO_2$ [21], monoclinic $NaMnO_2$ [23], P2-$Na_xCo_{2/3}Mn_{1/3}O_2$ [30], and P2-Na_xCoO_2 [29]. The main contribution to the low coulomb efficiency comes from side reactions at higher potentials, e.g. electrolyte decomposition [13, 23]. Our results do not show any effect of Co doping on these parasitic reactions. Another possible reason for capacity fading could be the disproportionation of Mn^{3+} into Mn^{4+} and dissolved Mn^{2+}, which is a general problem of Mn containing cathodes. This hypothesis is substantiated by literature [1, 6] and is a key issue to be addressed in future works.

The better capacity retention for the doped sample fits to corresponding observations for the stability of substituted layered manganese oxides in lithium ion batteries [32]. It has to be pointed out, however, that the ion exchange of Na^+ towards Li^+ goes along with a transition of a P2 to an O2

structure [32] so that the structural boundary conditions cannot be directly compared. Moreover, the capacity fading of LIBs involving Li_xMnO_2 cathodes is mainly due to a gradual transition into an energetically favourable spinel crystal structure [45, 46]. This transition does not occur in NIBs [23]. The stabilizing effect of Co could involve more than one factor, similar to what was observed for spinel $LiCo_yMn_{2-y}O_4$ as compared to $LiMn_2O_4$ as cathodes in LIBs where Co was shown to improve the general chemical stability and the cation conductivity of the electrode [6].

Conclusions

The gelatin-assisted combustion method is ideal for the synthesis of P2-type layered sodium manganese oxides as well-defined model cathodes for rechargeable Na^+ ion batteries. These cathodes can be systematically varied by partial substitution of Mn by Co, Fe, Ni, Cu, Zn, and Al. The resulting powders consist of sub-micrometre flakes with a $P6_3mmc$ crystal structure. Being charged to 3.8 V vs. Na | Na^+, the cathodes based on those particles have a discharge capacity of 138 $mAhg^{-1}$, equivalent to the extrusion and re-insertion of ~0.5 Na. Due to the small size of the flakes, these capacities were attainable at a rate of 0.3 C. We have exemplarily shown that substitution by Co does not alter the capacity itself but has a beneficial effect on the cycling stability. Specifically, the capacity of the 20th discharge cycle (with 0.3 C) increases from 75 $mAhg^{-1}$ for $Na_{0.7}MnO_{2+z}$ to 92 $mAhg^{-1}$ for $Na_{0.7}Co_{0.11}Mn_{0.89}O_{2+z}$. An effect of Co doping towards improved cycle efficiency via suppression of parasitic side reactions, however, can be excluded. Cyclic voltammograms indicate that the presence of Co suppresses the formation of ordered Na^+/vacancy phases which is likely to have an influence on the Na^+ transport within the cathode. Further studies will reveal in how far this behaviour directly contributes to the observed cycle life improvement. Moreover, a systematic study on the optimum particle size for plain and doped Na_xMnO_2 is on its way.

Acknowledgments The authors would like to thank Miss Han-Yi Chen, Miss Yin Ting Teng, and Mr. Jan Geder for their valuable help in conducting SEM, XRD, and BET measurements. This work was financially supported by the Singapore National Research Foundation under its Campus for Research Excellence and Technological Enterprise (CREATE) programme.

References

1. Wu Y, Wan C, Jiang C, Fang S (2002) Introduction, principles and advances of lithium secondary batteries. Tsinghua University Press, Beijing
2. Scrosati B, Garche J (2010) J Power Sources 195:2419–2430
3. Liu C, Li F, Ma L, Cheng H (2010) Adv Mater 22:E28–E62
4. Ceder G, Hautier G, Jain A, Ong SP (2012) MRS Bull 37:185–191
5. Vetter J, Novák P, Wagner MR, Veit C, Möller K-C, Besenhard JO, Winter M, Wohlfahrt-Mehrens M, Vogler C, Hammouche A (2005) J Power Sources 147:269–281
6. Wu YP, Rahm E, Holze R (2002) Electrochim Acta 47:3491–3507
7. Liu L, Tian F, Zhou M, Guo H, Wang X (2012) Electrochim Acta 70:360–364
8. Qu Q, Fu L, Zhan X, Samuelis D, Maier J, Li L, Tian S, Li Z, Wu Y (2011) Energy Environ Sci 4:3985
9. Tang W, Liu LL, Tian S, Li L, Li LL, Yue YB, Bai Y, Wu YP, Zhu K, Holze R (2011) Electrochem Commun 13:1159–1162
10. Ellis BL, Nazar LF (2012) Curr Opin Solid State Mater Sci 16:168–177
11. Chevrier VL, Ceder G (2011) J Electrochem Soc 158:A1011–A1014
12. Ellis BL, Makahnouk WRM, Makimura Y, Toghill K, Nazar LF (2007) Nat Mater 6:749–753
13. Kim S-W, Seo D-H, Ma X, Ceder G, Kang K (2012) Adv Energy Mater 2:710–721
14. Palomares V, Serras P, Villaluenga I, Hueso KB, Carretero-González J, Rojo T (2012) Energy Environ Sci 5:5884–5901
15. Tarascon J-M, Armand M (2001) Nature 414:359–367
16. Parant J-P, Olazcuaga R, Devalette M, Fouassier C, Hagenmuller P (1971) J Solid State Chem 3:1–11
17. Delmas C, Fouassier C, Hagenmuller P (1980) Physica B+C 99:81–85
18. Doeff MM, Anapolsky A, Edman L, Richardson TJ, De Jonghe LC (2001) J Electrochem Soc 148:A230–A236
19. Eriksson TA, Lee YJ, Hollingsworth J, Reimer JA, Cairns EJ, Zhang X, Doeff MM (2003) Chem Mater 15:4456–4463
20. Mendiboure A, Delmas C, Hagenmuller P (1985) J Solid State Chem 57:323–331
21. Caballero A, Hernán L, Morales J, Sánchez L, Santos Peña J, Aranda MAG (2002) J Mater Chem 12:1142–1147
22. Shao-Horn Y (1999) J Electrochem Soc 146:2404–2412
23. Ma X, Chen H, Ceder G (2011) J Electrochem Soc 158:A1307–A1312
24. Kim H, Kim D, Seo D, Yeom M, Kang K, Kim DK, Jung Y (2012) Chem Mater 24:1205–1211
25. Tarascon J, Guyomard D, Wilkens B (1992) Solid State Ionics 57:113–120
26. Sauvage F, Laffont L, Tarascon J-M, Baudrin E (2007) Inorg Chem 46:3289–3294
27. Yang S, Wang X, Wang Y, Chen Q, Li J, Yang X (2010) T Nonferr Metal Soc 20:1892–1898
28. Chick LA, Pederson LR, Maupin GD, Bates JL, Thomas LE, Exarhos GJ (1990) Mater Lett 10:6–12
29. Berthelot R, Carlier D, Delmas C (2011) Nat Mater 10:74–80
30. Carlier D, Cheng JH, Berthelot R, Guignard M, Yoncheva M, Stoyanova R, Hwang BJ, Delmas C (2011) Dalton Trans 40:9306–9312
31. Dollé M, Hollingsworth J, Richardson TJ, Doeff MM (2004) Solid State Ionics 175:225–228
32. Dollé M, Patoux S, Doeff MM (2005) Chem Mater 17:1036–1043
33. Rietveld HM (1969) J Appl Crystallogr 2:65–71
34. Rietveld HM (1967) Acta Crystallogr 22:151–152
35. Cheary RW, Coelho A (1992) J Appl Crystallogr 25:109–121
36. Lu Z, Donaberger RA, Dahn JR (2000) Chem Mater 12:3583–3590
37. Shu G, Prodi A, Chu S, Lee Y, Sheu H, Chou F (2007) Phys Rev B Condens Matter 76:184115
38. Meng YS, Hinuma Y, Ceder G (2008) J Chem Phys 128:104708

39. Yabuuchi N, Kajiyama M, Iwatate J, Nishikawa H, Hitomi S, Okuyama R, Usui R, Yamada Y, Komaba S (2012) Nat Mater 11:512–517
40. Huang Q, Foo ML, Lynn JW, Zandbergen HW, Lawes G, Wang Y, Toby BH, Ramirez AP, Ong NP, Cava RJ (2004) J Phys Condens Matter 16:5803–5814
41. Zandbergen H, Foo M, Xu Q, Kumar V, Cava R (2004) Phys Rev B Condens Matter 70:024101
42. Zhang P, Capaz R, Cohen M, Louie S (2005) Phys Rev B Condens Matter 71:153102
43. Robertson AD, Armstrong AR, Bruce PG (2001) Chem Mater 13:2380–2386
44. Qu QT, Shi Y, Tian S, Chen YH, Wu YP, Holze R (2009) J Power Sources 194:1222–1225
45. Wohlfahrt-Mehrens M, Butz A, Oesten R, Arnold G, Hemmer RP, Huggins RA (1997) J Power Sources 68:582–585
46. Robertson AD, Armstrong AR, Paterson AJ, Duncan MJ, Bruce PG (2003) J Mater Chem 13:2367–2373

4.2 Layered Na_xMnO_{2+z} in Sodium-Ion Batteries – Influence of Morphology on Cycle Performance

This chapter is a summary of the publication "Layered Na_xMnO_{2+z} in Sodium Ion Batteries – Influence of Morphology on Cycle Performance" (ACS Applied Materials & Interfaces **2014**, *6*, 8059-8065), which is the continuation of the work on sodium manganese oxides as NIB cathodes. N. Bucher was leading the work that is presented in this publication.

The basic principle of energy storage of NIBs is (de-)insertion of Na-ions into (from) a crystal structure. This incorporation of Na^+ into a given lattice is accompanied by a volume change of the unit cell. During cycling, this leads to repeated expansion and contraction of the unit cell, which results in structural stress which can have an influence on the long-range order of the material, and therefore on cycling stability. Thus, one approach to enhance cycling stability is to accommodate these volume changes of the unit cell. This publication reports for the first time on the effect of morphology on the electrochemical properties of $Na_{0.7}MnO_{2+z}$ (NMO). In this work a new wet-chemical approach to synthesise hollow NMO spheres has been introduced; the diameter of the obtained spheres is approximately 5 µm; NMO flakes were prepared via combustion synthesis as in the previous Chapter 4.1. Both spheres and flakes were synthesised in the same layered P2-type structure, even though crystallinity was higher for the flakes. Potentiostatic measurement revealed the same behaviour for the spheres as previously observed for the flakes – one major transition at 2.2 / 2.5 V *vs*. $Na|Na^+$, and several peaks at higher potentials (voltage range of 1.5 – 3.8 V *vs*. Na). However, these minor peaks are significantly more pronounced for the spheres, indicating that a higher amount of charge is transferred during the respective process. This is confirmed by galvanostatic measurements. The minor plateaus at voltages above 2.5 V *vs*. $Na|Na^+$ are more distinct; as the underlying processes are better exploited, the weight-normalised charge, *i.e.* capacity, is higher for the spheres than for the flakes. While the flakes provide an initial discharge capacity of 140 mA h g^{-1} at a current rate of 50 mA g^{-1}, the respective value for the spheres is 160 mA h g^{-1}.

This advantage with regard to capacity could be observed for various current rates ranging from 20 mA g^{-1} to 800 mA g^{-1}. Moreover, it is preserved over the course of cycling. While the flakes exhibit a capacity of 73 mA h g^{-1} after 100 cycles, the spheres still provide 94 mA h g^{-1} (50 mA g^{-1}). Possible reasons for this are better accommodation of the volume changes during charge/discharge for the spheres than for the flakes as a consequence of the spherical morphology, or a better penetration of the electrode with electrolyte and more uniform mixing as a result of the spherical morphology.

In order to investigate the effect of morphology on the extent to which repeated volume changes led to degradation of the morphological integrity of the $Na_{0.7}MnO_2$, SEM pictures of both flake-like and spherical material after 100 cycles were taken. Thus, it could be confirmed that, while the flakes seemed to have fused together, the spheres were still intact; *i.e.* their morphology was retained throughout cycling.

The spherical NMO material presented in this work was subsequently shown to be suitable for a full-cell setup combined with a $Na_6V_{10}O_{28}$ polyoxometalate as anode in a different puplication.[27]

Even though *ex-situ* XRD measurements indicated that the pristine structure is largely maintained for both materials during cycling, structural reasons for the difference in capacity and cycling stability could not be excluded.

In summary, a positive effect of morphology optimisation on capacity and cycling stability has been shown for the P2-layered manganese oxides for the first time. A two-step synthesis route to obtain the spherical morphology of this material class was introduced for NIB materials. The spherical morphology was preserved better over the course of cycling than the flake-like morphology. Suggested reasons for this improvement are better accommodation of volume changes, enhanced penetration of the electrode material by the electrolyte and better electrical contact in the electrode.

Layered Na_xMnO_{2+z} in Sodium Ion Batteries–Influence of Morphology on Cycle Performance

Nicolas Bucher, Steffen Hartung, Arun Nagasubramanian, Yan Ling Cheah, Harry E. Hoster and Srinivasan Madhavi

The publication can be found under the following weblink:

http://dx.doi.org/10.1021/am406009t

ACS APPLIED MATERIALS & INTERFACES

Research Article

www.acsami.org

Layered Na_xMnO_{2+z} in Sodium Ion Batteries—Influence of Morphology on Cycle Performance

Nicolas Bucher,[∥,†,‡] Steffen Hartung,[∥,†,‡] Arun Nagasubramanian,[†,§] Yan Ling Cheah,[§] Harry E. Hoster,[†,‡] and Srinivasan Madhavi*[,†,§]

[†]TUM CRREATE, Singapore 138602, Singapore

[‡]Technische Universität München, 85748 Garching, Germany

[§]School of Materials Science and Engineering, Nanyang Technological University, Singapore 639798, Singapore

Supporting Information

ABSTRACT: Due to its potential cost advantage, sodium ion batteries could become a commercial alternative to lithium ion batteries. One promising cathode material for this type of battery is layered sodium manganese oxide. In this investigation we report on the influence of morphology on cycle performance for the layered Na_xMnO_{2+z}. Hollow spheres of Na_xMnO_{2+z} with a diameter of ~5 μm were compared to flake-like Na_xMnO_{2+z}. It was found that the electrochemical behavior of both materials as measured by cyclic voltammetry is comparable. However, the cycle stability of the spheres is significantly higher, with 94 mA h g^{-1} discharge capacity after 100 cycles, as opposed to 73 mA h g^{-1} for the flakes (50 mA g^{-1}). The better stability can potentially be attributed to better accommodation of volume changes of the material due to its spherical morphology, better contact with the added conductive carbon, and higher electrode/electrolyte interface owing to better wetting of the active material with the electrolyte.

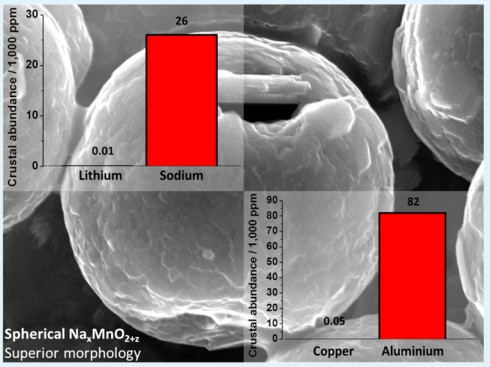

KEYWORDS: *sodium ion battery, energy storage, sodium manganese oxide, spheres, morphology*

1. INTRODUCTION

Electrochemical energy storage technologies have become an important field of research, as the need to flexibly store electricity has greatly increased over the last years. This can be seen in a variety of areas in everyday life, from portable consumer electronics like laptops and smartphones, electrically powered vehicle to boost electro mobility, to the need of large-scale energy storage to smoothen erratic fluctuations of electricity generated by renewable sources.

Over the last years and decades, the intercalation-based lithium ion battery (LIB) technology has been at the centre of this research, due to its high power density and capacity. However, as the necessity for flexible and affordable energy storage pervades more and more areas, relying on this technology might pose several problems. First, with a crustal abundance of 10 ppm,[1] lithium resources are limited, and hence, it is uncertain whether these resources can sustain a considerably elevated demand. Moreover, as LIBs are already a relatively expensive technology, a significantly higher demand could increase prices even further. Therefore, research has recently also focused on alternative energy storage technologies. One promising candidate is sodium ion batteries (NIB). NIB is based on the same working principle as LIB but uses sodium as the electroactive species.[2−7] With a crustal abundance of sodium of 26 000 ppm, (see abstract graphic)[1] both availability and price make NIB a promising option to complement (or even eventually replace) LIB in certain areas. Furthermore, in contrast to LIB which uses copper as anode current collector, NIB can use the cheaper and more abundant Al, as it does not alloy with Na.[8−10] However, one inherent disadvantage is that sodium compounds usually provide lower performance. Several classes of cathode materials have been studied in the field of NIB. $NaFePO_4$ provides a high cycle stability and acceptable capacity.[11] Different (sodium) vanadium oxides were studied and show promising performances. NaV_6O_{15}, for example, provides 142 mA h g^{-1}, and NaV_3O_8 delivers a capacity of 200 mA h g^{-1}.[12−17] Jian et al. recently showed that $Na_3V_2(PO_4)_3$ is a promising material,[18] and Xu et al. published a study on $Na_3V_2O_2(PO_4)_2F$/graphene, which shows a high intercalation potential (>3.5 V), combined with a good capacity and stability.[19] Layered oxides are among the most promising materials to deliver the performance required for practical applications.[20−31] Vassilaras et al., for example, recently reported approximately 160 mA h g^{-1} for $NaNi_{1/3}Co_{1/3}Fe_{1/3}O_2$,[32] and Wang et. al. published a work of $Na_{0.66}[Li_{0.22}Ti_{0.78}]O_2$ as an anode material with a low volume change, in which they also studied the position of Na in the interlayer.[33] Within this class of materials, sodium manganese

Received: December 27, 2013
Accepted: May 12, 2014
Published: May 12, 2014

   dx.doi.org/10.1021/am406009t | ACS Appl. Mater. Interfaces 2014, 6, 8059−8065

based oxides have received special attention, as manganese is relatively abundant.[1] Furthermore, these compounds have shown that they are able to deliver considerable capacities.[34−37]

Various attempts have been made to improve specific characteristics (e.g., cycle stability) by partially substituting manganese with other transition metals like Co, Ni, or Fe.[10,37−39] Yabuuchi et al., for example, reported good capacities and stabilities for $Na_xFe_{1/2}Mn_{1/2}O_2$.[10]

A different approach to decrease capacity fading is optimization of the morphology. Hollow spherical nanostructured morphologies possess favorable characteristics such as high surface-to-volume ratio, low density and low coefficients of thermal expansion as compared to their bulk micrometer sized counterparts. For example it has been shown that for $LiNi_{0.5}Mn_{1.5}O_4$, $LiMn_2O_4$, and $ZnMn_2O_4$ spherical particles considerably enhance cycle stability in LIB applications.[40−43]

In this publication, we demonstrate that this approach is beneficial in the field of sodium ion batteries, in general, and sodium manganese oxides in particular. For this purpose, we will first describe the synthesis of spherical sodium manganese oxides along with physical characterization studies such as X-ray diffraction (XRD), scanning electron microscopy (SEM), and transmission electron microscopy (TEM).We have evaluated the electrochemical performance of this material and compared it to a sodium manganese oxide that has been synthesized through a different route, which yielded a flake-like morphology. We present in this work the effect of morphology on the electrochemical performance of sodium manganese oxide (NMO) in sodium ion batteries.

2. EXPERIMENTAL SECTION

2.1. Synthesis. Spherical NMO was synthesized using spherical MnO_2 as precursor, which was synthesized according to a slightly modified procedure described by Li et al.[44] Spherical MnO_2 was synthesized by first dissolving NH_4HCO_3 in deionized water. Then, a small amount of ethanol (10% volume of the NH_4HCO_3 solution) and a solution of $MnSO_4$ in deionized water was added dropwisely. During the subsequent stirring at room temperature, spherical $MnCO_3$ was forming. The precipitate was filtrated, washed repeatedly with water and ethanol, and afterwards annealed in air for 5 h at 400 °C to give spherical MnO_2. Next, this was added to a solution of NaOH in deionized water and ethanol to give a dispersion. Both water and ethanol were evaporated, and the residue was annealed in air for 3 h at 320 °C, followed by 4 h at 800 °C to give the targeted spherical sodium manganese oxide.

Flake-like NMO was synthesized as described previously by our group.[37] Sodium nitrate (Sigma-Aldrich, ≥99%), manganese acetate (Alfa Aesar, anhydrous, 98%), and gelatin were dissolved in deionized water and nitric acid (≥69%, Honeywell). The solution was heated to 250 °C until spontaneous combustion set in. Subsequently, the product was annealed in air for 4 h at 800 °C to give the flake-like NMO.

2.2. Characterization. The crystal structures of the products were verified by powder X-ray diffraction, using a Bruker X-ray diffractometer with Cu Kα radiation. 2θ was varied within a range of $10° < 2\theta < 80°$, using a step size of 0.02° and 0.9 s per step. The Topas software (version 3) was used to conduct a phase analysis. The product morphologies were analysed by field emission scanning electron microscopy (FESEM, JEOL JSM-7600F) and transmission electron microscopy (TEM, JEOL 2100F, 200 kV). Elemental compositions were determined by micro X-ray fluorescence analysis (XRF, Bruker/M4 Tornado), using Rh as X-ray source (50 kV, 200 μm).

2.3. Electrochemistry. The composite electrodes were prepared by mixing NMO with acetylene black (Alfa Aesar, > 99%) and polyvinylidene fluoride (PVDF, Arkema, Kynar HSV 900) binder in the weight ratio 60:20:20 with *N*-methyl-2-pyrrolidone (NMP) to form a homogeneous slurry. This mixture was coated on an Al foil using a doctor blade; the coating was dried in air at 80 °C to remove the NMP. The coating was punched into pieces with a diameter of 16 mm, which were then roll-pressed, so that the electrodes prepared from flake-like and spherical NMO had comparable packing densities. Subsequently, they were dried at 110 °C under vacuum. These electrodes were then assembled in 2016 coin cells with circular metallic sodium pieces with a diameter of 16 mm as the anode, and glass fibre (Whatman) as the separator. A 1M solution of $NaClO_4$ (Sigma-Aldrich, ≥98%) in a mixture of ethylene carbonate and propylene carbonate (1:1 wt %; EC, Sigma-Aldrich, 99%; PC, Sigma-Aldrich, ≥99.7%) was employed as electrolyte. Cyclic voltammetry was measured using a BioLogic potentiostat, and a Neware battery tester was used for galvanostatic charge/discharge tests.

3. RESULTS

3.1. Morphology and Structure. Spherical MnO_2 (Figure 1a and b) was synthesized as a precursor for spherical NMO. The MnO_2 spheres are approximately 5 μm in diameter and

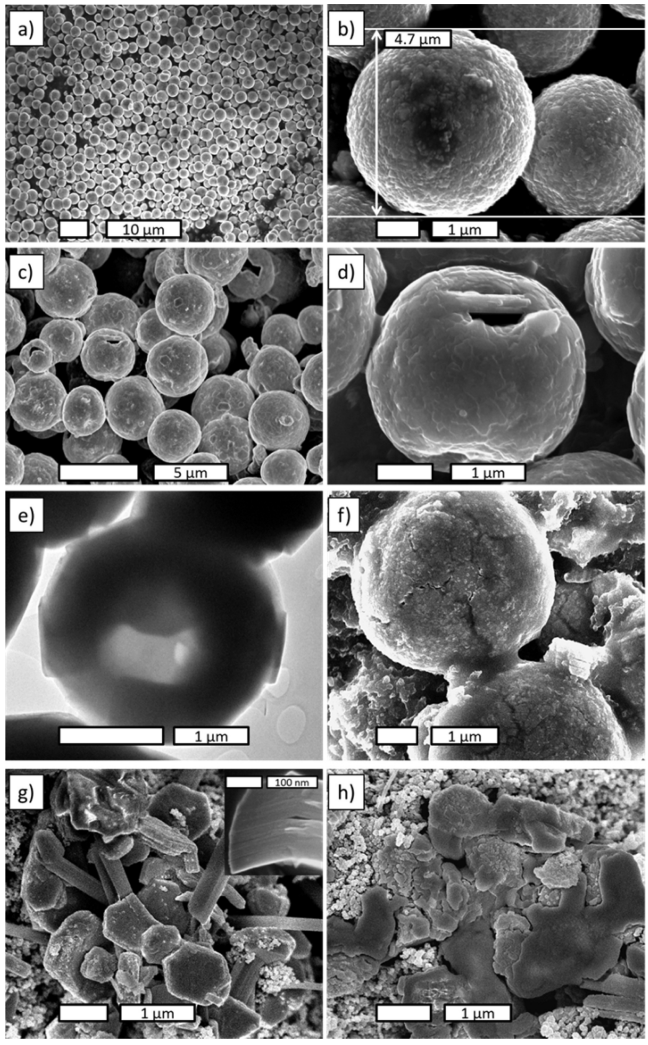

Figure 1. (a and b) SEM image of spherical MnO_2, (c and d) SEM image of spherical NMO, (e) TEM image of spherical NMO, (f) SEM image of a spherical NMO electrode after 100 cycles, surrounded by PVDF binder and acetylene black, (g) SEM image of flake-like NMO electrode before cycling, (h) SEM image of a flake-like NMO electrode after 100 cycles, surrounded by PVDF binder and acetylene black.

dx.doi.org/10.1021/am406009t | ACS Appl. Mater. Interfaces 2014, 6, 8059−8065

consist of fused, cubic crystallites. Sodium manganese oxide maintains this morphology (Figure 1c). However, during the synthesis process, some of the spheres seem to have opened up. Thus, a cross-section became visible (Figure 1d), indicating that the spheres are hollow, and that the shells are composed of sodium manganese layers with a thickness of several hundred nanometers. TEM pictures (Figure 1e) confirm that the spheres are hollow. Moreover, they indicate polycrystallinity of the material. After 100 cycles, the morphology is maintained (Figure 1f). Although minor cracks are visible, the spheres are preserved. The flakes, however, do not maintain their initial morphology. Figure 1g shows flake-like NMO on an electrode; after 100 cycles (Figure 1h), the flakes appear degraded and fused, indicating that morphology is degrading during cycling. The flake-like NMO shows the same morphology as described previously, that is, layered flakes with a cross-section of several hundred nanometers (see inset in Figure 1g).[37] BET measurements showed a comparable surface area of approximately 5 m^2 g^{-1}. However, the macropores in the spheres (Figure 1d, e) can contribute to better wetting of the active material with electrolyte.

For both morphologies, NMO was synthesized in the layered P2 structure (space group $P6_3mmc$). The crystal structure consists of layers of MnO_6 octahedra, while the sodium ions occupy two different triangular prismatic sides in between these layers. This was confirmed by XRD measurements (Figure 2).

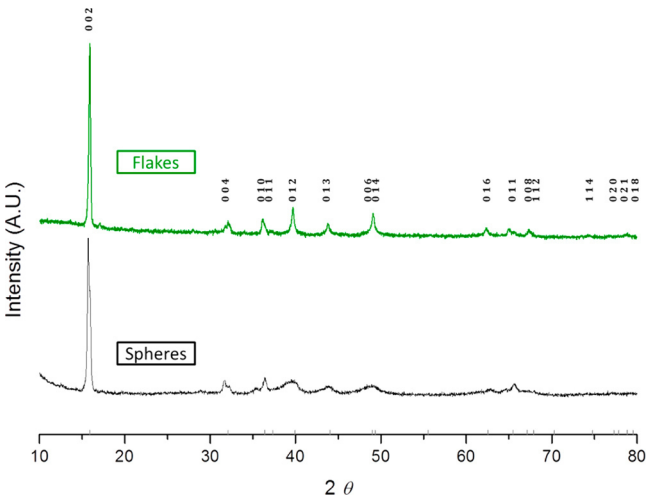

Figure 2. XRD pattern of the flake-like and spherical NMO.

The patterns for layered and spherical NMO, which were synthesized via similar annealing procedures, show that both materials have the same phase, albeit the flakes are more crystalline than the spheres. The crystallite size of the flakes, as estimated by the Debye–Scherer equation on the peak half maximum for different peaks, exceeds the crystallite size of the spheres (22–36 nm vs 4–20 nm). P2-type sodium manganese oxide occurs in the α and the β form. The XRD pattern of the synthesized spherical material corresponds to the α form; the additional small impurity peak at $2\theta = 32°$ can be attributed to the β form. As the oxygen content slightly varies for these two different forms, we write the chemical formula as Na_xMnO_{2+z}, with $0 \leq z \leq 0.25$.[45] XRF measurements showed that, initially, $x = 0.8$ for the spheres, and $x = 0.6$ for the flakes. The unit cell volume changes, according to Patoux et al., by approximately 1% upon (de-)insertion of 0.1 Na.[46]

3.2. Electrochemistry. Figure 3d shows the cyclic voltammogram (CV) of spherical NMO at a scan rate of 0.1 mV s^{-1}, which is remarkably similar to the CV of the layered NMO discussed earlier.[37] The main oxidation peak occurs around 2.45 V, and the corresponding reduction peak around 2.22 V. At higher voltages, several oxidation and reduction peaks are visible, which can mainly be attributed to phase transitions due to ordering process of the sodium ions between the two different triangular prismatic sites.

In the cycling profile of spherical NMO for 50 mA g^{-1}, as can be seen in Figure 3a, the significant peaks that can be seen in the CV can be observed as well. The dominating feature is the plateau around 2.3 V. As the half-cell is charged first, a certain amount of sodium is removed from the NMO structure. The observed capacity in the first charge is 47 mA h g^{-1}, which corresponds to 0.27 Na^+ per formula unit. The structure of this material varies with its sodium content—from the structure at hand, Na^+ can be removed until a stoichiometry of ca. $Na_{0.44}$ is reached.[45] Thus, in the first charge Na^+ can potentially be removed from the structure with the initial composition only until this barrier, which is why the capacity is rather low. Upon discharge, the structure is filled with sodium, which is removed in subsequent charge cycles. Thus, subsequent charge capacities are considerably higher. The first discharge capacity is 161 mA h g^{-1}, which decreases to 120 mA h g^{-1} after 50, and 94 mA h g^{-1} after 100 cycles.

Flake-like NMO shows a slightly lower capacity for both initial charge (34 mA h g^{-1}) and discharge (140 mA h g^{-1}) as compared to the spherical NMO. These values for initial discharge capacities for both spherical and flake-like NMO are comparable to previously reported capacities of layered oxides.[35,37,39] The initial charge capacity of the NMO flakes is slightly decreased as compared to our previous work,[37] which hints at a lower initial sodium content. However, as the (de-)insertion of Na^+ is reversible, this difference should be compensated upon the first charge. Similarly, as both the spheres and the flakes were first charged, a common baseline is created as all the sodium that can be deinserted from this P2 structure in this voltage range is removed, so that after the first charge the Na-content for spheres and flakes should be similar. For our experiments, the electrolyte used was a mixture of ethylene carbonate and propylene carbonate (1:1 wt %), which resulted in a better cycle stability as compared to the previously reported electrolyte without ethylene carbonate. For the flakes, a discharge capacity of 87 mA h g^{-1} was observed after 50 cycles, and 73 mA h g^{-1} after 100 cycles (see Figure 4). After 20 cycles, a capacity of 105 mA h g^{-1} can be achieved, which indicates a better stability than previously reported NMO.[37] This can probably be attributed to the addition of ethylene carbonate to the electrolyte.[47−49]

However, a significant difference in cycle stability can be seen between the spherical and the flake-like NMO, with the spheres providing 120 mA h g^{-1} after 50 cycles as opposed to 87 mA h g^{-1} for the flakes, and 94 mA h g^{-1} as compared to 73 mA h g^{-1} after 100 cycles, respectively (Figure 4). Thus, a higher capacity can be maintained for the spherical morphology.

Moreover, more pronounced plateaux at higher voltages (i.e., above 2.3 V) were observed when changing the morphology from flake-like to spherical (Figure 3b). Thus, it seems that transformations occurring at these voltages can be better addressed and exploited with hollow spheres. As can be seen in the direct comparison of the cyclic voltammograms of spherical and flake-like NMO (0.1 mV s^{-1}, Figure 3d), both materials

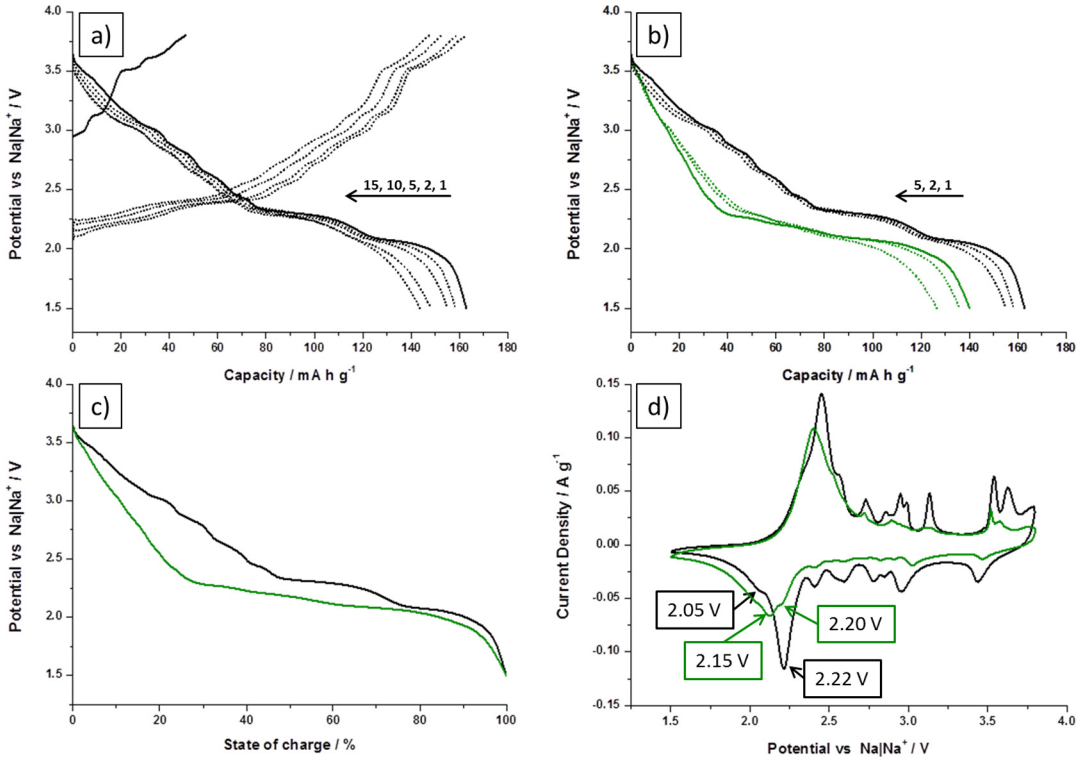

Figure 3. (a) Charge/discharge profile of spherical NMO at 50 mA g^{-1}; half-cell vs Na in 1 M $NaClO_4$ in propylene carbonate/ethylene carbonate (1:1 wt %); (b) discharge profile of spherical (black) and flake-like (green) NMO at 50 mA g^{-1}; (c) state of discharge profile of spherical (black) and flake-like (green) NMO, (d) cyclic voltammogram of spherical (black) and flake-like (green) NMO at 0.1 mV s^{-1}.

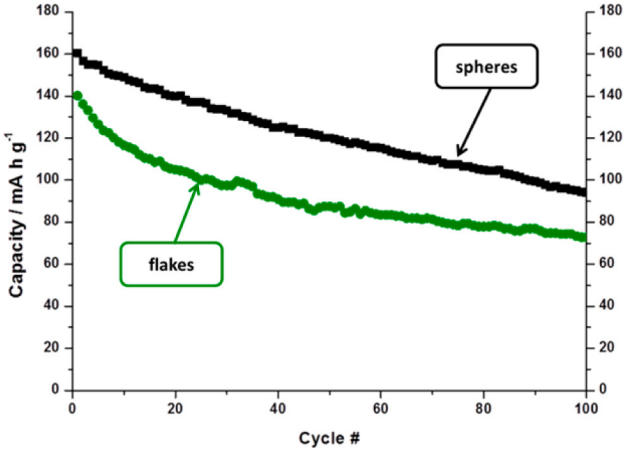

Figure 4. Cycling behavior of NMO at 50 mA g^{-1}; black, spherical; green, flake-like.

exhibit the same peaks, although they are significantly more pronounced for the hollow spheres, which corresponds to the discharge profiles. Thus, similar redox reactions, phase transformations or ordering processes occur in both materials; they are not suppressed in the flake-like material. An interesting feature in these CVs is that for the hollow spheres, the main reduction peak occurs at 2.22 V with a small shoulder peak at 2.05 V, whereas for the flakes the main peak is at 2.15 V with a small shoulder peak at 2.20 V. Even though a small shift can be attributed to polarization effects, it is noticeable that the peak intensity seem to have switched: a main peak with a shoulder at a higher voltage for the flakes, and a shoulder peak with a main peak at a higher voltage for the spheres.

This, together with the increased total capacity, results in an increase in energy density. The energy density was increased from 322 W h kg^{-1} (flakes) to 408 W h kg^{-1} (spheres), which corresponds to an increase of 27%. When normalized to state of discharge (Figure 3c), it can be seen that this increase is to a large extend (34%) attributable to a better exploitation of insertion processes, resulting in increased capacity for these processes.

Moreover, the hollow spheres also show remarkable capacities at higher current rates (Figure 5). Although the initial capacities decrease with increasing current rate, capacities seem to converge after 100 cycles. Therefore, this material is well suitable for applications for which fast discharge is

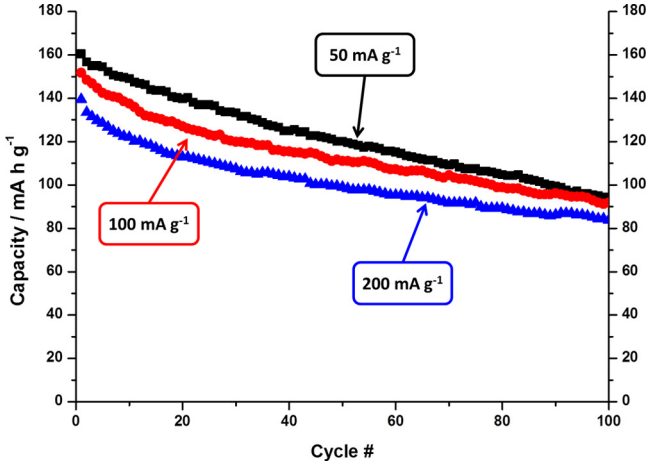

Figure 5. Cycling behavior of spherical NMO at different current rates.

dx.doi.org/10.1021/am406009t | ACS Appl. Mater. Interfaces 2014, 6, 8059−8065

necessary. The influence of current rate on capacity can be seen in Figure 6 for both flake-like and spherical NMO.

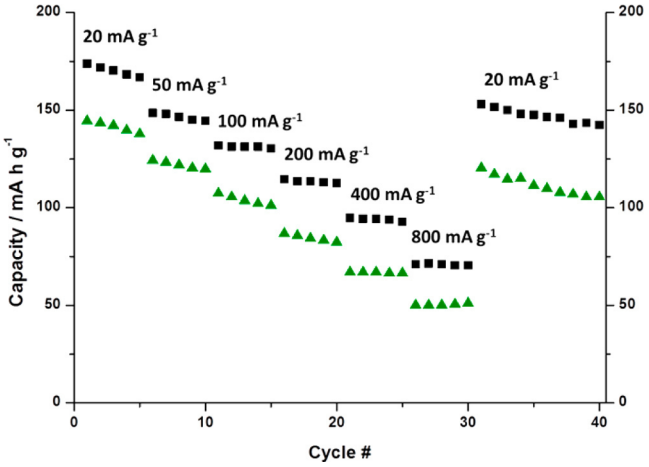

Figure 6. Cycling behavior of NMO; black (upper curve), spherical; green (lower curve), flake-like.

This conclusion that hollow spheres exhibit a higher cycle stability than other morphologies has also been found for materials of other chemical compositions.[41−43] Several arguments for this behavior have been introduced. First, hollow spheres can more easily accommodate the volume change that is inherently caused by the (de-)insertion of lithium or sodium into (from) the host structure. Thus, morphology is maintained over a longer time, resulting in higher cycle stability. Especially for sodium (de-)insertion, which distorts the structure to an even greater extent, this characteristic is highly significant. This assumption has been verified by opening a cell that had been cycled for 100 cycles at 200 mA g^{-1} and examining the morphology. As can be seen from Figure 1f, the spherical morphology is retained throughout cycling Thus, the inherent advantages of this morphology are retained as well. Moreover, as opposed to bulk materials, hollow spheres distinguish themselves through singular particles with defined boundaries, which enhances uniform mixing with the added conductive carbon. This could lead to a longer-lasting contact between the active material and the necessary conductive carbon, resulting in better cycle stability. Another effect is that the electrolyte penetration is enhanced, and thus, the diffusion pathway for sodium ions is shortened. Better crystallinity can be ruled out as a potential factor for the superior performance of the spheres as crystallinity is higher for the flakes (see section 3.1). As shown previously, cycle stability can potentially be improved even further by partially substituting manganese with other metals, such as cobalt.[37]

4. CONCLUSION

Different synthesis routes that yield different morphologies of sodium manganese oxide were explored. Specifically, flake-like and spherical sodium manganese oxide with the same P2-type crystal structure were obtained. Both materials show the same electrochemical behavior as measured by cyclic voltammetry, while the spheres provide slightly higher discharge capacities (140 vs 161 mA h g^{-1}, respectively) for a current rate of 50 mA g^{-1}. After 100 cycles, a higher discharge capacity could be maintained for the hollow spheres (94 mA h g^{-1} as opposed to 73 mA h g^{-1}). Moreover, energy density could be increased by 27%, due to an increase in capacity, especially based on more pronounced plateaux at higher voltage regions. As both materials have been tested under the same conditions, it can safely be assumed that the spherical morphology is responsible for the increase in cyclability, probably due to better accommodation of volume changes, better contact with the conductive carbon, and shortened sodium ion diffusion pathways. Even for higher current rates, spherical NMO shows remarkable cycle stability so that, for example, after 100 cycles, 84 mA h g^{-1} can still be achieved for 200 mA g^{-1}.

Therefore, we have proven that a change in morphology towards spheres does not only work for LIB systems but also for sodium ion batteries. Moreover, we have demonstrated that spherical, P2-type NMO is a suitable sodium ion battery cathode material for applications that require high capacities and cycle stability.

■ ASSOCIATED CONTENT

Ⓢ Supporting Information

Figure S1 shows the (ex-situ) XRD of the flake-like and spherical NMO after cycling, indicating that the main structure is largely maintained and small transformations occur for both materials. The impurity peak at $2\theta = 13$ can be attributed to the birnessite structure, which was probably formed while handling the sample in atmosphere. Figure S2 shows SEM images of the flake-like NMO after cycling to substantiate the claim that the particles that can be seen in Fig. 1h are indeed NMO. This material is available free of charge via the Internet at http://pubs.acs.org/.

■ AUTHOR INFORMATION

Corresponding Author

*Email: Madhavi@ntu.edu.sg.

Author Contributions

∥The manuscript was written through contributions of all authors. All authors have given approval to the final version of the manuscript. N.B. and S.H. contributed equally to this manuscript.

Funding

This work was financially supported by the Singapore National Research Foundation under its Campus for Research Excellence and Technological Enterprise (CREATE) programme.

Notes

The authors declare no competing financial interest.

■ ACKNOWLEDGMENTS

Y.L.C. acknowledges the World Future Foundation for their support.

■ REFERENCES

(1) Mp, X. *Springer Materials* (www.springermaterials.com) Landolt-Boernstein Databaset-Boernstein Database; Springer: New York; pp 248−250, 1984.

(2) Ellis, B. L.; Nazar, L. F. Sodium and Sodium-Ion Energy Storage Batteries. *Curr. Opin. Solid State Mater. Sci.* **2012**, *16*, 168−177.

(3) Palomares, V.; Serras, P.; Villaluenga, I.; Hueso, K. B.; Carretero-González, J.; Rojo, T. Na-Ion Batteries, Recent Advances and Present Challenges to Become Low Cost Energy Storage Systems. *Energy Environ. Sci.* **2012**, *5*, 5884−5901.

(4) Palomares, V.; Casas-Cabanas, M.; Castillo-Martínez, E.; Han, M. H.; Rojo, T. Update on Na-Based Battery Materials. A Growing Research Path. *Energy Environ. Sci.* **2013**, *6*, 2312−2337.

(5) Kim, S.-W.; Seo, D.-H.; Ma, X.; Ceder, G.; Kang, K. Electrode Materials for Rechargeable Sodium-Ion Batteries: Potential Alternatives to Current Lithium-Ion Batteries. *Adv. Energy Mater.* **2012**, *2*, 710−721.
(6) Chevrier, V. L.; Ceder, G. Challenges for Na-Ion Negative Electrodes. *J. Electrochem. Soc.* **2011**, *158*, A1011−A1014.
(7) Pan, H.; Hu, Y.-S.; Chen, L. Room-Temperature Stationary Sodium-Ion Batteries for Large-Scale Electric Energy Storage. *Energy Environ. Sci.* **2013**, *6*, 2338−2360.
(8) Komaba, S.; Murata, W.; Ishikawa, T.; Yabuuchi, N.; Ozeki, T.; Nakayama, T.; Ogata, A.; Gotoh, K.; Fujiwara, K. Electrochemical Na Insertion and Solid Electrolyte Interphase for Hard-Carbon Electrodes and Application to Na-Ion Batteries. *Adv. Funct. Mater.* **2011**, *21*, 3859−3867.
(9) Komaba, S.; Ishikawa, T.; Yabuuchi, N.; Murata, W.; Ito, A.; Ohsawa, Y. Fluorinated Ethylene Carbonate as Electrolyte Additive for Rechargeable Na Batteries. *ACS Appl. Mater. Interfaces* **2011**, *3*, 4165−4168.
(10) Yabuuchi, N.; Kajiyama, M.; Iwatate, J.; Nishikawa, H.; Hitomi, S.; Okuyama, R.; Usui, R.; Yamada, Y.; Komaba, S. P2-Type $Na_x[Fe_{1/2}Mn_{1/2}]O_2$ Made from Earth-Abundant Elements for Rechargeable Na Batteries. *Nat. Mater.* **2012**, *11*, 512−517.
(11) Oh, S.-M.; Myung, S.-T.; Hassoun, J.; Scrosati, B.; Sun, Y.-K. Reversible $NaFePO_4$ Electrode for Sodium Secondary Batteries. *Electrochem. Commun.* **2012**, *22*, 149−152.
(12) Liu, H.; Zhou, H.; Chen, L.; Tang, Z.; Yang, W. Electrochemical Insertion/Deinsertion of Sodium on NaV_6O_{15} Nanorods as Cathode Material of Rechargeable Sodium-Based Batteries. *J. Power Sources* **2011**, *196*, 814−819.
(13) Novak, P.; Scheifele, W.; Haas, O. Magnesium Insertion Batteries - an Alternative to Lithium? *J. Power Sources* **1995**, *54*, 479−482.
(14) West, K.; Zachau-Christiansen, B.; Jacobsen, T.; Jacobsen, T. Sodium Insertion in Vanadium Oxides. *Solid State Ionics* **1988**, *28-30*, 1128−1131.
(15) Wang, G.; Pistoia, G. Rechargeable All Solid-State Lithium and Sodium Cells with Composite Cathodic Films Based on $Na_{1+x}V_3O_8$. *J. Electroanal. Chem.* **1991**, *302*, 275−278.
(16) He, H.; Jin, G.; Wang, H.-Y.; Huang, X.; Chen, Z.; Sun, D.; Tang, Y.-G. Annealed NaV_3O_8 Nanowires with Good Cycling Stability as a Novel Cathode for Na-Ion Battery. *J. Mater. Chem. A* **2013**, *2*, 3563−3570.
(17) Hartung, S.; Bucher, N.; Nair, V. S.; Ling, C. Y.; Wang, Y.; Hoster, H. E.; Srinivasan, M. Sodium Vanadium Oxide − a New Material for High-Performance Symmetric Sodium Ion Batteries. *Chem. Phys. Chem.* **2014**, 10.1002/cphc.201402020R1.
(18) Jian, Z.; Han, W.; Lu, X.; Yang, H.; Hu, Y.-S.; Zhou, J.; Zhou, Z.; Li, J.; Chen, W.; Chen, D.; Chen, L. Superior Electrochemical Performance and Storage Mechanism of $Na_3V_2(PO_4)_3$ Cathode for Room-Temperature Sodium-Ion Batteries. *Adv. Energy Mater.* **2013**, *3*, 156−160.
(19) Xu, M.; Wang, L.; Zhao, X.; Song, J.; Xie, H.; Lu, Y.; Goodenough, J. B. $Na_3V_2O_2(PO_4)_2F$/Graphene Sandwich Structure for High-Performance Cathode of a Sodium-Ion Battery. *Phys. Chem. Chem. Phys.* **2013**, *15*, 13032−13037.
(20) Berthelot, R.; Carlier, D.; Delmas, C. Electrochemical Investigation of the P2−Na_xCoO_2 Phase Diagram. *Nat. Mater.* **2011**, *10*, 74−80.
(21) Bhide, A.; Hariharan, K. Physicochemical Properties of Na_xCoO_2 as a Cathode for Solid State Sodium Battery. *Solid State Ionics* **2011**, *192*, 360−363.
(22) Braconnier, J. J.; Delmas, C.; Hagenmuller, P. Etude par Desintercalation Electrochimique des Systemes Na_xCrO_2 et Na_xNiO_2. *Mater. Res. Bull.* **1982**, *17*, 993−1000.
(23) D'Arienzo, M.; Ruffo, R.; Scotti, R.; Morazzoni, F.; Mari, C. M.; Polizzi, S. Layered $Na_{0.71}CoO_2$: A Powerful Candidate for Viable and High Performance Na-Batteries. *Phys. Chem. Chem. Phys.* **2012**, *14*, 5945−5952.
(24) Ding, J. J.; Zhou, Y. N.; Sun, Q.; Yu, X. Q.; Yang, X. Q.; Fu, Z. W. Electrochemical Properties of P2-phase $Na_{0.74}CoO_2$ Compounds as Cathode Material for Rechargeable Sodium-Ion Batteries. *Electrochim. Acta* **2013**, *87*, 388−393.
(25) Guignard, M.; Didier, C.; Darriet, J.; Bordet, P.; Elkaïm, E.; Delmas, C. P2-Na_xVO_2 System as Electrodes for Batteries and Electron-Correlated Materials. *Nat. Mater.* **2012**, *11*, 1−7.
(26) Meng, Y. S.; Hinuma, Y.; Ceder, G. An Investigation of the Sodium Patterning in Na_xCoO_2 ($0.5 < \text{or} = x < \text{or} = 1$) by Density Functional Theory Methods. *J. Chem. Phys.* **2008**, *128*, 104708-1−104708-8.
(27) Shu, G.; Prodi, A.; Chu, S.; Lee, Y.; Sheu, H.; Chou, F. Searching for Stable Na-Ordered Phases in Single-Crystal Samples of γ-Na_xCoO_2. *Phys. Rev. B* **2007**, *76*, 184115-1−184115-9.
(28) Takahashi, Y.; Akimoto, J.; Kijima, N.; Gotoh, Y. Structure and Electron Density Analysis of $Na_{0.74}CoO_2$ by Single-Crystal X-ray Diffraction. *Solid State Ionics* **2004**, *172*, 505−508.
(29) Xia, X.; Dahn, J. R. A Study of the Reactivity of De-Intercalated P2-Na_xCoO_2 with Nonaqueous Solvent and Electrolyte by Accelerating Rate Calorimetry. *J. Electrochem. Soc.* **2012**, *159*, A647−A650.
(30) Zandbergen, H.; Foo, M.; Xu, Q.; Kumar, V.; Cava, R. Sodium Ion Ordering in Na_xCoO_2: Electron Diffraction Study. *Phys. Rev. B* **2004**, *70*, 024101-1−024101-8.
(31) Zhang, P.; Capaz, R.; Cohen, M.; Louie, S. Theory of Sodium Ordering in Na_xCoO_2. *Phys. Rev. B: Condens. Matter* **2005**, *71*, 153102-1−153102-4.
(32) Vassilaras, P.; Toumar, A. J.; Ceder, G. Electrochemical Properties of $NaNi_{1/3}Co_{1/3}Fe_{1/3}O_2$ as a Cathode Material for Na-Ion Batteries. *Electrochem. Commun.* **2014**, *38*, 79−81.
(33) Wang, Y.; Yu, X.; Xu, S.; Bai, J.; Xiao, R.; Hu, Y.-S.; Li, H.; Yang, X.-Q.; Chen, L.; Huang, X. A Zero-Strain Layered Metal Oxide as the Negative Electrode for Long-Life Sodium-Ion Batteries. *Nat. Commun.* **2013**, *4*, 2365.
(34) Wu, F.; Yu, G.; Xu, D.; Kan, E. First-Principles Investigations on the Magnetic Structure of α-$NaMnO_2$. *J. Phys.: Condens. Matter* **2012**, *24*, 456002-1−456002-5.
(35) Caballero, A.; Hernán, L.; Morales, J.; Sánchez, L.; Santos, J. Ion-Exchange Properties of P2-Na_xMnO_2: Evidence of the Retention of the Layer Structure Based on Chemical Reactivity Data and Electrochemical Measurements of Lithium Cells. *J. Solid State Chem.* **2003**, *174*, 365−371.
(36) Ma, X.; Chen, H.; Ceder, G. Electrochemical Properties of Monoclinic $NaMnO_2$. *J. Electrochem. Soc.* **2011**, *158*, A1307−A1312.
(37) Bucher, N.; Hartung, S.; Gocheva, I.; Cheah, Y. L.; Srinivasan, M.; Hoster, H. E. Combustion-Synthesized Sodium Manganese (Cobalt) Oxides as Cathodes for Sodium Ion Batteries. *J. Solid State Electrochem.* **2013**, *17*, 1923−1929.
(38) Kim, D.; Lee, E.; Slater, M.; Lu, W.; Rood, S.; Johnson, C. S. Layered $Na[Ni_{1/3}Fe_{1/3}Mn_{1/3}]O_2$ Cathodes for Na-Ion Battery Application. *Electrochem. Commun.* **2012**, *18*, 66−69.
(39) Carlier, D.; Cheng, J. H.; Berthelot, R.; Guignard, M.; Yoncheva, M.; Stoyanova, R.; Hwang, B. J.; Delmas, C. The P2-$Na_{2/3}Co_{2/3}Mn_{1/3}O_2$ Phase: Structure, Physical Properties and Electrochemical Behavior as Positive Electrode in Sodium Battery. *Dalton Trans.* **2011**, *40*, 9306−9312.
(40) Zhou, L.; Zhao, D.; Lou, X. $LiNi_{0.5}Mn_{1.5}O_4$ Hollow Structures as High-Performance Cathodes for Lithium-Ion Batteries. *Angew. Chem., Int. Ed. Engl.* **2012**, *51*, 239−241.
(41) Zhou, L.; Zhou, X.; Huang, X.; Liu, Z.; Zhao, D.; Yao, X.; Yu, C. Designed Synthesis of $LiMn_2O_4$ Microspheres with Adjustable Hollow Structures for Lithium-Ion Battery Applications. *J. Mater. Chem. A* **2013**, *1*, 837−842.
(42) Xiao, L.; Guo, Y.; Qu, D.; Deng, B.; Liu, H.; Tang, D. Influence of Particle Sizes and Morphologies on the Electrochemical Performances of Spinel $LiMn_2O_4$ Cathode Materials. *J. Power Sources* **2013**, *225*, 286−292.
(43) Chen, X.-F.; Qie, L.; Zhang, L.-L.; Zhang, W.-X.; Huang, Y.-H. Self-Templated Synthesis of Hollow Porous Submicron $ZnMn_2O_4$

Sphere as Anode for Lithium-Ion Batteries. *J. Alloys Compd.* **2013**, *559*, 5−10.
(44) Fei, J. B.; Cui, Y.; Yan, X. H.; Qi, W.; Yang, Y.; Wang, K. W.; He, Q.; Li, J. B. Controlled Preparation of MnO_2 Hierarchical Hollow Nanostructures and Their Application in Water Treatment. *Adv. Mater.* **2008**, *20*, 452−456.
(45) Parant, J.-P.; Olazcuaga, R.; Devalette, M.; Fouassier, C.; Hagenmuller, P. Sur Quelques Nouvelles Phases de Formule Na_xMnO_2 ($x < 1$). *J. Solid State Chem.* **1971**, *3*, 1−11.
(46) Patoux, S.; Dollé, M.; Doeff, M. M. Layered Manganese Oxide Intergrowth Electrodes for Rechargeable Lithium Batteries. 2. Substitution with Al. *Chem. Mater.* **2005**, *17*, 1044−1054.
(47) Ponrouch, A.; Marchante, E.; Courty, M.; Tarascon, J.-M.; Palacín, M. R. In Search of an Optimized Electrolyte for Na-Ion Batteries. *Energy Environ. Sci.* **2012**, *5*, 8572−8583.
(48) Ponrouch, A.; Dedryvère, R.; Monti, D.; Demet, A. E.; Ateba Mba, J. M.; Croguennec, L.; Masquelier, C.; Johansson, P.; Palacín, M. R. Towards High Energy Density Sodium Ion Batteries through Electrolyte Optimization. *Energy Environ. Sci.* **2013**, *6*, 2361−2369.
(49) Vidal-Abarca, C.; Lavela, P.; Tirado, J. L.; Chadwick, a. V.; Alfredsson, M.; Kelder, E. Improving the Cyclability of Sodium-Ion Cathodes by Selection of Electrolyte Solvent. *J. Power Sources* **2012**, *197*, 314−318.

Layered Na_xMnO_{2+z} in sodium ion batteries – influence of morphology on cycle performance

Nicolas Bucher[‡,a, b], *Steffen Hartung*[‡,a,b], *Arun Nagasubramanian*[a, c], *Yan Ling Cheah*[c], *Harry E. Hoster*[a,b], *Srinivasan Madhavi**[a,c]

a) TUM CREATE, Singapore 138602, Singapore

* E-mail: Madhavi@ntu.edu.sg

b) Technische Universität München, 85748 Garching, Germany

c) School of Materials Science and Engineering, Nanyang Technological University, Singapore 639798, Singapore

‡ *Nicolas Bucher and Steffen Hartung contributed equally to this manuscript.*

- Supporting information -

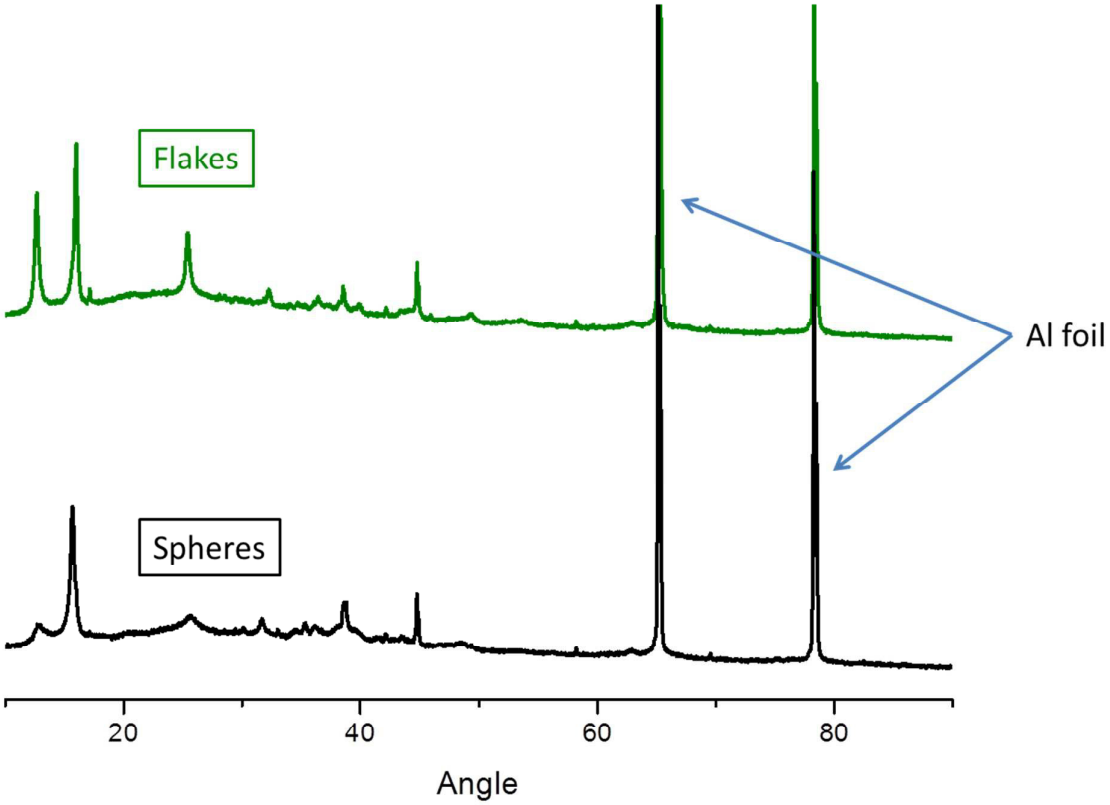

Figure S1: XRD of flake-like and spherical NMO after cycling

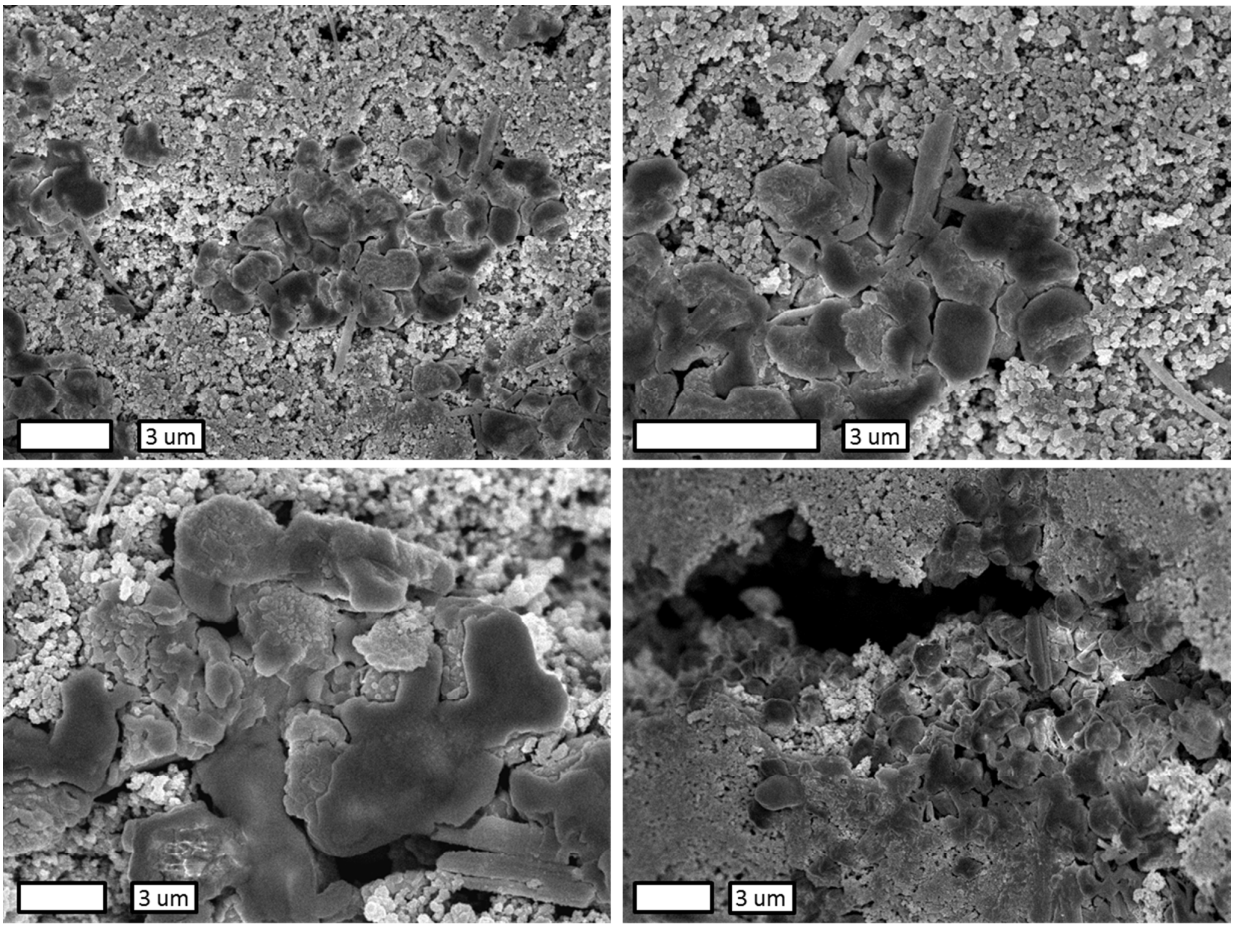

Figure S2: SEM images of flake-like NMO after cycling

4.3 Electrochemical Cell for *in operando* X-ray Diffraction Measurements on a Conventional X-ray Diffractometer

This chapter is a summary of the note "Electrochemical cell for *in operando* X-ray diffraction measurements on a conventional X-ray diffractometer" (Review of Scientific Instruments **2014**, *86*, 086102-1 – 3). The cell was the first *in operando* tool developed for a lab scale XRD in Singapore and is being utilised now for a variety of measurements on LIBs and NIBs. This work was jointly performed by S. Hartung and N Bucher. S. Hartung focussed on the verification and testing of the cell and drafted the manuscript. N. Bucher focussed on the development and construction of the cell.

As noted before, structural developments of the aforementioned electrode materials during cycling can be a crucial factor for observed electrochemical phenomena, such as differences in capacity or cycling stability. The method of choice for monitoring structural changes as a consequence of Na^+-(de-)insertion into / from a crystal structure is X-ray diffraction. As these processes are incremental, a continuous screening of structural developments is favoured over probing several samples at various states of charge. Not only does this provide a more complete picture, but it also eliminates comparability and reproducibility problems that typically arise for *ex situ* measurements for which different cells have to be used. Thus, electrochemical *in operando* measurements of battery materials possess an inherent advantage in determining structural changes.

Therefore, an electrochemical *in operando* XRD cell, which can be employed for measurements at laboratory scale diffractometers, was developed. Typically the incorporation of an X-ray window will keep the cell airtight to prevent reactions with the materials (*e.g.* alkali metal), is rather X-ray transmissible and also acts as current collector. However, the X-ray window causes reflections that can overlap with reflections from the material, and still absorbs X-rays which reduces signal intensity. Therefore, in most constructions the toxic and carcinogenic beryllium is used as it has a very low X-ray absorbents coefficient and only a few interfering reflections. In the construction presented here, the two functionalities for the current collector and the X-ray window are separated. This has two effects:

1) Currents during the measurement are not dissipated via the X-ray window, which reduces corrosion and thus extends the life-time of the window and potential duration of measurements
2) Requirements in term of mechanical stability are reduced for the X-ray window, as the pressure when closing the cell / in operation is accommodated by the current collector.

The *in operando* cell was constructed to account for these factors (Chapter 4.3, Figure. 1 of the publication). Moreover, the spacer supporting the alkali metal anode was constructed in a 'flower' shape, so that lateral movement is inhibited, and excess electrolyte can leave the inner part of the cell when closing it, which further reduces stability requirements for the X-ray window. As a consequence, ultrathin Al foil with a thickness of 6 µm can be used as X-ray window. Thus, X-ray absorption is reduced and the toxic beryllium can be avoided. Moreover, in contrast to the often used mechanically more stable Kapton, Al gives only few, defined reflections, which reduces overlap with material reflections and thus facilitates the analysis. First *in operando* measurements over a duration of 100 hours confirmed the operability of the cell for $Na_{2.55}V_6O_{16}$ as a cathode material for NIB. Particularly for Na_xMnO_2, excellent signal quality and signal to noise ratio has been demonstrated.

In summary, a new *in operando* X-ray diffraction cell was constructed which can be employed on a common lab diffractometer. Excellent diffraction data can be obtained by the use of non-toxic and cheap materials.

In addition to the data presented in this publication, operando measurements of NMO flakes were conducted (presented in Chapter 4.1). Although a phase chance is indicated (Figure 14), the identification was not clear, which was attributed either to insufficient resolution of the laboratory diffractometer, or to the fact that these measurements are done in reflection mode, which means that the bulk materials was not probed. Therefore, the need for transmission measurements with higher resolution was identified; this is discussed in the next Chapter 4.4.

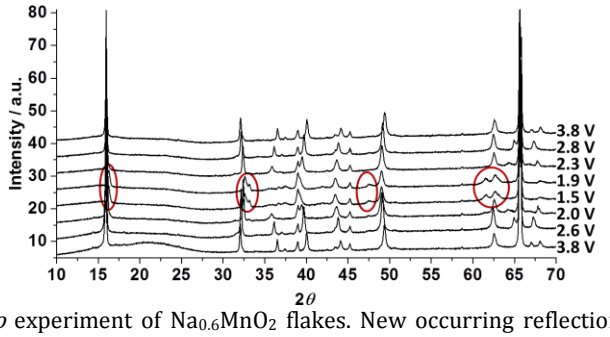

Figure 14. *In operando* experiment of $Na_{0.6}MnO_2$ flakes. New occurring reflections are indicated in red.

Note: Electrochemical cell for in operando X-ray diffraction measurements on a conventional X-ray diffractometer

Steffen Hartung, Nicolas Bucher, Ramona Bucher, and Madhavi Srinivasan

The publication can be found under the following weblink:

http://dx.doi.org/10.1063/1.4926465

Note: Electrochemical cell for *in operando* X-ray diffraction measurements on a conventional X-ray diffractometer

Steffen Hartung,[1,2,3,a)] Nicolas Bucher,[1,2,3,a)] Ramona Bucher,[1] and Madhavi Srinivasan[1,3]
[1]*TUM CREATE, Singapore 138602, Singapore*
[2]*Technical University of Munich, Garching 85748, Germany*
[3]*School of Materials Science and Engineering, Nanyang Technological University, Singapore 639798, Singapore*

(Received 29 April 2015; accepted 28 June 2015; published online 10 August 2015)

Electrochemical *in operando* X-ray diffraction (XRD) is a powerful method to analyze structural changes of energy storage materials while inserting/de-inserting charge carriers, such as Li- or Na-ions, into/from a host structure. The design of an XRD *in operando* cell is presented, which enables the use of thin (6 μm) aluminum foil as X-ray window as a non-toxic alternative to conventional beryllium windows. Owing to the reduced thickness, diffraction patterns and their changes during cycling can be observed with excellent quality, which was demonstrated for two cathode materials for sodium-ion batteries in a half-cell set-up, P2-$Na_{0.7}MnO_2$ and $Na_{2.55}V_6O_{16}{\cdot}0.6H_2O$. © *2015 AIP Publishing LLC*. [http://dx.doi.org/10.1063/1.4926465]

As electrochemical energy storage devices are being intensely researched for a variety of applications, approaches to optimize their performance are of high commercial interest. The underlying mechanism of energy storage for many systems is the intercalation of ions, e.g., Li^+ and Na^+, into a given crystal structure.[1–3] Thus, elucidating potential structural changes during (de-)insertion might go a long way in explaining observed electrochemical phenomena like capacity fading, and therefore deliver important information for better energy storage devices. Consequently, experimental setups have been developed to study these changes *in operando*.[4–6] For the observation of crystal structure changes, the method of choice is X-ray diffraction.

For electrochemical *in operando* XRD measurements, a setup needs to fulfill several requirements. An airtight system is crucial to prevent a reaction of air with the components of the electrochemical cell, particularly for half-cell setups that contain metallic lithium or sodium. The window, shielding the electrochemically active components from the outer atmosphere, should be as thin as possible and needs to have a low X-ray absorption coefficient to minimize X-ray absorption, and thus a decrease in signal intensity. Ideally, of course, non-toxic materials are preferred.

Even though commercial cell setups are available, they have some shortcomings. In a typical setup, the active material, which is to be measured during cycling in a half-cell setup with lithium or sodium as the negative electrode, is pressed onto the X-ray window. This is typically aluminum-coated beryllium, which serves both as current collector and as X-ray window due to its low X-ray absorption coefficient. Moreover, as the active material is mechanically pressed against the X-ray window, mechanical stability is desired to prevent fissures in the window. This can be achieved by using a rigid beryllium window with a typical thickness of around 125 μm. The main drawbacks of beryllium, however, are its toxicity and high cost. Furthermore, dissipating the current via the beryllium as it is the case in this setup makes the window more susceptible to electrochemically induced corrosion, as beryllium dissolves at voltages above 3 V.[7] After early studies by Chianelli *et al.* in 1978,[8] several approaches to tailor *in operando* XRD cells to specific needs have been proposed.[5,7,9–12]

This work presents a new cell setup developed by our group to address the obstacles for *in operando* diffraction measurements mentioned above. In this cell, the X-ray window and current collector are separated by a gap (see Figure 1 (8)). This setup has two main advantages. First, as the current is no longer dissipated via the X-ray window, corrosion is decreased and lifetime of the window, and thus possible *in operando* measurement time, can be extended. Second, mechanical pressure during cell assembly and subsequent cycling is no longer exerted on the X-ray window, but on the current collector. Thus, requirements in terms of mechanical stability can be greatly reduced for the X-ray window. As a consequence, beryllium can be replaced by the cheaper, non-toxic aluminum. Moreover, the thickness of the X-ray window can be reduced, so that X-ray reflection of the window material is minimized, and signal quality of the battery material is enhanced.

For the approach presented here, an aluminum foil with a thickness of 6 μm was used. The active material, together with teflonized acetylene black as binder, and activated carbon as conducting agent, was pressed into a stainless steel grid, which acted as the current collector (component (7) in Figure 1). After mounting the window (i.e., assembling parts (1)–(5)), the cell is turned around so that the inner part faces upward, and component (7) is placed onto (5), and then held in place by (13). A separator and lithium/sodium disc are placed onto (7), followed by a stainless steel spacer (12) in a floral shape—the outer edges touch the walls (component (13)), which inhibits lateral movement and prevents the electrodes from slipping out of position. The indentations ensure that the electrolyte, which is added after (12) is in place, can penetrate past the spacer and

[a)]S. Hartung and N. Bucher contributed equally to this work.

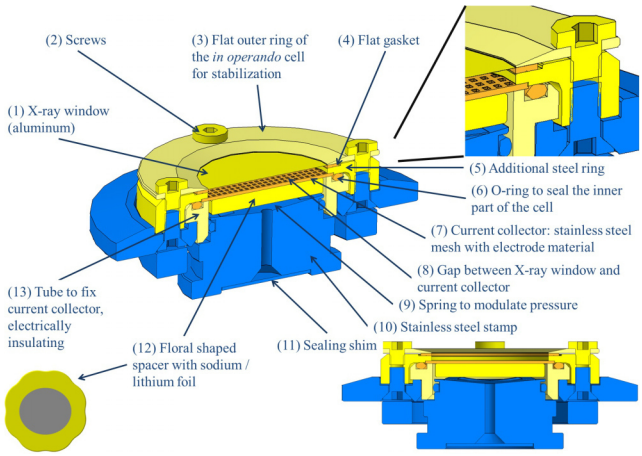

FIG. 1. Setup of the new *in operando* cell.

soak the separator and active material. These components are pressed together when closing the cell. Excess electrolyte can "leave" the inner part of the cell due to the indentations, which avoids pressure on the aluminum foil. Moreover, due to the steel ring (5), onto which the current collector is pressed, this pressure is accommodated without effect for the aluminum foil. For the lower part (blue (color code refers to online version) components in Figure 1), a setup rebuilt from a conventional commercial setup was used.[13] X-ray diffraction is measured in reflection mode from above, as the active material to be measured is exposed to X-rays due to the use of a stainless steel mesh. As the active material is slightly below the X-ray window, the outer stainless steel ring (3) needs to be flat to avoid reflection of incoming X-rays by the ring at small angles.

This *in operando* cell setup has been tested for various materials on a conventional Rigaku SmartLab X-ray diffractometer (200 mA, 45 kV) in reflection mode, with copper as X-ray source. One example is P2-$Na_{0.7}MnO_2$ (NMO), a promising material for sodium-ion batteries.[14,15] Figure 2 shows the X-ray diffraction patterns of NMO in powder form, and of a pellet, which was prepared in the way described above and built into the *in operando* XRD cell; the pattern of the aluminum used as X-ray window is added as reference. As can be seen, the pattern is well visible. The high signal intensity and excellent signal-to-noise ratio allow the monitoring of shifts of the observed reflections, or phase transformations, during cycling. The X-ray window does not reduce signal intensity detrimentally, and the well-defined reflections of the aluminum only hinder analysis in the rare case when a material has reflections in the same narrow angle range.

A good example for the easily observable shifts of the observed reflections is $Na_{2.55}V_6O_{16}{\cdot}0.6H_2O$,[16] which was cycled vs. Na in the presented setup with 1M $NaClO_4$ (Sigma Aldrich, >98%) in ethylene carbonate: propylene carbonate (1:1 % wt) as the electrolyte (PC: Sigma Aldrich, 99.7%, EC: Sigma Aldrich, 99%).

Figure 3(a) shows the XRD pattern of a $Na_{2.55}V_6O_{16}{\cdot}0.6H_2O$ pellet in the *in operando* cell. Figure 3(b) shows reversible shifts during electrochemical cycling for selected reflections in the range of $2\theta = 26.5°–31°$, which comprises reflections of diverse intensities. The color code represents the height profile, with blue (color code refers to online version) being the "noise," i.e., only background reflection.

As can be seen, reversible shifts of the observed reflections are clearly observable, which can give new insights into changes of the lattice parameters, and thus enhance the understanding of the expanding and shrinking unit cell

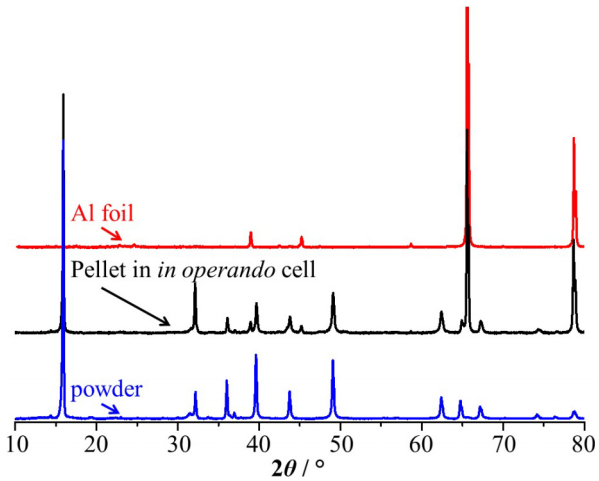

FIG. 2. X-ray diffraction pattern of P2-$Na_{0.7}MnO_2$ powder (bottom), a pellet with P2-$Na_{0.7}MnO_2$, teflonized acetylene black, and activated carbon (8:1:1 weight) on a stainless steel grid in the *in operando* cell (middle), the aluminum window (top).

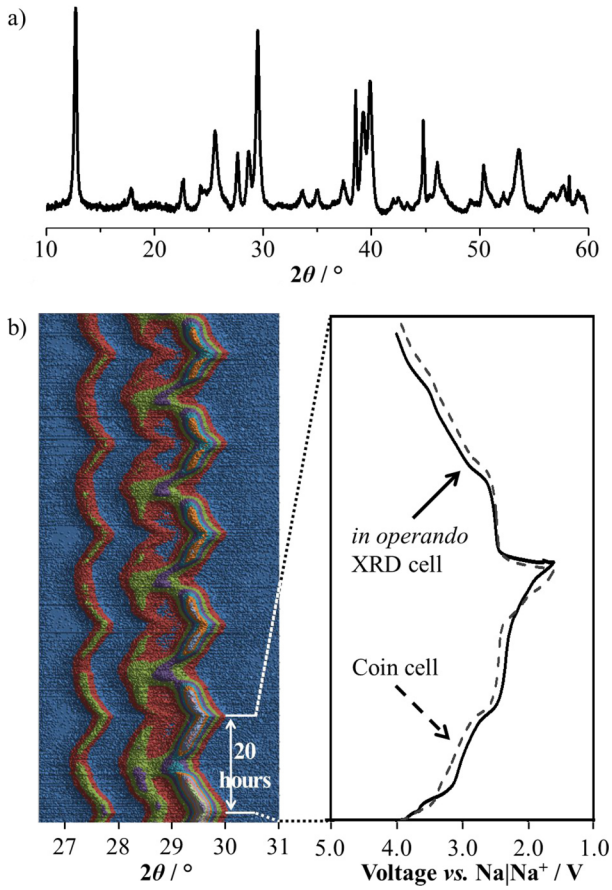

FIG. 3. (a) XRD pattern of $Na_{2.55}V_6O_{16}{\cdot}0.6H_2O$ in the *in operando* cell; (b) *in operando* XRD measurement for 5 cycles at 10 mA g^{-1}; left: reversible shifts of the observed reflections, right: representative charge/discharge curve in the *in operando* cell (solid line) and in a coin cell (dashed line).

during Na-ion insertion and de-insertion. This can be nicely correlated to the electrochemical charge/discharge data as presented on the right side of Figure 3(b), which also corresponds well with similar measurements in an established coin cell setup (solid line: *in operando* cell, dashed line: coin cell). Quantitative analyses to study this from a scientific, not instrument-focused point of view will be concluded shortly.

In summary, we have designed, constructed, and verified a new setup for electrochemical *in operando* X-ray diffraction measurements using a conventional X-ray diffractometer. The setup is based on a separation of X-ray window and current collector, which enables the use of non-toxic and cheap ultrathin aluminum foil, and thus ensures excellent signal quality. This facilitates the examination of structural changes while electrochemically inserting/deinserting Li- and Na-ions into/from a host material. Consequently, a deeper understanding for structural processes during charging/discharging battery materials can be obtained. These insights can be used to develop strategies to mitigate capacity fading in energy storage materials.

This work was financially supported by the Singapore National Research Foundation under its Campus for Research Excellence and Technological Enterprise (CREATE) programme. The authors thank Steffen Schlueter and Patrick Osswald for initial discussions.

[1]D. Kundu, E. Talaie, V. Duffort, and L. F. Nazar, Angew. Chem., Int. Ed. **54**, 3431 (2015).
[2]N. Yabuuchi, K. Kubota, M. Dahbi, and S. Komaba, Chem. Rev. **114**, 11636 (2014).
[3]L. Croguennec and M. R. Palacin, J. Am. Chem. Soc. **137**, 3140 (2015).
[4]J. N. Weker and M. F. Toney, Adv. Funct. Mater. **25**, 1622 (2015).
[5]Y. Shen, E. E. Pedersen, M. Christensen, and B. B. Iversen, Rev. Sci. Instrum. **85**, 104103 (2014).
[6]C. J. Pelliccione, E. V. Timofeeva, J. P. Katsoudas, and C. U. Segre, Rev. Sci. Instrum. **85**, 126108 (2014).
[7]M. N. Richard, I. Koetschau, and J. R. Dahn, J. Electrochem. Soc. **144**, 554 (1997).
[8]R. R. Chianelli, J. C. Scanlon, and B. M. L. Rao, J. Electrochem. Soc. **125**, 1563 (1978).
[9]M. Morcrette, Y. Chabre, G. Vaughan, G. Amatucci, J. Leriche, S. Patoux, C. Masquelier, and J.-M. Tarascon, Electrochim. Acta **47**, 3137 (2002).
[10]N. A. Cañas, S. Wolf, N. Wagner, and K. A. J. Friedrich, J. Power Sources **226**, 313 (2013).
[11]G. A. Roberts and K. D. Stewart, Rev. Sci. Instrum. **75**, 1251 (2004).
[12]K. Rhodes, M. Kirkham, R. Meisner, C. M. Parish, N. Dudney, and C. Daniel, Rev. Sci. Instrum. **82**, 075107 (2011).
[13]Rigaku, Rigaku J. **27**, 32 (2011).
[14]N. Bucher, S. Hartung, I. Gocheva, Y. L. Cheah, M. Srinivasan, and H. E. Hoster, J. Solid State Electrochem. **17**, 1923 (2013).
[15]N. Bucher, S. Hartung, A. Nagasubramanian, Y. L. Cheah, H. E. Hoster, and S. Madhavi, ACS Appl. Mater. Interfaces **6**, 8059 (2014).
[16]S. Hartung, N. Bucher, V. S. Nair, C. Y. Ling, Y. Wang, H. E. Hoster, and M. Srinivasan, Chemphyschem **15**, 2121 (2014).

4.4 P2-$Na_xCo_yMn_{1-y}O_2$ (y = 0, 0.1) as Cathode Materials in Sodium-Ion Batteries – Investigation of Doping and Morphology to Enhance Cycling Stability

This chapter is a summary of the manuscript entitled "P2-$Na_xCo_yMn_{1-y}O_2$ (y = 0, 0.1) as Cathode Materials in Sodium-Ion Batteries – Investigation of Doping and Morphology to Enhance Cycling Stability" (*submitted to ACS Chemistry of Materials*). It is mainly based on synchrotron measurements that were performed at the Stanford Linear Accelerator Center (SLAC) and aims at obtaining a better understanding of the causes for different cycling stabilities. N. Bucher was leading the work that is presented in this publication.

As indicated in previous chapters, structural processes that occur during Na^+-(de-)insertion play a crucial role for capacity and cycling stability. Therefore, electrochemical *in operando* synchrotron XRD was employed to investigate similarities and differences regarding structural processes during cycling between the isostructural Na_xMnO_{2+z} (NMO) flakes, $Na_xCo_{0.1}MnO_{2+z}$ (NCO) flakes, and Na_xMnO_{2+z} spheres. Ultimately, the two routes to optimise cycling stability, Co-doping (Chapter 4.1) and morphology optimisation (Chapter 4.2), are combined. It is shown that $Na_xCo_{0.1}MnO_{2+z}$ spheres are superior, with regard to capacity and cycling stability, to the aforementioned materials. Thus, cycling stability increases in the following order: NMO flakes < NCO flakes < NMO spheres < NCO spheres.

At first it was ruled out that manganese dissolution (a widely discussed phenomena for Mn-materials[130,131]) could be a reason for the capacity loss. Structural investigations have revealed that during discharge, *i.e.* Na^+-insertion, NMO flakes undergo a partial phase transition. The initial hexagonal phase transforms into a new orthorhombic phase (so-called P'2-phase) with the *Cmcm* symmetry. The phase change is caused by a gliding of the layers of MnO_6-octahedra. Even though this phase transition is reversed during de-insertion of Na^+, capacity fading can be attributed to structural stress from repeated phase transitions during cycling.

The Co-doped analogue, NCO flakes, does not show this phase change. Hence, it is concluded that Co-doping has as stabilising effect on the structure during cycling and suppresses not only Na^+-ordering between the layers of MnO_6-octahedra, but also the

phase transition towards the P'2-phase. This is one possible explanation for the increase in cycling stability over the NMO flakes.

The same effect was also observed for the new presented NCO spheres in an *in operando* XRD experiment – the material maintains its hexagonal structure throughout cycling. As neither NCO flakes nor NCO spheres show phase changes during discharge, these two materials were taken as models to explain the difference in cycling stability between the flake-like and the spherical morphology. It has been found that volume change of the unit cell is significantly reduced as compared to the expansion of the unit cell for NCO flakes during Na^+-insertion. At the same time, comparison of the development of the full with at half maximum indicates that the strain is higher. Therefore, it is concluded that accommodation of Na^+ into the host structure by an increase in strain results in a less detrimental effect than an expansion of the unit cell. As similar differences in changes of the unit cell volume was found for the undoped analogues, the same explanation is assumed to be valid. This helps explain the superior cycling stability of the spherical morphology and a better accommodation of higher sodium content in the host structure.

These findings have been substantiated by GITT and EIS measurements. Not only are the changes in the diffusion coefficient for Na^+ in line with the phase changes observed from XRD. It was also confirm the Co-doping has a positive influence on Na-transport within the structure, which leads to a superior rate capability and can be another reason for the improved cycling stabilities of the Co-doped materials.

In summary, the main reasons for the success of these two strategies were identified. Cathode material with spherical morphology seems to accommodate cycling stresses better, and Co increases stability by supressing phase changes and sodium ordering, as well as improving Na^+-mobility within the active material. A combination of both approaches led to a superior material which exceeds most literature values (compare also Chapter 2.3.1).

P2-$Na_xCo_yMn_{1-y}O_2$ (y = 0, 0.1) as Cathode Materials in Sodium-Ion Batteries – Investigation of Doping and Morphology to Enhance Cycling Stability

Nicolas Bucher, Steffen Hartung, Joseph B. Franklin, Anna M. Wise, Linda Y. Lim, Han-Yi Chen, Johanna Nelson Weker, Michael F. Toney, Madhavi Srinivasan

Manuscript submitted to *ACS Chemistry of Materials*

Manuscript ID: cm-2015-04557v

After the review process, a revised version of this manuscript was accepted:

Nicolas Bucher, Steffen Hartung, Joseph B. Franklin, Anna M. Wise, Linda Y. Lim, Han-Yi Chen, Johanna Nelson Weker, Michael F. Toney, Srinivasan Madhavi: P2–$Na_xCo_yMn_{1-y}O_2$ (y = 0, 0.1) as Cathode Materials in Sodium-Ion Batteries – Effects of Doping and Morphology To Enhance Cycling Stability. Adapted with permission from ACS Chem. Mater. **2016**, DOI: 10.1021/acs.chemmater.5b04557, Copyright 2016 American Chemical Society.

The publication can be found under the following weblink:

http://dx.doi.org/10.1021/acs.chemmater.5b04557

P2-$Na_xCo_yMn_{1-y}O_2$ (y = 0, 0.1) as Cathode Materials in Sodium-Ion Batteries – Investigation of Doping and Morphology to Enhance Cycling Stability

Nicolas Bucher[‡1,2,3)], Steffen Hartung[‡1,2,3)], Joseph B. Franklin[4)], Anna M. Wise[5)], Linda Y. Lim[5,6)], Han-Yi Chen[1,2,3)], Johanna Nelson Weker[5)], Michael F. Toney[5)], Madhavi Srinivasan[1,3,4*]

[1] TUM CREATE, Singapore 138602, Singapore

[2] Technical University of Munich, Garching 85748, Germany

[3] School of Materials Science and Engineering, Nanyang Technological University, Singapore 639798, Singapore

[4] Energy Research Institute at NTU (ERI@N), Nanyang Technological University, Research Techno Plaza, 50 Nanyang Drive, Singapore

[5] Stanford Synchrotron Radiation Lightsource, SLAC National Accelerator Laboratory, 2575 Sand Hill Road, Menlo Park, CA, United States

[6] Department of Materials Science and Engineering, Stanford University, 496 Lomita Mall, Stanford, CA, United States.

KEYWORDS: sodium ion battery, sodium manganese oxide, in operando, synchrotron X-ray diffraction, cobalt doping, morphology, spheres

ABSTRACT: Sodium-ion batteries have become a subject of increasing interest and are considered as an alternative to the ubiquitous lithium-ion battery. However, capacities, and particularly cycling stability of electrodes need to be improved. One prominent material class is layered Na_xMO_{2+z} (M: transition metal), for which various strategies, such as morphology optimization and doping, have been previously presented by our group. In this work, structural processes as a consequence of Na^+ insertion into Na_xMnO_{2+x} flakes and spheres, as well as $Na_xCo_{0.1}Mn_{0.9}O_{2+z}$ flakes and spheres, have been investigated using *operando* synchrotron X-ray diffraction. The higher cycling stability of the Co-doped version is attributed to the suppression of transformation and ordering processes as compared to the pristine Na_xMnO_{2+z}. Moreover, galvanostatic intermittent titration technique measurements and electrochemical impedance spectroscopy indicate higher conductivity of Na-ions in the structure of the doped material. Increased cycling stability of spheres over flakes is attributed to smaller changes of the unit cell volume of the spheres and thus reduced structural stress. The combination of both strategies - morphology optimization and Co-doping - yield spherical $Na_xCo_{0.1}Mn_{0.9}O_{2+z}$ which exhibits superior performance as compared to flakes and undoped materials as well as most similar materials reported in literature.

INTRODUCTION

Sodium-ion batteries (NIBs) have received significant attention recently, and are considered a viable alternative to the ubiquitous lithium-ion batteries (LIBs).[1–5] NIBs have a cost advantage over LIBs for two main reasons. Na, unlike Li, does not alloy with Al in the anodic potential region. Thus, Cu, which is used as the anodic current collector in LIBs, can be replaced with the cheaper Al for NIBs.[6–8] Secondly, Na resources are more widespread and abundant than Li-based raw materials.[1,9] One of the most promising classes of cathode materials is layered oxides, Na_xMO_{2+z} (M = transition metal).[10,11] Within this class, there are several dominant subgroups, which are defined on the basis of the coordination of the Na-ions between the transition metal – oxygen layers. Following the nomenclature introduced by Delmas *et al.*,[12] in *O*-type materials, Na^+ is octahedrally coordinated by oxygen, whereas in *P*-type materials, the coordination is prismatic. Different stacking, *i.e.* shifts of the layers composed of edge-sharing MO_6-octahedra against one another, are indicated by numbers. In a P2-structure, *e.g.* two layers of MO_6-octahedra need to be depicted in the unit cell to accurately describe the structure. First studies on insertion processes into these layered oxides have been conducted in the 1980's.[12–17] Recently, particularly P2-type materials are of interest because of their good compromise regarding cycling stability and capacity.[18–26] In these studies, the predominant transition metal (typically Mn) was partially substituted by other metals. The variety in terms of composition is immense, and is the result of attempts to fine-tune certain characteristics such as cycling stability, oper-

ating potential, capacity, or cost. Thus, understanding the effect of those different transition metals on the structure changes is key to further develop and optimize P2-type layered oxides as cathodes for NIBs. Ni, for example, is employed due to its high redox potential, which elevates the average discharge potential, and thus energy density, of the material.[11,24,27] Co in Mn/Co-based layered oxide is reduced and oxidized in parallel to Mn over the course of cycling.[28] Increased cycling stability was obtained by incorporating Fe.[8,11] This Fe-doping suppresses minor structural transitions during cycling and concomitant Na^+ ordering processes and thus increases capacity retention. Mg both stabilizes the structure by suppressing a structural distortion towards an orthorhombic phase and a smoothening of the charge/discharge curves. However, this is achieved at the expense of capacity.[26,29,30] Moreover, several combinations of the aforementioned materials have been reported in an attempt to combine the respective advantages.[20,31,32] It was shown by our group before that substituting 11% of Mn with Co in the Na_xMnO_{2+z} structure suppresses Na^+ ordering and leads to an increase of cycling stability.[33] The underlying structural causes are the focus of this publication.

Another influencing factor for NIB performance is synthetic route. Synthesis conditions affect the amounts of defects in the structure,[31,34] the morphology, and long-range order. We found previously that spheres achieve higher capacity and a better cycling performance than flakes.[35] This prompted us to look into the structural aspects of this difference. In this work, the effect of Co-doping and morphology optimization are investigated using *operando* synchrotron X-ray diffraction (XRD), as well as galvanostatic intermittent titration technique (GITT) and electrochemical impedance spectroscopy (EIS). Manganese dissolution was shown to have a negligible effect on capacity fading using various analytical techniques. It is shown that for Na_xMnO_{2+z} (NMO) flakes a two phase region evolves during discharge. Substituting 10% of the Mn with Co suppresses both the Na^+ ordering processes and the transition to the orthorhombic phase. These effects are identified as possible causes for improved cycling performance. Moreover, it is shown that the enhanced conductivity adds to the positive influence of a small substitution of Mn with Co. Enhanced cycling performance of the spherical over the flake-like morphology is attributed to smaller changes of the volume of the unit cell for the spheres. Finally, both approaches were combined in the synthesis of spherical $Na_{0.6}Co_{0.1}Mn_{0.9}MnO_2$, which shows a significant improvement in cycling stability. Thus, the advantage of a variation of a previously investigated optimization strategy, doping, and a novel promising approach, spherical morphologies, were demonstrated.

EXPERIMENTAL SECTION

Synthesis and Coin Cell Preparation

Na_xMnO_{2+z} (NMO) and $Na_xCo_{0.1}Mn_{0.9}O_{2+z}$ (NCO) flakes were synthesized by combustion synthesis as described previously.[33,36–38] $NaNO_3$ (Sigma Aldrich, ≥ 99%) and $Mn(CH_3COO)_2$ (Alfa Aesar, anhydrous, 98 %) were mixed (molar ratio Na:Mn = 0.7) and subsequently dissolved in deionized water. For NCO, additional $Co(NO_3)_2$ was added, such that the weight ratio of Na:Co:Mn was 0.7:0.1:0.9. Concentrated HNO_3 (≥ 69%, Honeywell) was added, followed by 1.5 g of gelatine. The solution was heated until spontaneous combustion occurred. The resulting dark brownish powder was annealed at 800 °C for 4 hours, followed by another step at 610 °C for 9 hours and a quenching step to room temperature. Elemental composition, as determined by Inductively Coupled Plasma Optical Emission Spectrometry (ICP-OES), was $Na_{0.6}MnO_{2+z}$ for the NMO flakes and $Na_{0.6}Co_{0.1}Mn_{0.9}O_{2+z}$ for the NCO flakes, 'z' in the above-mentioned formula unit accounts for Mn-vacancies and is typically between 0.05 and 0.25 for this phase.[13]

Spherical NMO was synthesized as reported previously, with a slightly modified annealing procedure.[35] NH_4CO_3 was dissolved in deionized water, followed by a dropwise addition of ethanol (10% volume of the NH_4HCO_3 solution) and a solution of $MnSO_4$ in deionized water. To form spherical $MnCO_3$, the solution was stirred at room temperature. After filtration and subsequent washing, the product was annealed in air at 400 °C for 5 hours to form MnO_2. Then, it was dispersed in a solution of NaOH in deionized water and ethanol. Next, both water and ethanol were evaporated, and the residue was first annealed at 320 °C in air for 3 hours, followed by an annealing step in air at 800 °C for 4 hours, an additional step at 610 °C for 9 hours and finally by a quenching to room temperature. Chemical composition according to inductively coupled plasma optical emission spectroscopy (ICP-OES) was $Na_{0.7}MnO_{2+z.}$

For NCO spheres the same process was employed; however, $CoSO_4$ was added to the $MnSO_4$ solution to achieve 10 % ratio of cobalt in the final product. Chemical composition according to ICP-OES was $Na_{0.6}Co_{0.1}Mn_{0.9}O_{2+z.}$

Coin cells (2016) were prepared with metallic sodium as the negative electrode, and a composite cathode made from active material, acetylene black (Alfa Aesar, >99%), and polyvinylidene fluoride (PVDF, Arkema, Kynar HSV 900) coated on aluminum foil with a weight ratio 6:2:2. Glass fiber (Whatman) was used as a separator. The electrolyte was a 1 M solution of $NaClO_4$ in a mixture of propylene carbonate (PC) and ethylene carbonate (EC) with a weight ratio of 1:1.

Synchrotron *operando* XRD was performed with 2016 coin cells with a 3 mm hole drilled through the casing. Subsequently, they were sealed by Kapton foil with a thickness of 25 µm and epoxy resin. A Na-metal ring was

used as anode (Ø = 16 mm, hole = 3 mm). To ensure a sufficient amount of active material in the beam`s path a pellet was prepared (~10 mg active material) with teflonized acetylene black as a binder, which was then pressed onto aluminum foil.

Physical characterization

Synchrotron X-ray diffraction measurements were performed at the Stanford Synchrotron Radiation Lightsource (beamline 11-3) using an X-ray energy of 12.7 keV (wavelength λ = 0.974 Å) and a MAR345 area detector image plate detector (Rayonix). The sample-detector distance was 166.9 mm, enabling collection of data in the scattering vector, q, range of 0.45 – 5.00 Å^{-1}, where $q = (4\pi\sin\theta)/\lambda$, where λ is the X-ray wavelength and θ is the Bragg angle. 2D diffraction data was reduced to 1D and converted to °2θ using the GSAS2 software for better comparability.[39] In this work, structural developments are depicted for the first discharge (Figure 3-8). All observed changes of the lattice parameters and structural transitions were found to be reversible in the subsequent charge. All *operando* measurements were conducted between 3.8 – 1.5 V vs. Na|Na$^+$.

A Rigaku SmartLab X-ray diffractometer with Cu-K$_\alpha$ radiation (wavelength 1.54 Å) was used for laboratory scale powder XRD measurements in reflection mode (100 mA, 45 kV)

Field emission scanning electron microscopy was performed using a Zeiss Supra 55 FESEM. A Dual-view Optima 5300 DV system was used for ICP-OES. Energy dispersive X-ray spectroscopy (EDS) was performed on a JEOL JEM-2100. For the atom absorptions spectroscopy (AAS) a Varian SpectrAA 220FS spectrometer was used.

Electrochemistry

Galvanostatic cycling was performed on a Neware battery tester system in a coin cell set-up. Galvanostatic cycling for the *operando* XRD was conducted on a MTI CT-3008W-5V1mA-S1 instrument. It should be noted that during the initial charge process for the NCO spheres an interruption in the operando experiment occurred due to technical difficulties. In typical coin cell tests, doped and undoped spheres show similar capacities (Figure 2). Galvanostatic intermittent titration technique was performed on a Biologic VMP3 potentiostat. A constant current pulse of 50 mA was applied for 200 seconds, followed by an OCV relaxation period of 5 hrs. When the voltage changed by less than 2 mV h^{-1} the next current pulse was applied. The data was analyzed using the equation (1) for the diffusion coefficient,

Equation (1) $$D = \frac{4}{\pi}\left(\frac{i\,V_m}{z_A\,F\,S}\right)^2\left[\frac{\left(\frac{dE}{d\delta}\right)}{\left(\frac{dE}{d\sqrt{t}}\right)}\right]^2$$

where V_m is the molar volume of the unit cell, I is the applied current, z_A is the charge number, F is the Faraday's constant, S is the electrode / electrolyte contact area (assumed to be the geometric surface of the electrode), $\frac{dE}{d\delta}$ is the slope of the Coulometric titration curve, $\frac{dE}{d\sqrt{t}}$ is the slope of the linearized plot of the potential E (V) during the current pulse. Volume changes during the cycling process were neglected, as the diffusion coefficient changes significantly (several orders of magnitude), whereas the unit cell volume only changes by several %.

Impedance spectroscopy was performed on a BioLogic VMP 3 with the EC-lab software in a 3-electrode glass cell set-up, using Na-metal as counter and reference electrode, and the active material (composite cathode) as working electrode. After charging / discharging to the respective voltage (50 mA g^{-1}) the potential was kept for 30 min, followed by a relaxation step of 2 hrs and the impedance measurement in OCV.

Manganese dissolution analysis

For the manganese dissolution tests a beaker cell (7.5 mL) was constructed. The cathode was an aluminum foil (50 × 20 mm) coated with the active material covering the complete outer wall. Relatively large amounts (~ 15 mg) of NMO flakes, which show the highest capacity fading, were employed to improve the accuracy of the measurement. The anode was an aluminum wire covered with Na-metal, which was fixed in the center of the cell. Two layers of glass fiber separator were placed between anode and cathode to prevent short circuiting. After adding 6.0 mL of electrolyte the cell was sealed and operated between 10 and 40 cycles. Afterwards, the metallic sodium was dissolved in pure ethanol, all cell parts rinsed with ethanol and combined with the extracted electrolyte. For EDS, the solution was heated (120 °C) on a copper foil until a dry black powder was received. For ICP the solution was acidified and the majority of organic parts where oxidized under heating (CO_2 evolution). Afterwards, the solution was filled to a specific volume with deionized water in a calibrated flask. For AAS the solutions could be used as is after filling it up to a specific volume with deionized water. Assuming all capacity loss is attributed to Mn dissolution, the concentrations should be 22 ppm and 10 ppm in the analysis sample, respectively.

RESULTS & DISCUSSION

Physical characterization

The crystal structures of the as-prepared Na_xMnO_{2+z} (NMO) flakes, NMO hollow spheres, $Na_xCo_{0.1}Mn_{0.9}O_{2+z}$ (NCO) flakes, and NCO hollow spheres were identified to have a hexagonal unit cell of the P2-type class (space group $P6_3/mmc$, Figure S1). For all materials, the lattice parameters were found to be approximately $a = b \approx 2.87$ Å and c ≈ 11.1 Å (for exact values see Table S1). The (hkl) reflections of the hollow spheres are broader than the flakes', as can be seen for the most intense reflection

(002), which has a FWHM of 2θ = 0.30 ° for the NMO spheres, and 0.12 ° for the NMO flakes. Paulsen *et al.*,[40] indicated that the employed short annealing time can lead to stacking faults or inhomogeneity of the Na^+ distribution, which would explain the breadth of the reflections of the spheres. In addition, the flakes had crystallographic texture, and thus, a thorough Rietveld refinement for the *operando* data is challenging and beyond the scope of this publication. Phases were then identified using the Pawley approach; for powder material of flakes a Rietveld refinement was employed (50301-ICSD).

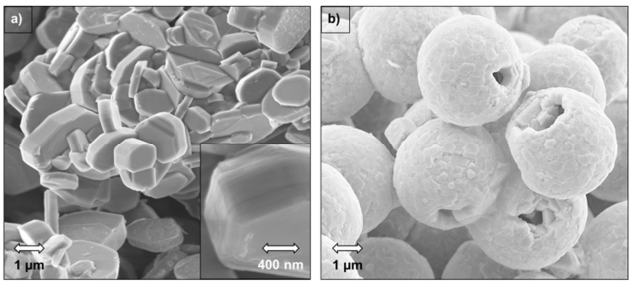

Figure 1. Scanning electron microscopy pictures of a) $Na_{0.6}Co_{0.1}Mn_{0.9}O_2$ flakes, b) $Na_{0.6}Co_{0.1}Mn_{0.9}O_2$ spheres.

The flakes' diameter and thickness vary (Figure 1a). The hollow spheres have an outer diameter of approximately 5 µm, and their outer shells are built up of hexagonal layered flakes (Figure 1b). The shell thickness is comparable with the thickness of the synthesized flakes.

Electrochemical Studies

Galvanostatic cycle tests (20 mA g^{-1}) showed a discharge capacity of 147 mA h g^{-1} for the NMO flakes, 153 mA h g^{-1} for the NCO flakes, 188 mA h g^{-1} for the NMO spheres, and 183 mA h g^{-1} for the NCO spheres, in the first discharge (Figure 2a). Potential reasons for the higher capacity of the spheres are stacking faults as mentioned above, or an increased amount of defects as a result of this synthetic route. NMO flakes show various minor plateaus during discharge indicating Na^+ ordering processes.[27,33,41–43] For the curve of the NMO spheres, these features are enhanced, whereas the NCO flakes do not exhibit most of these minor plateaus. The minor plateaus, and the lack thereof for the doped materials, can easily be seen when plotting the derivative of the potential with respect to the capacity (Figure S2). Cobalt-doped spheres, which have not previously been presented in the literature, show a capacity increase as compared to the NCO flakes, whilst lacking distinct features in the discharge curve as opposed to NMO spheres. For galvanostatic cycle tests at 50 mA h g^{-1} (Figure 2b), NCO flakes (71% capacity retention over 100 cycles & 65% after 150 cycles) show an improvement in cycling stability over NMO flakes (59% / 52%). The same effect of doping is observed for the spherical morphology. While spheres have higher capacity retention than flakes for both doped and undoped material, the Co-doped spheres are more stable than the undoped NMO spheres (75% *vs.* 67% after 100 cycles and 67% *vs.* 58% at 150 cycles). Moreover, Co-doped materials also show better rate capability (Figure 2c). At a current rate of 400 mA g^{-1} (~2.2C), the obtained capacity is 120 mA h g^{-1}. Possible reasons for this are discussed below.

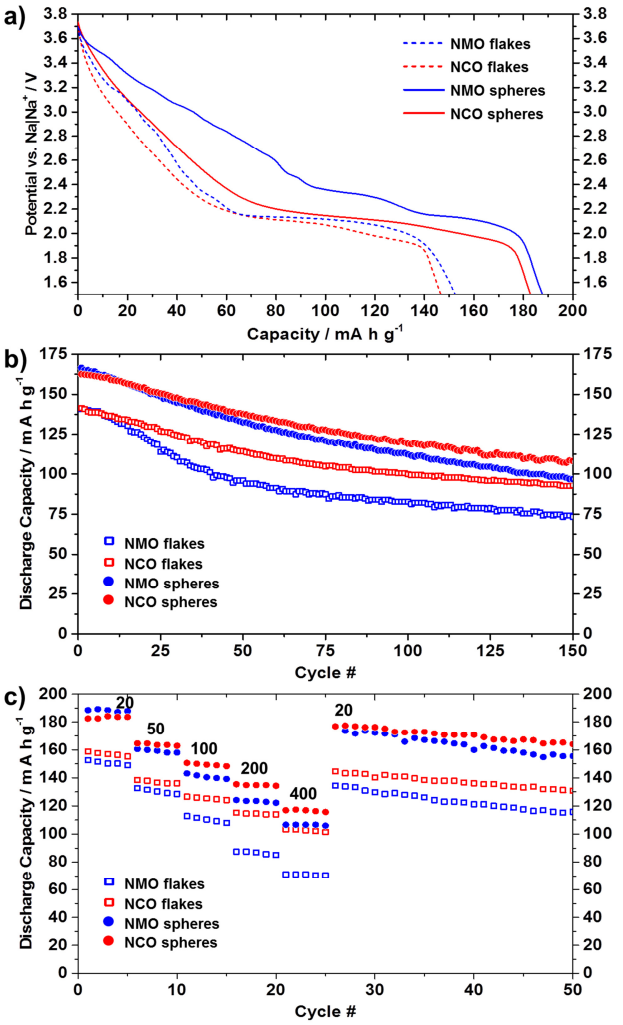

Figure 2. a) Discharge profiles of $Na_{0.6}MnO_2$ flakes, $Na_{0.6}Co_{0.1}Mn_{0.9}O_2$ flakes, $Na_{0.7}MnO_2$ spheres and $Na_{0.6}Co_{0.1}Mn_{0.9}O_2$ spheres for galvanostatic cycling at 20 mA g^{-1}, b) Cycling stability for cycling at 50 mA g^{-1}, c) rate test with labelled current rate in mA g^{-1}.

The observed fading prompted us to investigate Mn^{2+} dissolution from the active materials following a potential disproportionation of Mn^{3+} into Mn^{2+} and Mn^{4+}.[44,45] Calculations on the hypothetical amount of manganese in the electrolyte, assuming that capacity fading is due to manganese dissolution, show that the respective values (~ 10 - 20 ppm) are significantly above the detection limits for ICP, atomic absorption spectroscopy (AAS) and energy-dispersive X-ray spectroscopy (EDX). However, neither ICP, nor AAS, nor EDX measurements of the processed and concentrated electrolyte was able to detect dissolved manganese. The Mn detection limit for these methods is

~ 1 ppm, the amount of dissolved Mn (if any) is < 1 ppm. Consequently, a capacity fading of ≥ 1% should be detectable by these methods if it were resulting from Mn dissolution. Thus, it can be concluded that manganese dissolution has a negligible effect on capacity fading of the P2-type materials presented in this work and cannot explain the differences between the respective materials

Structural Studies

In the following sections, the structural processes as a further cause of the different cycling performances are investigated.

Na_xMnO_{2+z} flakes: During discharge (3.8 V – 1.5 V), the Na^+ content (x) increased from 0.46 to 0.98. The (002) reflection shifts to a higher angle, reflecting a contraction of the unit cell along the *c*-lattice parameter (Figure 3a).

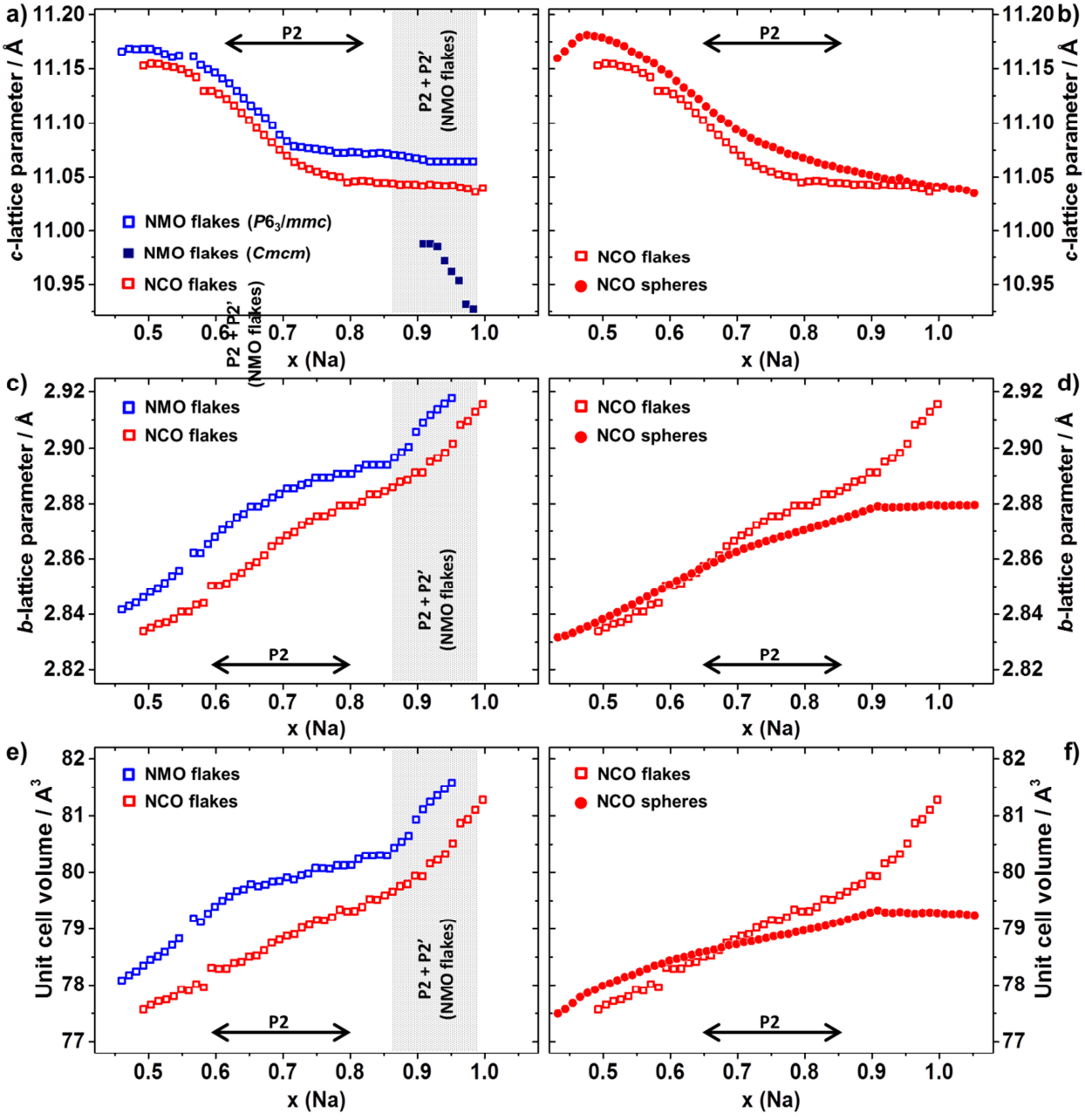

Figure 3. For first discharge, development of the *c*-lattice parameter of a) NMO flakes, the evolving P'2 phase for NMO flakes and NCO flakes, b) NCO flakes and NCO spheres; development of the b-lattice parameter of c) NMO and NCO flakes, d) NCO flakes and NCO spheres; development of the unit cell volume of e) NMO and NCO flakes, f) NCO flakes and NCO spheres. In a), c) and e) the 2 phase region for the NMO flakes was indicated. In this 2 phase region parameters are only shown when could be clearly distinguished.

As Na^+ inserts between the MnO_6-layers, the negative charges of the oxygen between different layers are screened, which moves the layers closer together. The shift of the (010) reflection to lower angles reflects an expansion of the unit cell along the *a*- and *b*-directions (Figure 3c). The cause of this is a decrease of the oxidation state of manganese during discharge, which results in an expansion of the MnO_6-octahedra, and, therefore, an expansion of the *a*- and *b*-lattice parameters.[18,22] Two different phases can be observed during discharge. Initially, the hexagonal P2-type phase of the pristine material is maintained up to a Na^+ loading of ~ 0.87. Then, new reflections occur in the pattern (at 2θ = 21.3, 23.6, 26.2, 29.6, 37.8, 38.9, 43.1, 45.0 °; see Figure 4), and become more intense until the end of the discharge at 1.5 V. Moreover, an overlap of a reflection from the original pattern with a reflection from the newly emerging phase is detectable ($2\theta \approx 10.2°$).

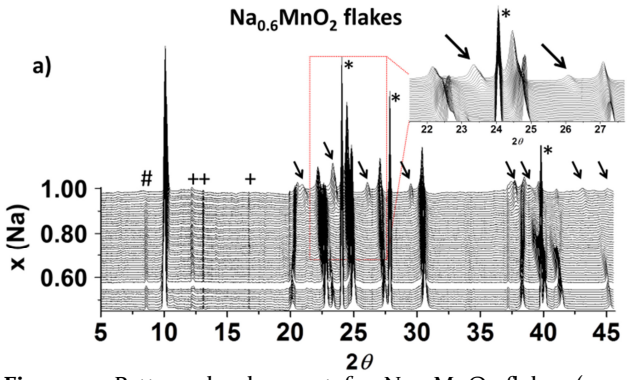

Figure 4. Pattern development for $Na_{0.6}MnO_2$ flakes (synchrotron radiation: λ = 0.974 Å; arrows indicate new reflections; * denote aluminum reflections, + denote epoxy resin, # denotes the hydrated phase[46,47]).

These new reflections are in line with an orthorhombic phase. Typically, this phase is called the P'2 phase.[13,18,48] In Figure 4a the c-lattice development of the initial P2 and the evolving P'2 phase is displayed. Figure 5a shows the diffraction pattern of the NMO flakes at 1.5 V, as well as the (hkl) values for both the initial hexagonal phase, and of the newly formed orthorhombic phase (*Cmcm* space group). The new reflections in the pattern fit well with the orthorhombic phase. Other reflections that occur at similar positions for both the new orthorhombic and the initial hexagonal phase, show a broadening of the reflections in the diffraction pattern due to an overlap of the reflections from the two phases. This phase transition is attributed to the increased amount of Jahn-Teller active Mn^{3+}. The resulting distortion leads to a transformation of the hexagonal to the orthorhombic unit cell, caused by a gliding of the oxygen layer. In the subsequent charge process, the P'2 phase disappears.[48] To check whether the phase change is partially irreversible, the NMO flakes | Na – half cell was cycled offline, and the diffraction patterns at OCV were measured after 5, 10, and 15 cycles. However, no remnant of the P'2 phase could be identified. Thus, it is concluded that the phase transformation is reversible.

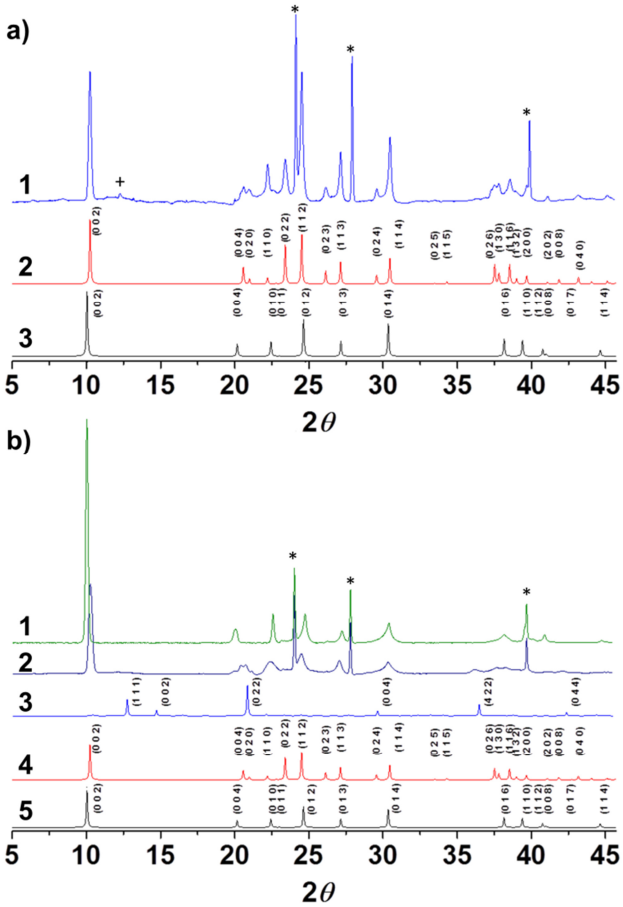

Figure 5. a) Diffraction of NMO flakes at 1.5 V (1, blue), simulated patterns of the *Cmcm* (2, red) and the $P6_3/mmc$ phase (3, black); b) diffraction pattern of NMO spheres at OCV (1, green) and 1.5 V (2, dark blue), simulated patterns of the $P2_13$ (3, light blue), *Cmcm* (4, red), and $P6_3/mmc$ (5, black) symmetry (synchrotron radiation: λ = 0.974 Å, * denote aluminum reflection, + denotes epoxy resin).

$Na_xCo_{0.1}Mn_{0.9}O_{2+z}$ flakes: The Na^+ content changes from 0.49 to 1.0 during discharge. Developments of the lattice parameters, are similar to NMO flakes (Figure 3a, c). The *c*-lattice parameters decrease, by 0.11 Å, and the *b*-lattice parameters increases by 0.08 Å. This is also reflected in the unit cell volume, which, for both material increases by ~ 4 $Å^3$ (4.5%) over the course of the full discharge (Figure 3e). However, during discharge, no new phase could be detected even though the amount of inserted Na^+ was similar to NMO flakes (Figure 6). In contrast to Mn^{3+}, which distorts the structure, Co^{3+} is Jahn-Teller inactive. This suggests that substituting manganese with cobalt on the order of 10% has a stabilizing effect. Moreover, as shown in the section Electrochemical Studies, Co suppresses Na^+ ordering processes in the structure, which otherwise occur for the undoped material. These two effects eliminate structural heterogeneity that inher-

ently occurs as the result of repeated structural transformations, the suppression of these phase transitions is suggested to be the reason for the enhanced cycling stability of the NMO flakes over the NCO flakes.

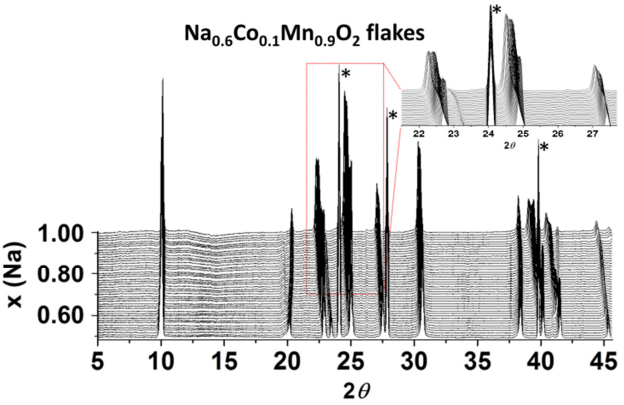

Figure 6. Pattern development for $Na_{0.6}Co_{0.1}Mn_{0.9}O_2$ flakes (synchrotron radiation: λ = 0.974 Å, * denote aluminum reflections).

$Na_xCo_{0.1}Mn_{0.9}O_{2+z}$ spheres: In order to examine whether morphology has an influence on these transitions, spherical $Na_{0.6}Co_{0.1}Mn_{0.9}O_{2+z}$, for which no phase transition is anticipated due to suppression by Co doping, is discussed here. During discharge from 3.8 – 1.5 V, Na^+ content was increased over a wider Na^+ content range: from 0.43 to 1.05. As can be seen in Figure 7, similarly to NCO flakes, no phase change occurs. Thus, the difference in cycling stability between the doped and undoped materials cannot be the consequence of phase transitions. While the change of the *c*-lattice parameter is similar to the NCO flakes, the *b*-lattice parameter, and therefore also the unit cell volume, changes less severely (Figure 3). Thus, the stress on the crystal structure is reduced as compared to the flakes and the volume expansion of the spheres (~ 2.3%) while discharging from 3.8 – 1.5 V is only half the volume change of the flakes (~ 4.8%).

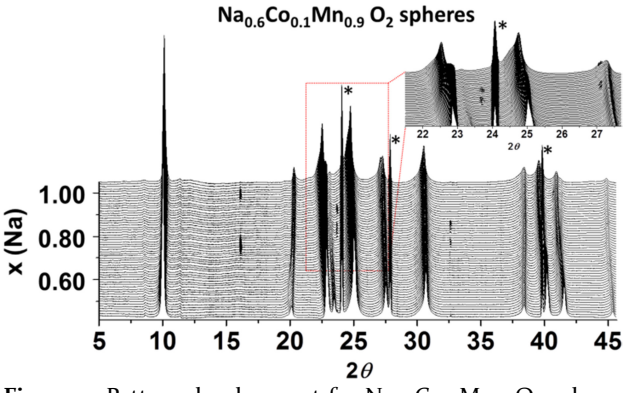

Figure 7. Pattern development for $Na_{0.6}Co_{0.1}Mn_{0.9}O_2$ spheres (synchrotron radiation: λ = 0.974 Å, arrows indicate new reflections, * denotes aluminum reflections).

The effect on the structure is exacerbated by the anisotropic expansion of the lattice parameters. As the *c*-lattice parameter decreases during Na^+ insertion, the expansion of the unit cell volume is based on an increase of the *a*- and *b*-lattice parameter, *i.e.*, an expansion within the plane of MnO_6-octahedra. This difference might be one contributing factor to the superior cycling stability of NCO spheres over NCO flakes.

Comparison of strain distribution:

For undoped materials, the phase change giving rise to additional overlapping reflections makes detailed comparison of structures difficult. However given there is no phase transition at high Na content for Co-doped materials we can directly compare NCO spheres and NCO flakes. Whilst the volume change is greater for the flakes as described above, the shift in (002) reflection to higher angles °2θ for NCO spheres is particularly modest given the higher Na content despite the ability to accommodate a slightly larger amount of Na in the structure than the NCO flakes (1.05 Na for NCO spheres compared to 1.00 Na for NCO flakes). Whilst one may not be able to infer much from the contraction along the *c*-direction, observable differences in Full Width at Half Maximum (FWHM) of higher order reflections are apparent for the (002) and (004) for the NCO spheres in Table S2; here we look at relative ratio of $FWHM_{(004)}$ / $FWHM_{(002)}$. For the NCO flakes, whilst there is no appreciable change when increasing the Na content from 0.6 (OCV) to 1.0 (within the error), there is a modest observable variation at low sodium content of 0.49 Na ($FWHM_{(004)}$ / $FWHM_{(002)}$ = 1.18). This possibly indicates a larger distribution of strain in the material. The ratio $FWHM_{(004)}$ / $FWHM_{(002)}$ is larger for NCO spheres; whilst it is ~1 around OCV (0.5 - 0.6 Na^+) and > 1 moving away from OCV in either direction *i.e.* for Na^+ < 0.5 (1:1.39) and Na^+ > 0.6. This suggests that, although there is a lesser volume change for the spheres, there is a greater degree of strain distribution in the material at high and low Na loading, implying possible inhomogeneities in the distribution of Na concentration throughout the material. Whilst the mechanism by which this takes place is unclear, it is postulated that this ability to accommodate strain rather than release it in the form of lattice contraction may act to *i)* protect the material from structural fatigue during successive cycling leading to superior cycling stability and *ii)* facilitate the broader range of sodium content. Whilst it is not possible to observe such difference in FWHM for NMO spheres for aforementioned reasons, given the similar performance of the materials, it is hypothesized that the same strain accommodation ability may also be one of the reasons for superior cycling stability and capacity in these materials.

Na_xMnO_{2+z} spheres: Na^+ content increases from 0.35 to 1.02 during discharge. The development of the diffraction patterns of NMO spheres show three different phases in the course of one discharge (Figure 8). In the charged state, *i.e.* at Na^+ contents between 0.35 – 0.49, the diffraction pattern shows a two phase region with reflections from a non-hexagonal phase. From a Na^+ loading of 0.82, new reflections (2θ ≈ 20.8, 36.3, 42.3 °) are observed.

Moreover, a significant broadening of the (002) reflection ($2\theta \approx 10.3°$) at the end of the discharge is visible.

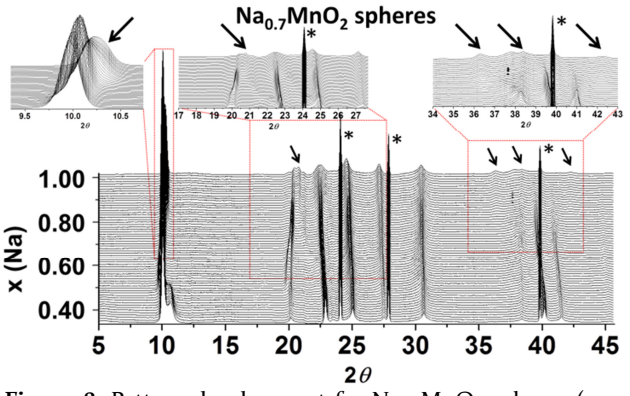

Figure 8. Pattern development for $Na_{0.7}MnO_2$ spheres (synchrotron radiation: λ = 0.974 Å, arrows indicate new reflections, * denote aluminum reflections)

The reflections at low sodium content are attributed to a so-called 'Z'-phase, which represents a structure in which, based on the initial P2-type structure, the layers of MnO_6-octahedra are shifted.[18,48] Talaie *et al.* modelled this phase with an O2 2x2x10 supercell, in which the position of the respective layers was randomized.[18] This phase, however, disappeared during discharge. From a Na^+ content of 0.49, only the initial P2-stacking order is detectable. In Figure S3a the c-lattice of the original P2- and the 'Z'-phase of the NMO spheres are shown. In the two phase region, *i.e.*, at a low Na^+ content, the *c*-lattice of the P2-phase stays rather constant. With the disappearing of the 'Z'-phase the *c*-lattice of the P2-phase increases until the electrostatic interaction between Na^+ and the Mn-O-layers result in a decrease of the interlayer distance. Over the development of the single P2-phase region, the *b*-lattice parameter does not change significantly, leading to a smaller volume change of the NMO spheres compared to NMO flakes (Figure S3b and c).

The occurrence of the P'2 phase is not as clear as for the NMO flakes. The new reflections at 20.8 and 42.3 as well as the broadening around 10.3 °2θ could indicate the P'2 phase. However, a new reflection at $2\theta \approx 36.8$ ° is not in line with an emerging P`2 phase, which suggests that another new phase is formed. Moreover, the prominent reflections between 23 and 30 °$2\theta$ of a unit cell with the *Cmcm* space group are absent. This suggests that the contribution from the P`2 phase is small. A structure that could explain the unidentified reflection at 36, but also the aforementioned reflections at 20 and 42, is cubic Na_3MnO_4 (space group $P2_13$). Although this is not in line with the layered oxide structure, the precursor for our P2-type NMO for the spheres was amorphous MnO_2, which is converted to Mn_2O_3 at the synthesis temperature and crystallizes in a cubic structure. Thus, a minor part of the Mn_2O_3 precursor might not have been transformed to P2-type NMO during the annealing process, and has taken up Na^+ at potentials of 2.2 – 1.5 V *vs.* $Na|Na^+$, possibly resulting in the detectable presence of this phase. A shoulder at 2θ = 20.6 °, where Mn_2O_3 has its most intense reflection, supports this hypothesis. Figure 5b shows the diffraction pattern of the NMO spheres at OCV and at 1.5 V, as well as the (hkl) values for a cubic $P2_13$ space group, the initial P2 phase, and of the potentially formed P'2 phase. Sharma *et al.* recently showed that, even for the same material, the formation of the P'2 phase depends on the current rate at which the material is cycled, *i.e.,* on kinetic factors.[30] These could be influenced by stacking faults or defects in the structure. Different tendencies for NMO flakes and spheres to form the P'2 phase could therefore be attributed to different kinetic behavior, such as nucleation of the new phase. The smaller changes in the unit cell volume, in combination with the lower concentration of the P'2 phase throughout cycling reduce structural stresses and fatigue. This is considered to be one of the leading contributors to the observed higher cycling stability of the materials with spherical morphology.

The NCO spheres do not show the impurity attributed to the Mn2O3 precursor. Moreover, the Co-doped materials have a larger average crystallite size than the undoped analogues, as indicated by sharper reflections in the XRD pattern. This is in line with findings by Paulsen et al. that incorporating Co into the structure facilitates the formation of the P2-phase during synthesis.[40] Thus, the Co-doped materials are anticipated to contain a lower degree of amorphous/untransformed material, which can crystallize in the suspected cubic phase. In our measurements, the 'Z'-phase was not observed for the NCO spheres. However, Na^+ content during the initial charge might just not have been decreased sufficiently to induce the formation of the 'Z'-phase.

Diffusion & Conductivity Properties

Filling up a given structure with Na^+ influences the mobility of these Na-ions, and thus affects diffusion properties. As structural changes result in different pathways along which Na^+ can move in the structure, phase transitions also have an effect on diffusion. To elucidate these changes, galvanostatic intermittent titration technique and Electrochemical Impedance Spectroscopy were performed. Figure 9 shows the development of the effective diffusion coefficient during the course of one discharge as measured by GITT. Minima of the diffusion coefficient are indicative of the exhaustion of certain processes or structural rearrangements. Between a Na^+ content of 0.45 and 0.67, *i.e.* the solid solution region, diffusion coefficients are comparable, and develop in parallel, for all materials. The diffusion coefficient is between 10^{-9} – 10^{-10} cm^2 s^{-1}, which is considered to indicate fast diffusion processes for an insertion material.

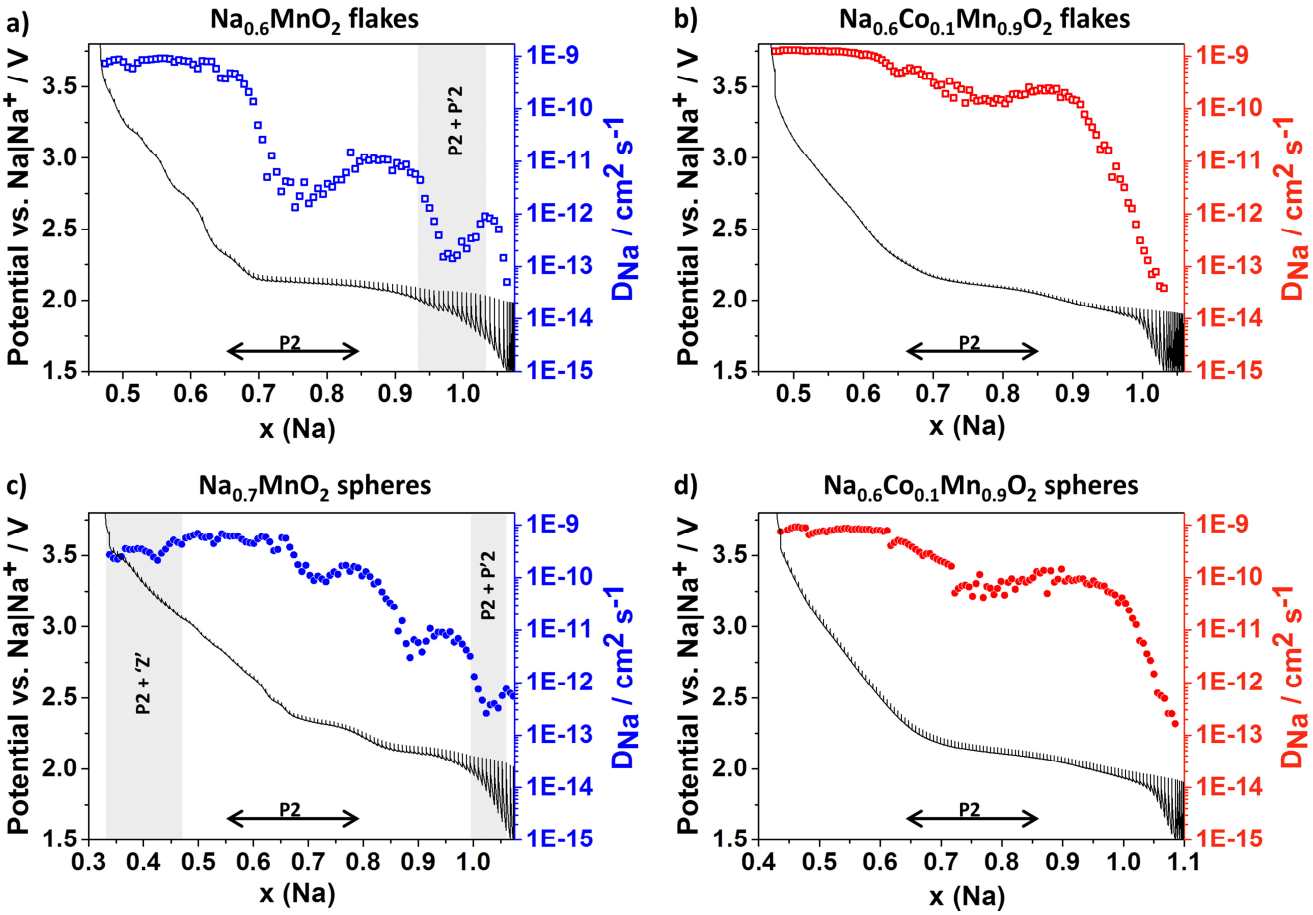

Figure 9. Development of the diffusion coefficient during discharge as measured by GITT for a) $Na_{0.7}MnO_2$ flakes, b) $Na_{0.6}Co_{0.1}Mn_{0.9}O_2$ flakes, c) $Na_{0.6}MnO_2$ spheres, d) $Na_{0.6}Co_{0.1}Mn_{0.9}O_2$ spheres. For the undoped materials the two phase regions are indicated.

Minor changes (*i.e.* minima) can be observed in this region for undoped NMO flakes (Figure 9a) and spheres (Figure 9c), which correlate well with small plateaus in the discharge curve that signify Na^+ ordering processes (Figure 2a). At a Na^+ content of approximately 0.67, diffusion coefficients for all materials start decreasing. For Na^+ contents beyond that, the values diverge. NMO flakes show a local minimum at a Na^+ content of approximately 0.77 ($D_{Na+} \approx 10^{-12}$ cm^2 s^{-1}), followed by an increase and, subsequently, another minimum ($D_{Na+} \approx 10^{-13}$ cm^2 s^{-1}). Both the electrochemistry and GITT measurements suggest the start of a first structural transition at a Na^+ content of ~ 0.7. The diffraction data, however, did not show any phase change in this region (Figure 4). This minimum can be explained by high concentration overpotential, which results in a rearrangement of the Na-ions between the MnO_6-layers and thus in changes of the diffusion properties. The second minimum at x = 0.97 is attributed to the phase transition towards the orthorhombic phase as observed by synchrotron XRD (Figure 4 & 5a). GITT measurements suggest the phase transition takes place at a slightly higher Na^+ content as indicated by XRD. This difference can possibly be attributed to the nature of the GITT analysis. For the calculation of the Na^+ content, only the Na^+ insertion induced by the applied current is considered, but diffusion of Na^+ in the opposite direction during the rest periods is neglected. This is substantiated by the high voltage gradient during the rest period of the GITT measurement in the major plateau at ~ 2.2 – 2.1 V (Figure S4). Thus, the Na^+ content is overestimated.

Except for this second minimum at high Na^+ contents, NCO flakes (Figure 9b) shows the same trend as NMO flakes, *i.e.*, the same position for main minima and maxima, albeit at considerable higher values for the diffusion coefficient ($D_{Na+} \approx 10^{-12}$ cm^2 s^{-1} for the minimum). This increase is attributed to the effect of the Co.

For NMO spheres (Figure 9c) the trend is similar to the NMO flakes. However, the structural transition at ~ 0.7 develops first at a minima value around $D_{Na+} \approx 10^{-10}$ cm^2 s^{-1}, before coming down to similar low diffusion coefficient values ($D_{Na+} \approx 10^{-12}$ cm^2 s^{-1}) at Na^+ content of x ≈ 0.88. Moreover, a third minimum occurs at a Na^+ content of ~ 1.02. The diffusion coefficient of the last minimum is comparable to the minimum of the NMO flakes which was attributed to the phase transition towards the P'2 phase. This substantiates the phase transition from the

hexagonal $P6_3/mmc$ to the orthorhombic *Cmcm* phase as hypothesized in the discussion on structural changes. The minimum which indicates the phase transition towards an orthorhombic phase for both NMO materials cannot be seen for the Co-doped flakes nor spheres. This is in line with suppression of the phase transition as concluded in the Structural Studies section.

Over the whole P2-phase region both NCO flakes and spheres exhibit higher diffusion coefficients than the undoped analogues. This is explained by enhancement of the Na^+ conductivity as a result of Co-doping. This higher conductivity is also reflected in the rate capability, which is better for the Co-doped materials (Figure 2c). The reason for the lower conductivity of the undoped material is attributed to the high resistivity given by the Mn^{+3}, which is a Jahn-Teller active ion.[49,50] For $LiMnO_2$, doping results in a suppression of the Jahn-Teller effect, which lowers the diffusion barrier and thus increases ionic conductivity.[51] A similar effect is assumed here.

These findings have been confirmed by electrochemical impedance spectroscopy (Table S3) in a 3-electrode set-up for NMO and NCO flakes. Even though the trend for the charge-transfer resistance is similar in the beginning, *i.e.,* in the first charge and the first part of the subsequent discharge, the value for NMO flakes and NCO flakes diverge shortly before the onset of the pronounced plateau at approximately 2.5 V. In the plateau, whilst there are no phase transitions observed in the XRD, the charge transfer resistance of NMO starts to increase by one order of magnitude larger than the respective value for NCO flakes. This provides strong evidence in support of the hypothesis that the stabilizing effect of Co is not limited to structural stabilization, but also improves cycling stability through enhanced ionic conductivity in the electrode.

CONCLUSION

Na_xMnO_{2+z} and $Na_xCo_{0.1}Mn_{0.9}O_{2+z}$ were synthesized in two different morphologies, hexagonal flakes and hollow spheres. Their structural and diffusion properties in the context of sodium-ion battery cathodes were investigated using operando synchrotron X-ray diffraction, galvanostatic intermittent titration technique and electrochemical impedance spectroscopy. In addition, no dissolved Mn could be detected in the electrolyte over the course of cycling and is therefore thought to play a negligible role. Na_xMnO_{2+z} flakes undergo partial phase transition towards an orthorhombic crystal system upon the insertion of Na^+, while Co-doping on the order of 10% suppresses these structural transformations. The lack of repeated phase transitions might reduce inhomogeneity in the structure and, together with the suppression of Na^+ ordering processes, explain the better cycling stability of the doped material. In addition to the beneficial structural effects, Co-doping is also shown to have a positive influence on Na-ion transport within the structure. This not only explains the better rate capability of doped *vs.* undoped material, but could also contribute towards improved cycling stability.

Superior cycling stability of Co-doped spheres compared to doped flakes is attributed to the reduced volume expansion and contraction for the spheres. Thus, reduced strain within the structure of the spheres is one explanation for this difference. Moreover, the spherical material shows an increase in capacity, which is attributed to structural defects.

The effects of Co-doping are different from the intended effect for other transition metals. Incorporating elements such as Ni or Fe into the structure aims at increasing energy density by exploiting the high potential of their respective redox reactions. Yabuuchi *et al.* showed that incorporating 50% of Fe into the structure increases cycling stability by suppressing Na^+ ordering processes;[8] however, Fe does not prevent phase transformation in the lower voltage region.[18,22,48] Ni-substitution, on the other hand, does not eliminate Na^+ ordering processes, but enhances structural stability by alleviating the Jahn-Teller distortion and delaying the phase transitions between 2.1 – 1.5 V.[21,24,27,47] Incorporating a relatively small amount of Co – as low as 10% – into the structure enhances Na^+ conductivity, suppresses Na^+ ordering and prevents phase transformation between 2.1 – 1.5 V, and thus allows a more reversible exploitation of the capacity that can be obtained in this voltage region.

A combined approach of the two presented material optimization route, *i.e.,* doping and morphology optimization, has been shown to be most successful in attaining superior capacity and cycling stability for the investigated materials.

ACKNOWLEDGEMENT

The authors thank Matthias Schmidt and Charlotte Brzozowski for the helpful support during their internship.

ASSOCIATED CONTENT

Supporting Information. The supporting information comprises information on X-ray diffraction data of the pristine materials, the derivative of the potential with respect to capacity for NMO and NCO spheres spheres, changes of the FWHM for NCO flakes and spheres, development of the lattice parameters for NMO spheres, relaxation behaviour of NMO flakes during the GITT measurement, and EIS data for NMO and NCO flakes.

AUTHOR INFORMATION

Corresponding Author

* Email: Madhavi@ntu.edu.sg

Author Contributions

All authors have given approval to the final version of the manuscript. ‡ N.B. and S.H. contributed equally to this manuscript.

Funding Sources

This work was financially supported by the Singapore National Research Foundation under its Campus for Research Excellence and Technological Enterprise (CREATE) programme. A.M.W. was fully supported and J.N.W. was partially supported by the Department of Energy, Laboratory Direct Research and Development funding, under contract DE-AC02-76SF00515. Use of the Stanford Synchrotron Radiation Lightsource, SLAC National Accelerator Laboratory, is supported by the U.S. Department of Energy, Office of Science, Office of Basic Energy Sciences under Contract No. DE-AC02-76SF00515.

REFERENCES

(1) Kundu, D.; Talaie, E.; Duffort, V.; Nazar, L. F. The Emerging Chemistry of Sodium Ion Batteries for Electrochemical Energy Storage. *Angew. Chemie Int. Ed.* **2015**, No. 54, 3431–3448.

(2) Palomares, V.; Serras, P.; Villaluenga, I.; Hueso, K. B.; Carretero-González, J.; Rojo, T. Na-Ion Batteries, Recent Advances and Present Challenges to Become Low Cost Energy Storage Systems. *Energy Environ. Sci.* **2012**, *5* (3), 5884–5901.

(3) Palomares, V.; Casas-Cabanas, M.; Castillo-Martínez, E.; Han, M. H.; Rojo, T. Update on Na-Based Battery Materials. A Growing Research Path. *Energy Environ. Sci.* **2013**, *6* (8), 2312–2337.

(4) Yabuuchi, N.; Kubota, K.; Dahbi, M.; Komaba, S. Research Development on Sodium-Ion Batteries. *Chem. Rev.* **2014**, No. 114, 11636–11682.

(5) Ellis, B. L.; Nazar, L. F. Sodium and Sodium-Ion Energy Storage Batteries. *Curr. Opin. Solid State Mater. Sci.* **2012**, *16* (4), 168–177.

(6) Komaba, S.; Murata, W.; Ishikawa, T.; Yabuuchi, N.; Ozeki, T.; Nakayama, T.; Ogata, A.; Gotoh, K.; Fujiwara, K. Electrochemical Na Insertion and Solid Electrolyte Interphase for Hard-Carbon Electrodes and Application to Na-Ion Batteries. *Adv. Funct. Mater.* **2011**, *21* (20), 3859–3867.

(7) Komaba, S.; Ishikawa, T.; Yabuuchi, N.; Murata, W.; Ito, A.; Ohsawa, Y. Fluorinated Ethylene Carbonate as Electrolyte Additive for Rechargeable Na Batteries. *ACS Appl. Mater. Interfaces* **2011**, *3*, 4165–4168.

(8) Yabuuchi, N.; Kajiyama, M.; Iwatate, J.; Nishikawa, H.; Hitomi, S.; Okuyama, R.; Usui, R.; Yamada, Y.; Komaba, S. P2-Type Na(x)[Fe(1/2)Mn(1/2)]O2 Made from Earth-Abundant Elements for Rechargeable Na Batteries. *Nat. Mater.* **2012**, *11* (6), 512–517.

(9) Emsley, J. *Nature's Building Blocks: An A-Z Guide to the Elements*; Oxford University Press, 2001.

(10) Han, M. H.; Gonzalo, E.; Singh, G.; Rojo, T. A Comprehensive Review of Sodium Layered Oxides: Powerful Cathodes for Na-Ion Batteries. *Energy Environ. Sci.* **2015**, *8* (1), 81–102.

(11) Kubota, K.; Yabuuchi, N.; Yoshida, H.; Dahbi, M.; Komaba, S. Layered Oxides as Positive Electrode Materials for Na-Ion Batteries. *MRS Bull.* **2014**, *39* (05), 416–422.

(12) Delmas, C.; Fouassier, C.; Hagenmuller, P. Structural Classification and Properties of the Layered Oxides. *Phys. B+C* **1980**, *99* (1-4), 81–85.

(13) Parant, J.; Olazcuaga, R.; Devalette, M.; Fouassier, C.; Hagenmuller, P. Sur Quelques Nouvelles Phases de Formule NaxMnO2 (x </= 1). *J. Solid State Chem.* **1971**, *3*, 1–11.

(14) Delmas, C.; Braconnier, J. J.; Fouassier, C.; Hagenmuller, P. Electrochemical Intercalation of Sodium in NaxCoO2 Bronzes. *Solid State Ionics* **1981**, *3-4*, 165–169.

(15) Braconnier, J. J.; Delmas, C.; Hagenmuller, P. Etude Par Desintercalation Electrochimique Des Systemes NaxCrO2 et NaxNiO2. *Mater. Res. Bull.* **1982**, *17* (8), 993–1000.

(16) Molenda, J.; Delmas, C.; Hagenmuller, P. Electronic and Electrochemical Properties of NaxCoO2 Cathode. *Sol. Stat. Ion.* **1983**, *10*, 431.

(17) Mendiboure, A.; Delmas, C.; Hagenmuller, P. Electrochemical Intercalation and Deintercalation of NaxMnO2 Bronzes. *J. Solid State Chem.* **1985**, *57* (3), 323–331.

(18) Nazar, L.; Talaie, E.; Duffort, V.; Smith, H.; Fultz, B. Structure of the High Voltage Phase of Layered P2-Na2/3-z[Mn1/2Fe1/2]O2 and the Positive Effect of Ni Substitution on Its Stability. *Energy Environ. Sci.* **2015**, *8*, 2512–2523.

(19) Guignard, M.; Didier, C.; Darriet, J.; Bordet, P.; Elkaïm, E.; Delmas, C. P2-NaxVO2 System as Electrodes for Batteries and Electron-Correlated Materials. *Nat. Mater.* **2012**, *11* (11), 1–7.

(20) Li, Z.-Y.; Gao, R.; Sun, L.; Hu, Z.; Liu, X. Designing an Advanced P2-Nao.67Mno.65Nio.2Coo.15O2 Layered Cathode Material for Na-Ion Batteries. *J. Mater. Chem. A* **2015**, *3* (31), 16272–16278.

(21) Yuan, D.; Hu, X.; Qian, J.; Pei, F.; Wu, F.; Mao, R.; Ai, X.; Yang, H.; Cao, Y. P2-Type Na0.67Mn0.65Fe0.2Ni0.15O2 Cathode Material with High-Capacity for Sodium-Ion Battery. *Electrochim. Acta* **2014**, *116*, 300–305.

(22) Pang, W. K.; Kalluri, S.; Peterson, V. K.; Sharma, N.; Kimpton, J.; Johannessen, B.; Liu, H. K.; Dou, S. X.; Guo, Z. Interplay between Electrochemistry and Phase Evolution of the P2-Type Nax(Fe1/2Mn1/2)O2 Cathode for Use in Sodium-Ion Batteries. *Chem. Mater.* **2015**, *27* (8), 3150–3158.

(23) Jung, Y. H.; Christiansen, A. S.; Johnsen, R. E.; Norby, P.; Kim, D. K. In Situ X-Ray Diffraction Studies on Structural Changes of a P2 Layered Material during Electrochemical Desodiation/Sodiation. *Adv. Funct. Mater.* **2015**, *25* (21), 3227–3237.

(24) Wen, Y.; Wang, B.; Zeng, G.; Nogita, K.; Ye, D.; Wang, L. Electrochemical and Structural Study of Layered P2-Type Na(2/3)Ni(1/3)Mn(2/3)O2 as Cathode Material for Sodium-Ion Battery. *Chem. Asian J.* **2015**, *10* (3), 661–666.

(25) Park, K.; Han, D.; Shon, J.; Doo, S. G.; Lee, S. Characterization of a Thin, Uniform Coating on P2-Type Na2/3Fe1/2Mn1/2O2 Cathode Material for Sodium-Ion Batteries. *RSC Adv.* **2015**, *5* (9), 6340–6344.

(26) Buchholz, D.; Vaalma, C.; Chagas, L. G.; Passerini, S. Mg-Doping for Improved Long-Term Cyclability of Layered Na-Ion Cathode Materials – The Example of P2-Type NaxMg0.11Mn0.89O2. *J. Power Sources* **2015**, *282*, 581–585.

(27) Lu, Z.; Dahn, J. R. In Situ X-Ray Diffraction Study of P2-Na[2/3][Ni[1/3]Mn[2/3]]O[2]. *J. Electrochem. Soc.* **2001**, *148* (11), A1225.

(28) Cheng, J.-H.; Pan, C.-J.; Lee, J.-F.; Chen, J.-M.; Guignard, M.; Delmas, C.; Carlier, D.; Hwang, B. Simultaneous Reduction of Co 3+ and Mn 4+ in P2-Na 2/3 Co 2/3 Mn 1/3 O 2 As Evidenced by X-Ray Absorption Spectroscopy during Electrochemical Sodium Intercalation. *Chem. Mater.* **2014**, *26* (2), 1219–1225.

(29) Billaud, J.; Singh, G.; Armstrong, A. R.; Gonzalo, E.; Roddatis, V.; Armand, M.; Rojo, T.; Bruce, P. G. Na0.67Mn(1-x)MgxO2 (0</=x</=0.2): A High Capacity Cathode for Sodium-Ion Batteries. *Energy Environ. Sci.* **2014**, *7* (4), 1387–1391.

(30) Sharma, N.; Tapia-Ruiz, N.; Singh, G.; Armstrong, A. R.; Pramudita, J. C.; Brand, H. E. A.; Billaud, J.; Bruce, P. G.; Rojo, T. Rate Dependent Performance Related to Crystal Structure Evolution of Na0.67Mn0.8Mg0.2O2 in a Sodium-Ion Battery. *Chem. Mater.* **2015**, *27* (20), 6976–6986.

(31) Hasa, I.; Buchholz, D.; Passerini, S.; Scrosati, B.; Hassoun, J. High Performance Na0.5[Ni0.23Fe0.13Mn0.63]O2 Cathode for Sodium-Ion Batteries. *Adv. Energy Mater.* **2014**, *4* (15), 1400083 (1–7).

(32) Chagas, L. G.; Buchholz, D.; Vaalma, C.; Wu, L.; Passerini, S. P-Type NaxNi0.22Co0.11Mn0.66O2 Materials: Linking Synthesis with Structure and Electrochemical Performance. *J. Mater. Chem. A* **2014**, *2* (47), 20263–20270.

(33) Bucher, N.; Hartung, S.; Gocheva, I.; Cheah, Y. L.; Srinivasan, M.; Hoster, H. E. Combustion-Synthesized Sodium Manganese (cobalt) Oxides as Cathodes for Sodium Ion Batteries. *J. Solid State Electrochem.* **2013**, *17* (7), 1923–1929.

(34) Stoyanova, R.; Carlier, D.; Sendova-Vassileva, M.; Yoncheva, M.; Zhecheva, E.; Nihtianova, D.; Delmas, C. Stabilization of over-Stoichiometric Mn4+ in Layered Na2/3MnO2. *J. Solid State Chem.* **2010**, *183* (6), 1372–1379.

(35) Bucher, N.; Hartung, S.; Nagasubramanian, A.; Cheah, Y. L.; Hoster, H. E.; Madhavi, S. Layered NaxMnO$_2$+z in Sodium Ion Batteries-Influence of Morphology on Cycle Performance. *ACS Appl. Mater. Interfaces* **2014**, *6* (11), 8059–8065.

(36) Eriksson, T. A.; Lee, Y. J.; Hollingsworth, J.; Reimer, J. A.; Cairns, E. J.; Zhang, X. F.; Doeff, M. M. Influence of Substitution on the Structure and Electrochemistry of Layered Manganese Oxides. *Chem. Mater.* **2003**, *15* (23), 4456–4463.

(37) Dollé, M.; Hollingsworth, J.; Richardson, T. J.; Doeff, M. M. Investigation of Layered Intergrowth LixMyMn(1-y)O(2+z) (M=Ni, Co, Al) Compounds as Positive Electrodes for Li-Ion Batteries. *Solid State Ionics* **2004**, *175* (1-4), 225–228.

(38) Dollé, M.; Patoux, S.; Doeff, M. M. Layered Manganese Oxide Intergrowth Electrodes for Rechargeable Lithium Batteries. 1. Substitution with Co or Ni. *Chem. Mater.* **2005**, *17* (10), 1036–1043.

(39) Toby, B. H.; Von Dreele, R. B. GSAS-II: The Genesis of a Modern Open-Source All Purpose Crystallography Software Package. *J. Appl. Crystallogr.* **2013**, *46* (2), 544–549.

(40) Paulsen, J.; Dahn, J. R. Studies of the Layered Manganese Bronzes, Na2/3[Mn(1-x)Mx]O2 with M=Co, Ni, Li, and Li2/3[Mn(1-x)Mx]O2 Prepared by Ion-Exchange. *Solid State Ionics* **1999**, *126* (1-2), 3–24.

(41) Berthelot, R.; Carlier, D.; Delmas, C. Electrochemical Investigation of the P2–NaxCoO2 Phase Diagram. *Nat. Mater.* **2011**, *10* (1), 74–80.

(42) Platova, T. A.; Mukhamedshin, I. R.; Alloul, H.; Dooglav, A. V.; Collin, G. Nuclear Quadrupole Resonance and X-Ray Investigation of the Structure of Na2/3CoO2. *Phys. Rev. B* **2009**, *80* (22), 224106 (1–11).

(43) Zhang, P.; Capaz, R.; Cohen, M.; Louie, S. Theory of Sodium Ordering in NaxCoO2. *Phys. Rev. B* **2005**, *71* (15), 153102.

(44) Dong H, J.; Shin, Y. J.; Oh, S. M. Dissolution of Spinel Oxides and Capacily Losses in 4 V Li/LixMn2O4 Cells. *J. Electrochem. Soc.* **1996**, *143* (7), 2204–2211.

(45) Wu, Y. P.; Rahm, E.; Holze, R. Effects of Heteroatoms on Electrochemical Performance of Electrode Materials for Lithium Ion Batteries. *Electrochim. Acta* **2002**, *47* (21), 3491–3507.

(46) Caballero, A.; Hernán, L.; Morales, J.; Sánchez, L.; Santos Peña, J.; Aranda, M. a. G. Synthesis and Characterization of High-Temperature Hexagonal P2-Nao.6MnO2 and Its Electrochemical Behaviour as Cathode in Sodium Cells. *J. Mater. Chem.* **2002**, *12* (4), 1142–1147.

(47) Lee, D. H.; Xu, J.; Meng, Y. S. An Advanced Cathode for Na-Ion Batteries with High Rate and Excellent Structural Stability. *Phys. Chem. Chem. Phys.* **2013**, *15* (9), 3304–3312.

(48) Mortemard de Boisse, B.; Carlier, D.; Guignard, M.; Bourgeois, L.; Delmas, C. P2-NaxMn1/2Fe1/2O2 Phase Used as Positive Electrode in Na Batteries: Structural Changes Induced by the Electrochemical (De)intercalation Process. *Inorg. Chem.* **2014**, *53* (20), 11197–11205.

(49) Sharma, P. K.; Moore, G. J.; Zhang, F.; Zavalij, P.; Whittingham, M. S. Electrical Properties of the Layered Manganese Dioxides MxMn(1-y)CoyO2, M = Na,K. *Electrochem. Solid State Lett.* **1999**, *2* (10), 494–496.

(50) Robert Armstrong, A.; Gitzendanner, R. The Intercalation Compound Li(Mno.9Coo.1)O2 as a Positive Electrode for Rechargeable Lithium Batteries. *Chem. Commun.* **1998**, *85* (17), 1833–1834.

(51) Kong, F.; Longo, R. C.; Park, M.-S.; Yoon, J.; Yeon, D.-H.; Park, J.-H.; Wang, W.-H.; KC, S.; Doo, S.-G.; Cho, K. Ab Initio Study of Doping Effects on LiMnO2 and Li2MnO3 Cathode Materials for Li-Ion Batteries. *J. Mater. Chem. A* **2015**, *3* (16), 8489–8500.

ToC:

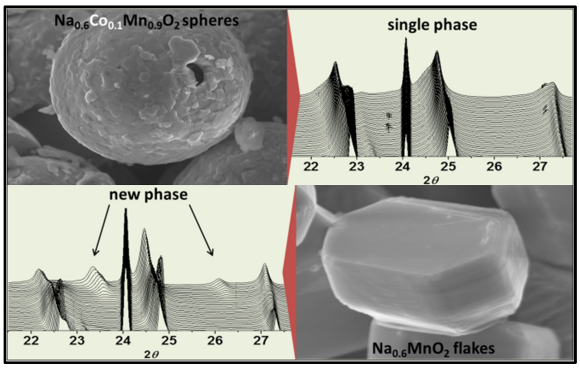

Supporting information for

P2-$Na_xCo_yMn_{1-y}O_2$ (y = 0, 0.1) as Cathode Materials in Sodium-Ion Batteries – Investigation of Doping and Morphology to Enhance Cycling Stability

Nicolas Bucher[‡1,2,3)], Steffen Hartung[‡1,2,3)], Joseph B. Franklin[4)], Anna M. Wise[5)], Linda Y. Lim[5,6)], Han-Yi Chen[1,2,3)], Johanna Nelson Weker[5)], Michael F. Toney[5)], Madhavi Srinivasan[1,3,4*]

[1] TUM CREATE, Singapore 138602, Singapore

[2] Technical University of Munich, Garching 85748, Germany

[3] School of Materials Science and Engineering, Nanyang Technological University, Singapore 639798, Singapore

[4] Energy Research Institute at NTU (ERI@N), Nanyang Technological University, Research Techno Plaza, 50 Nanyang Drive, Singapore

[5] Stanford Synchrotron Radiation Lightsource, SLAC National Accelerator Laboratory, 2575 Sand Hill Road, Menlo Park, CA, United States

[6] Department of Materials Science and Engineering, Stanford University, 496 Lomita Mall, Stanford, CA, United States.

[‡] Nicolas Bucher and Steffen Hartung contributed equally to this manuscript

Content: Figure S1 shows the X-ray diffraction pattern and (hkl) positions of $Na_{0.6}MnO_2$ (NMO) flakes, $Na_{0.6}Co_{0.1}Mn_{0.9}O_2$ (NCO) flakes, $Na_{0.7}MnO_2$ (NMO) spheres and $Na_{0.6}Co_{0.1}Mn_{0.9}O_2$ (NCO) spheres. Table S1 shows the refinement parameters for (NMO) flakes, (NCO) flakes, (NMO) spheres and (NCO) spheres. Subsequently, Figure S2 shows the derivative of the potential with respect to the capacity to illustrate Na^+ ordering processes. Table S2, the development of the full width at half maximum (FWHM) of the NCO flakes and NCO spheres, as well as their quotient, is shown at several different Na-loadings.The b- and c-lattice parameter of NMO and NCO spheres and NCO flakes, as well as the developments of their respective unit cell volumes, can be seen in Figure S3. In Figure S4 depicts the relaxation behaviour as measured by galvanostatic intermittent titration technique (GITT) for NMO flakes. Table S3 shows the development of resistivity for NMO and NCO flakes.

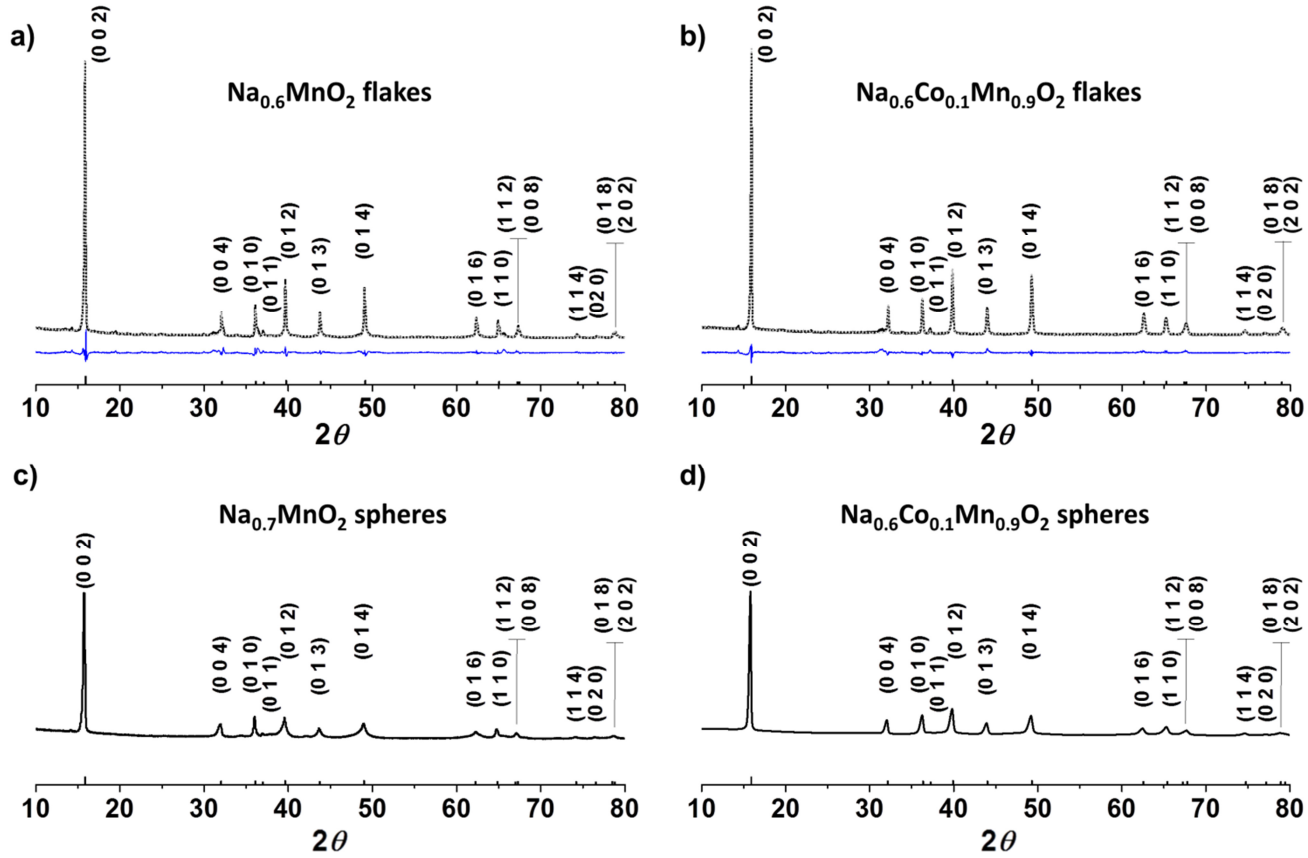

Figure S1. X-ray diffraction pattern and (hkl) positions (bottom) of a) $Na_{0.6}MnO_2$ flakes, b) $Na_{0.6}Co_{0.1}Mn_{0.9}O_2$ flakes, c) $Na_{0.7}MnO_2$ spheres, d) $Na_{0.6}Co_{0.1}Mn_{0.9}O_2$ spheres; for a) & b): dotted line: fit using Rietveld refinement, blue line: difference between pattern and fit (K_α (Cu): λ = 1.54 Å)

a) NCO flakes

Element	x	y	z	Occupancy
Mn	0	0	0	1
Co	0	0	0	
Na(1)	0	0	1/4	0.262(4)
Na(2)	2/3	1/3	1/4	0.396(9)
O	1/3	2/3	0.0903(4)	1

a/b = 2.8621(14) Å, c = 11.094(60) Å
R_{wp} :5.36%, R_p: 3.85%, S: 2.2062

b) NMO flakes

Element	x	y	z	Occupancy
Mn	0	0	0	1
Na(1)	0	0	1/4	0.231(17)
Na(2)	2/3	1/3	1/4	0.38(2)
O	1/3	2/3	0.0857(6)	1

a/b = 2.869(7) Å, c = 11.12(4) Å
R_{wp} : 9.19%, R_p: 6.38%, S: 3.2145

NCO spheres

a/b = 2.861(4) Å, c = 11.123(15) Å

NMO spheres

a/b = 2.875(14) Å, c = 11.16(6) Å

Table S1. a) Rietveld refinement parameters for NCO flakes and lattice parameters for NCO spheres (Pawley fit), b) Rietveld refinement parameters for NMO flakes and lattice parameters for NMO spheres (Pawley fit).

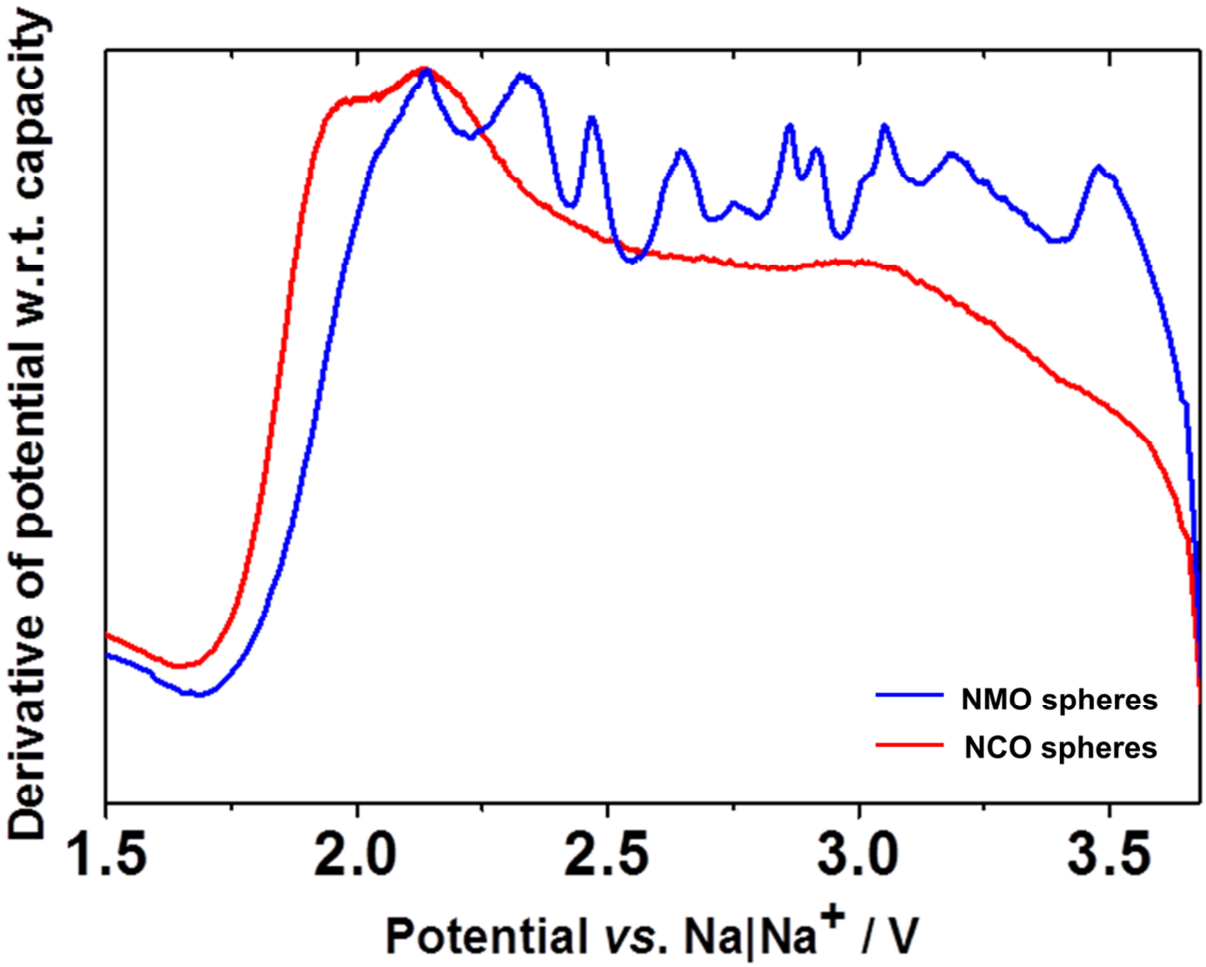

Figure S2. Derivative of the potential with respect to capacity: $Na_{0.7}MnO_2$ and $Na_{0.6}Co_{0.1}Mn_{0.9}O_2$ spheres.

a)

NCO Flakes	(002)		(004)		
x(Na)	FWHM / 2θ	peak position / 2θ	FWHM / 2θ	peak position / 2θ	$FWHM_{(004)}$ / $FWHM_{(002)}$
0.49	0.162	10.02	0.191	20.13	1.18
0.60	0.163	10.05	0.167	20.18	1.02
0.70	0.150	10.10	0.157	20.28	1.05
0.85	0.137	10.12	0.134	20.32	0.98
1.00	0.146	10.13	0.129	20.33	0.89

b)

NCO Spheres	(002)		(004)		
x(Na)	FWHM / 2θ	peak position / 2θ	FWHM / 2θ	peak position / 2θ	$FWHM_{(004)}$ / $FWHM_{(002)}$
0.43	0.160	10.02	0.222	20.10	1.39
0.50	0.201	10.00	0.200	20.14	1.00
0.60	0.174	10.03	0.181	20.18	1.04
0.85	0.146	10.08	0.196	20.22	1.35
0.85	0.140	10.11	0.169	20.29	1.21
1.00	0.151	10.13	0.184	20.32	1.22
1.05	0.160	10.13	0.200	20.33	1.25

Table S2. FWHM for the (002) and (004) reflections as well as their respective quotients at various points during discharge for a) NCO flakes, and b) NCO spheres

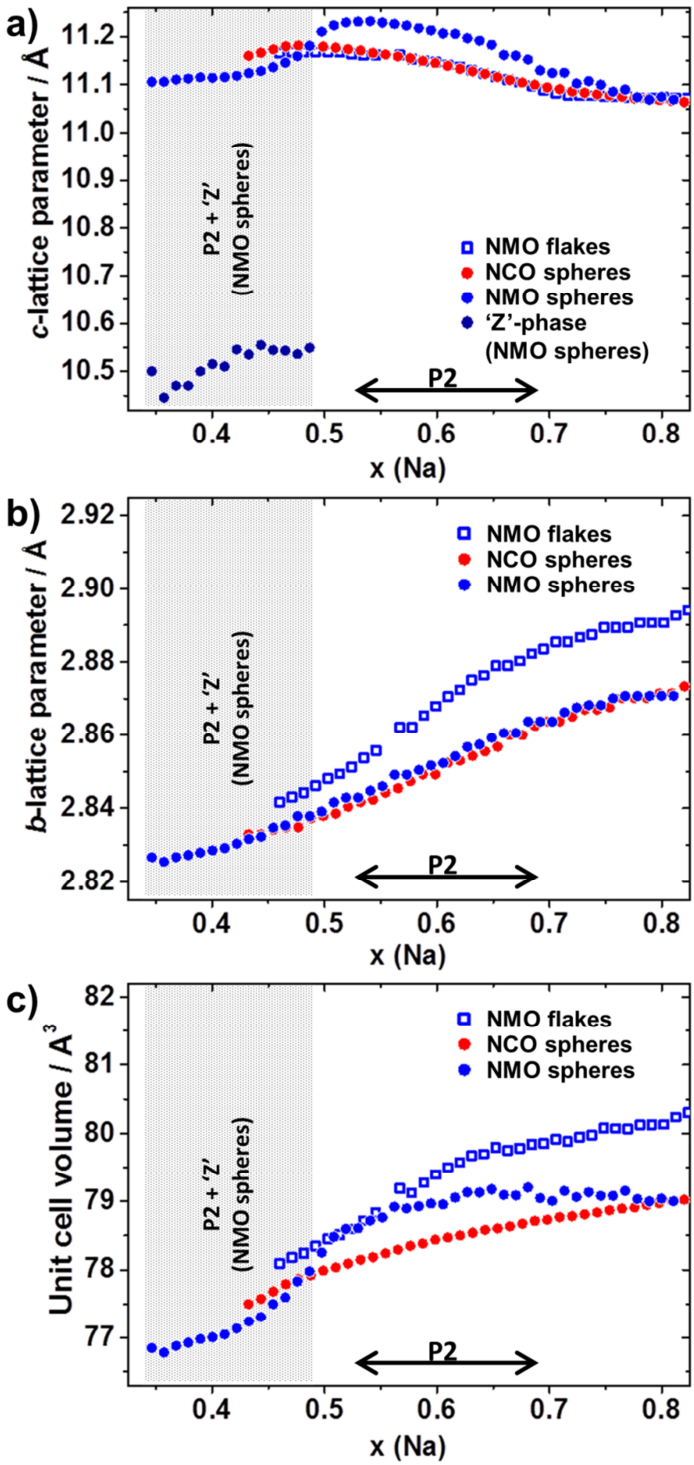

Figure S3. Development of the a) c-lattice parameter (including the evolving 'Z' phase) a) b-lattice parameter, c) unit cell volume, for NMO-, NCO spheres and NCO flakes. The two phase region for NMO spheres is indicated. Values are displayed until the phase change for NMO spheres occurs (Na ~ 0.82).

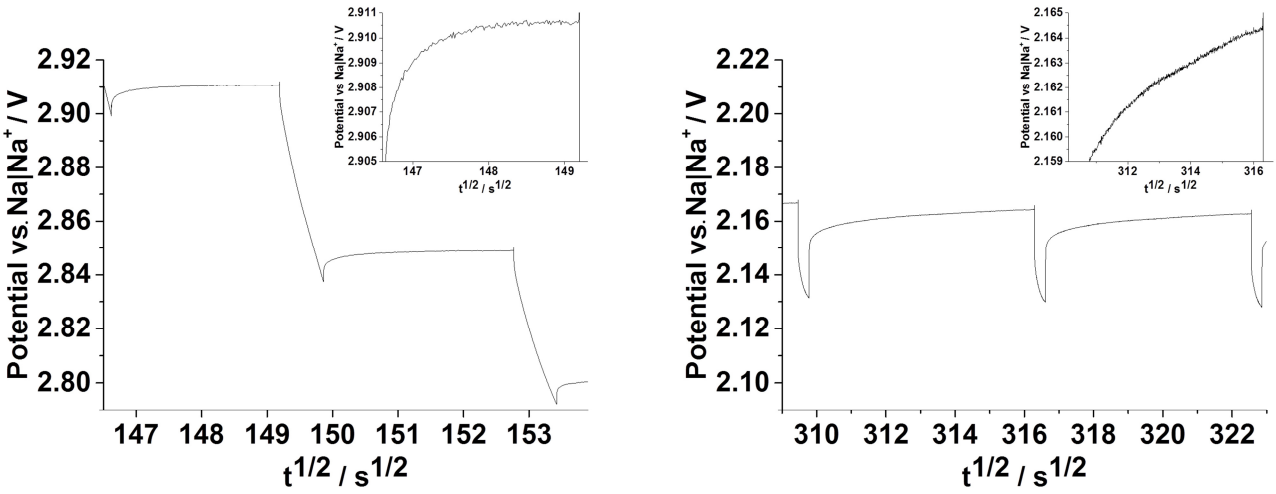

Figure S4. Relaxation behavior of $Na_{0.7}MnO_2$ flakes at various points on the discharge curve.

Randles circuit

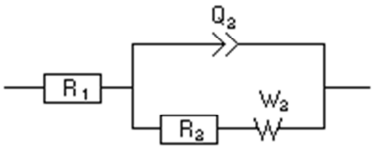

NMO flakes

U/V	U_{relax}/V	R1	R2	%
2.90	2.85	43.64	105.00	100
3.80	3.44	44.75	348.80	332
3.25	3.29	48.10	220.50	210
2.70	2.78	47.48	63.23	60
2.50	2.63	48.91	93.70	89
2.40	2.54	50.56	187.80	179
2.33	2.40	51.16	268.40	256
2.10	2.17	53.83	2755.00	2624
1.50	2.08	59.57	23703.00	22574

NCO flakes

U/V	U_{relax}/V	R1	R2	%
2.90	2.83	84.29	17.89	100
3.80	3.31	83.43	43.80	245
3.25	3.19	84.12	29.51	165
2.70	2.75	84.16	15.67	88
2.50	2.57	83.51	15.45	86
2.40	2.45	84.61	16.39	92
2.33	2.37	83.09	17.40	97
2.10	2.12	85.80	43.54	243
1.50	1.92	90.05	1183.00	6613

Table S3: Resistivity for NMO flakes and NCO flakes and various potentials during discharge; R1: Ohmic resistance of all cell components (mainly electrolyte – as the cell geometry was not kept constant, the value varies significantly comparing NMO and NCO flakes); R2: charge transfer resistance (changes in R2 are indicative of changes of the conductivity of the active material. The nominal values have been normalized to 100% to enable the comparison of the trends of different cells).

4.5 A Novel Ionic Liquid for Li-Ion Batteries – Uniting the Advantages of Guanidinium and Piperidinium Cations

This chapter is a summary of the publication "A novel ionic liquid for Li ion batteries – uniting the advantages of guanidinium and piperidinium cations" (RSC Advances **2014**, *4*, 1996-2003). It describes the development of a new ionic liquid (IL) as electrolyte for lithium- and sodium-ion batteries. This work was jointly performed by N. Bucher, S. Hartung and M. Arkhipova. N. Bucher was leading the electrochemical characterisation and battery testing. S. Hartung focused on the physicochemical characterization and drafted the manuscript. M. Arkhipova synthesised and identified the IL.

Electrolytes in sodium-ion and current commercial lithium-ion batteries typically consist of organic solvents solutions based on organic carbonates. These molecules, *e.g.* propylene carbonate or dimethyl carbonate, have a considerable vapour pressure, which poses a safety risk as it is the cause of flammability. Moreover, the electrochemical window of these carbonates limits the operating potential of lithium-ion batteries, and renders the quest for high voltage cathode materials useless. In general, it is desirable to eliminate parasitic side reactions occurring in LIBs and NIBs, and thus improve cycle live, by employing new types of stable electrolytes. Therefore, novel, safer electrolytes which extend the possible voltage window of batteries are needed. A promising candidate is ionic liquids, due to their negligible vapour pressure and (potentially) high electrochemical stability. However, these characteristics vary between structural classes. The scope of this work was to combine the advantages of different structural elements by incorporating them into one structure. Following this reasoning, the piperidinium structure was selected due to its high thermal and (particularly cathodic) electrochemical stability.[132–134] The guanidinium structure was selected due to the low viscosity of guanidinium-based ILs.[135–137] The resulting IL, *N,N,N',N'*-tetramethyl-*N'',N''*-pentamethylene-guanidinium bis(trifluoromethylsulfonyl) imide (PipGuan-TFSI), contained structural elements from both group, with TFSI as the anion.

Detailed physico-chemical investigations of the pure, targeted material, PipGuan-TFSI, confirmed that key properties lay between the respective values of the parent structures. This applies for thermal stability (415 °C), viscosity (108 mPa s at 25 °C), conductivity (1.46 mS cm^{-1} @ 28 °C) as well as for electrochemical stability measured

in a two and three electrode setup (~4.4 V). The ability of an electrolyte consisting of a 1M solution of LiTFSI in PipGuan-TFSI to transport Li-ions, which is a prerequisite for a working LIB, has been demonstrated by cyclic voltammetry of a two electrode coin cell with metallic lithium and stainless steel as the electrodes; reversible oxidation and reduction of Li and Li^+ was clearly visible.

Moreover, formation of a solid electrolyte interphase (SEI), which is a protective layer on the electrode formed by decomposition products of the electrolyte, and concurrently stability *vs*. metallic lithium was confirmed using EIS.

In order to investigate the behaviour of this new electrolyte in a Li-ion half-cell, coin cells with $LiFePO_4$ as cathode, and Li-metal as anode material were constructed. While obtained capacities were comparable to those achieved with conventional electrolytes at very slow C-rates (154 mA h g^{-1} at 0.025C), they decline when C-rates are increased. However, it was shown that elevated temperatures (55 °C) have a positive influence on rate capability, as expected, and resulted in a capacity of 148 mA h g^{-1} for 0.2C. In contrast to the aforementioned physico-chemical properties of PipGuan-TFSI, which lay between the two parent structures, discharge capacities for $LiFePO_4$ exceed both.[134,137]

In summary, a novel ionic liquid has been presented, combining positive characteristics of the parental structures. Its suitability as LIB electrolyte has been demonstrated.

After proving the suitability of this type of electrolyte in an LIB system, PipGuan-TFSI was tested for the Na_xMnO_{2+z} and $Na_xCo_{0.1}Mn_{0.9}O_{2+z}$ spheres (materials depict under Chapter 4.2 & 4.4) in an attempt to increase cycling stability. However, initial results indicated that this electrolyte is not stable in these systems.

A novel ionic liquid for Li ion batteries – uniting the advantages of guanidinium and piperidinium cations

Nicolas Bucher, Steffen Hartung, Maria Arkhipova, Denis Yu, Philipp Kratzer, Gerhard Maas, Madhavi Srinivasan, Harry E. Hoster

Reproduced from RSC Advances, Volume 4, Issue 4, 2014, Pages 1996-2003 with permission from The Royal Society of Chemistry.

The publication can be found under the following weblink:

http://dx.doi.org/10.1039/C3RA46118A

RSC Advances

PAPER

View Article Online
View Journal | View Issue

Cite this: *RSC Adv.*, 2014, **4**, 1996

A novel ionic liquid for Li ion batteries – uniting the advantages of guanidinium and piperidinium cations

Nicolas Bucher,†[ab] Steffen Hartung,†[ab] Maria Arkhipova,†[e] Denis Yu,[ad] Philipp Kratzer,[e] Gerhard Maas,[e] Madhavi Srinivasan[ac] and Harry E. Hoster*[abd]

Received 31st July 2013
Accepted 5th November 2013

DOI: 10.1039/c3ra46118a

www.rsc.org/advances

We report on the synthesis and the properties of *N*,*N*,*N*′,*N*′-tetramethyl-*N*″,*N*″-pentamethyleneguanidinium bis(trifluoromethylsulfonyl)imide (PipGuan-TFSI). The cation of this novel ionic liquid combines guanidinium and piperidinium structural elements. We tested it for its viscosity, ion conductivity, and also for its thermal and electrochemical stability. Furthermore, a 0.5 M solution of lithium TFSI in PipGuan-TFSI was tested as an electrolyte for Li-ion batteries. These experiments included cycles of Li deposition/dissolution on stainless steel and (de)intercalation into/from $LiFePO_4$ electrodes. The tests involving $LiFePO_4$ cathodes were performed at various *C*-rates and temperatures for a better quantitative comparison to other electrolyte systems. We discuss in how far PipGuan-TFSI successfully combines the advantages of guanidinium and piperidinium ionic liquids for battery electrolyte applications.

Introduction

Ionic liquids (ILs) are salts with a melting point below 100 °C. Room temperature ionic liquids, which is a subgroup defined by a melting point below room temperature, have attracted great interest in recent years as tunable "designer solvents". ILs are electrochemically and thermally stable, have a negligible volatility, and thus a low flammability.[1,2] Those properties make them suitable not only for (sustainable) chemical synthesis[3] or carbon capture[4,5] but also for energy storage applications[6] such as super capacitors, batteries, fuel cells and solar cells.[2,7–12] The gain in safety due to the low volatility of ILs comes with a higher viscosity and concomitantly lower ion conductivity[13] as compared to traditional, molecular solvents. Furthermore, any IL to be used in electrochemical energy storage devices must exhibit a suitable stability window. Both the ion conductivity and the potential window are tackled by the design of new ionic liquids.[14–16]

IL based electrolytes in Li ion batteries (LIBs) are usually ternary mixtures containing Li^+ ions and the anions and cations of the respective IL. The Li salt and the IL thus share the same anion. Therefore, the IL cation becomes the subject of target oriented optimization. Common basic structures are pyridinium,[17] imidazolium,[18–21] ammonium,[20–23] sulfonium, pyrrolidinium,[20,21,24–26] guanidinium,[27–33] or piperidinium.[19–21,34,35] The infinite number of possible structural variations in combination with the substantial synthesis efforts calls for a systematic strategy. Parallel to computational studies that are on the way in many research groups,[14–16] there is an obvious demand for systematic synthesis variations in combination with a set of electrochemical benchmark tests. For substances whose properties are already close to the desired optimum, variations can be incremental, *e.g.*, modifying moieties of existing cation structures. For substances with more room for improvement, however, more substantial yet still systematic variations may speed up the progress – in analogy to Nature's principles of genetic crossing that was successfully transferred to the field of multi-parameter optimization problems.

In this paper, we will demonstrate how the advantages of two different structural elements can be combined towards a new cation with better key properties than the parent structures. The two original structural elements are guanidinium and piperidinium. Guanidinium cations can be modified at six different sides and the resulting ILs have low viscosities. The main drawback of guanidinium cations, however, is their lack of electrochemical stability at the negative potential limit.[23,27,29,30] Piperidinium based ILs, on the other hand, were reported to have electrochemical windows exceeding 5 V and high cathodic stability *versus* lithium metal. Moreover, piperidinium ILs have a high thermal stability, which is crucial with regard to safety.[34,36] In the first part of this paper we will describe the

[a]*TUM CREATE, Singapore 138602, Singapore. E-mail: harry.hoster@tum-create.edu.sg; Tel: +65 9455 3973*

[b]*Technische Universität München, 85748 Garching, Germany*

[c]*School of Materials Science and Engineering, Nanyang Technological University, Singapore 639798, Singapore*

[d]*Energy Research Institute @ NTU, 1 CleanTech Loop, #06-04 CleanTech One, Singapore 637141, Singapore*

[e]*Institute of Organic Chemistry I, University of Ulm, Albert-Einstein-Allee 11, 89081 Ulm, Germany*

† Authors contributed equally to this manuscript.

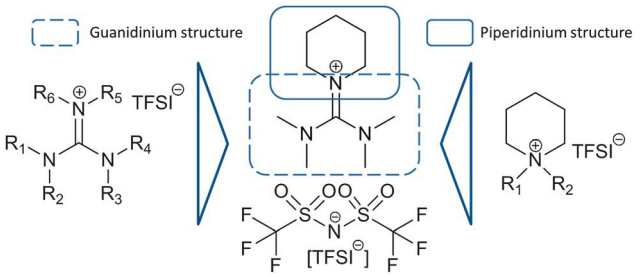

Fig. 1 *N,N,N′,N′*-Tetramethyl-*N″,N″*-pentamethyleneguanidinium bis(trifluoromethylsulfonyl)imide (PipGuan-TFSI).

synthesis of a new cation in which one side arm of a guanidinium cation was substituted with a piperidinium ring (PipGuan, see Fig. 1). Being initially synthesised as PipGuan chloride, an anion exchange towards PipGuan bis(trifluoromethylsulfonyl) imide (TFSI) yields a new IL, PipGuan-TFSI.

We will then elucidate the physical and electrochemical properties of this IL. Those characterisations include nuclear magnetic resonance (NMR) and infrared (IR) spectrometry, thermogravimetric analysis supported by mass spectroscopy (TGA-MS), differential scanning calorimetry (DSC), and viscosity and conductivity measurements. The electrochemical properties were tested by cyclic voltammetry (CV) and electrochemical impedance spectroscopy (EIS). Finally, we tested a solution of LiTFSI in PipGuan-TFSI as an electrolyte for a $LiFePO_4$ battery half-cell and compared the results at two different temperatures to the behaviour of the same cell using a commercial electrolyte. We will discuss in which respect the properties of the new cation structure reflect a compromise between the two parent structures and where the product of the crossing is superior to either of them.

Materials and methods

Synthesis

The novel guanidinium-based ionic liquid *N,N,N′,N′*-tetramethyl-*N″,N″*-pentamethyleneguanidinium bis(trifluoromethylsulfonyl) imide was synthesised from tetramethylurea by partially modifying reported procedures (Fig. 2).[28,31] Rigorously dried organic solvents were used. All amines were dried with KOH pellets and stored under an argon atmosphere. ^{1}H NMR spectra were referenced to the residual proton signal of the solvent [$\delta(CDCl_3)$ = 7.26 ppm]. ^{13}C spectra were referenced to the solvent signal [$\delta(CDCl_3)$ = 77.00 ppm], and ^{19}F spectra to external C_6F_6 [$\delta(C_6F_6)$ = −162.9 ppm].

As a first step, *N,N,N′,N′*-tetramethylchloroformamidinium chloride was obtained by a dropwise addition of tetramethylurea (20 mL, 167 mmol) to freshly distilled oxalyl chloride (15.7 mL, 183 mmol) dissolved in 20 mL of dry dichloromethane at room temperature. The solution was stirred overnight and the solvent was removed under vacuum. The remaining precipitate was washed several times with dry diethyl ether until the washing ether was colourless. The solid *N,N,N′,N′*-tetramethylchloroformamidinium chloride was dried for three hours at 20 °C/0.05 mbar to yield 27.09 g (95%) as a white moisture sensitive powder.

N,N,N′,N′-Tetramethyl-*N″,N″*-pentamethyleneguanidinium chloride was prepared by dropwise addition of a solution of piperidine (2.5 mL, 25 mmol) and triethylamine (3.5 mL, 25 mmol) in 20 mL of dry diethyl ether to a solution of *N,N,N′,N′*-tetramethylchloroformamidinium chloride (4.3 g, 25 mmol) in 40 mL of dry acetonitrile at 0 °C. The mixture was stirred overnight at room temperature. The precipitated triethylammonium chloride was filtered off, and the solvents were distilled on the rotary evaporator. A 0.1 M NaOH solution was added to the residual oil, until the pH was slightly alkaline. To remove the coloured impurities, the aqueous solution was washed several times with diethyl ether. Volatile components were distilled on the rotary evaporator (40 °C/70 mbar) and the solid residue was subsequently dried at 50 °C/0.05 mbar. Afterwards, it was dissolved in dry acetonitrile/diethyl ether (2 : 1 *v*/*v*, 10 mL) and the solid was filtered off. The organic solvents were removed and the product was dried for 8 h at 80 °C/0.05 mbar. Crystallisation from ethyl acetate/dimethyl formamide (2 : 1) gave 4.2 g of *N,N,N′,N′*-tetramethyl-*N″,N″*-pentamethyleneguanidinium chloride (77% yield) as a white hygroscopic powder.

N,N,N′,N′-Tetramethyl-*N″,N″*-pentamethyleneguanidinium bis(trifluoromethylsulfonyl)imide (PipGuan-TFSI) was synthesised by anion exchange. Lithium bis(trifluoromethylsulfonyl)imide (2.9 g, 10 mmol) and *N,N,N′,N′*-tetramethyl-*N″,N″*-pentamethyleneguanidinium chloride (2.2 g, 10 mmol) were dissolved in 30 and 10 mL, respectively, of deionised water. The solutions were combined resulting in two phases. After stirring the mixture at 70 °C for 30 min, it was cooled to room temperature, and dichloromethane (30 mL) was added. The organic phase was separated and washed with several portions of deionised water until chloride could not be detected any more in the rinsing water using $AgNO_3$. The organic phase was

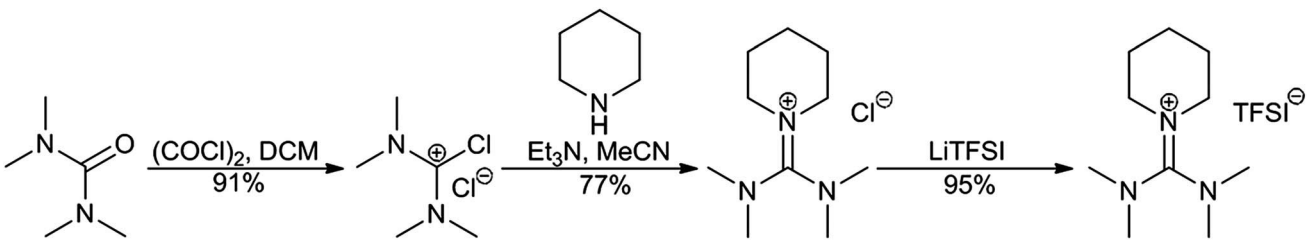

Fig. 2 Synthesis route to PipGuan-TFSI.

dried with Na_2SO_4, stirred over charcoal for 15 min, and filtered. The solvent was removed on a rotary evaporator, and the product was dried for 8 h at 120 °C/0.05 mbar. *N*,*N*,*N*′,*N*′-Tetramethyl-*N*″,*N*″-pentamethyleneguanidinium bis(trifluoromethylsulfonyl) imide was obtained as a slightly yellowish oil (4.4 g, 95% yield).

Physical and electrochemical characterisation

NMR spectra were recorded on a Bruker DRX 400 spectrometer (^{1}H: 400.13 MHz; ^{13}C: 100.61 MHz; ^{19}F: 376.46 MHz). IR spectra were recorded with a Bruker Vector 22 FTIR spectrometer. Thermal stability was determined by TGA (Mettler Toledo STARe TGA/DSC1; Mettler-Toledo TGA/SDTA 851 for *N*,*N*,*N*′,*N*′-tetramethyl-*N*″,*N*″-pentamethyleneguanidinium chloride), the decomposition point was defined as $T_{dec} \triangleq$ temperature of highest decomposition gradient at a heating rate of 5 K min^{-1}. The decomposition products were detected by mass spectrometry (Pfeiffer Vacuum Thermostar GSD320). Differential scanning calorimetry was performed with a Perkin Elmer DSC 7 instrument. Microanalyses were obtained with an Elementar vario MICRO cube instrument. Lithium bis(trifluoromethylsulfonyl)imide for synthesis was received from Acros Organics or IoLiTec GmbH with a purity of 99%. Viscosity was measured using a Rheometer (Anton Paar GmbH, Rheometer MCR 501), conductivity was measured using a conductivity meter (Eutech Instruments, CyberScan 600 Series). The electrochemical window was measured by linear sweep voltammetry (scan rate: 10 mV s^{-1}) in two different cells: (i) a two-electrode 2016 coin cell with stainless steel as the working electrode and lithium as the counter and reference electrode and (ii) a three-electrode beaker cell with glassy carbon as the working, Ag|$AgNO_3$ as the reference, and platinum as the counter electrode. For the reference electrode, a Ag wire was immersed in a solution of 0.01 M $AgNO_3$ in acetonitrile, with 0.1 M N(octyl)$_4BF_4$ as conducting salt. A junction with the compartment containing the IL was realized with a vycor glass frit. For both set-ups, the electrochemical windows were calculated for the cut-off current densities 0.1 mA cm^{-2} and 0.5 mA cm^{-2}. EIS was performed in a symmetric lithium coin cell set-up (Li|electrolyte|Li). Plating/stripping experiments were conducted using a 2016 coin cell set-up with lithium metal and stainless steel electrodes. For both measurements, a Biologic VMP3 potentiostat was used. Battery tests were performed with an electrolyte consisting of the synthesised PipGuan-TFSI and 0.5 M lithium bis(trifluoromethylsulfonyl)imide (LiTFSI, SOLVAY, 99.99%). Note that the maximum concentration attainable at 300 K was 0.8 M. Commercial lithium iron phosphate (LFP, ENAX) was used as cathode material. The composite cathodes were prepared by mixing LFP, acetylene black (Alfa Aesar, > 99%), and polyvinylidene fluoride (PVdF, Arkema, Kynar HSV 900) binder in the weight ratio of 80 : 10 : 10, with *N*-methyl-2-pyrrolidone (NMP, Sigma Aldrich, ≥99%), to form a slurry. The well-mixed, homogenous mixture was coated on an Al foil using a doctor blade, and dried at 80 °C in air to remove the solvent. Circular pieces with 16 mm diameter were punched out of the coated Al foil and roll-pressed between twin rollers to improve adherence of the coating to the Al foil. After drying the electrodes for 4 h under vacuum at 110 °C, the electrodes were assembled in a half-cell configuration in 2016 coin cells, using 16 mm circular lithium metal pieces as the anode, separated by a glass fibre separator (Whatman) swollen with the aforementioned electrolyte. Charge/discharge experiments were carried out with an Arbin battery tester. All measurements were performed with the purified and dry ionic liquid. Magnetic resonance techniques (^{1}H-NMR, ^{13}C-NMR, ^{19}F-NMR), infrared spectroscopy, mass spectroscopy, Karl-Fischer analysis and elemental analysis did not indicate the presence of any impurities other than small traces of water (according to Karl-Fischer: <50 ppm).

Results and discussion

Analytical data

***N*,*N*,*N*′,*N*′-Tetramethylchloroformamidinium chloride.** ^{1}H NMR ($CDCl_3$): $\delta = 3.55$ (s, 12H, NCH_3) ppm.

***N*,*N*,*N*′,*N*′-Tetramethyl-*N*″,*N*″-pentamethyleneguanidinium chloride.** Melting point = 158–159 °C, T_{dec} = 330 °C, ^{1}H NMR ($CDCl_3$): δ = 1.25–1.50 (m, 6H, $CH_2(CH_2)_3CH_2$, pip), 2.77 (s, 12H, NCH_3), 2.97–3.13 (m, 4H, NCH_2, pip) ppm. ^{13}C NMR ($CDCl_3$): δ = 22.6 ($N(CH_2)_2CH_2$, pip), 24.5 ($NCH_2CH_2CH_2$, pip), 40.05 and 40.09 (N*C*H$_3$), 49.3 (N*C*H$_2$CH$_2$CH$_2$, pip), 161.9 (*C*N$_3$) ppm. IR (ATR): ν = 2930 (m), 2856 (m), 1564 (s), 1435 (m), 1407 (s), 1277 (m), 1253 (m) cm^{-1}. MS (CI): m/z = 184 (100%, [cation]$^+$). Anal. calcd. for $C_{10}H_{22}ClN_3$*0.75H_2O: C 51.49, H 10.15, N 18.01; found: C 51.48, H 10.27, N 17.94%.

***N*,*N*,*N*′,*N*′-Tetramethyl-*N*″,*N*″-pentamethyleneguanidinium bis(trifluoromethylsulfonyl)imide (PipGuan-TFSI).** Melting point = 3 °C, T_{dec} = 463 °C, ^{1}H NMR ($CDCl_3$): δ = 1.65–1.80 (m, 6H, $CH_2(CH_2)_3CH_2$, pip), 2.98 and 2.99 (2 s, 6H each, NCH_3), 3.20–3.35 (m, 4H, NCH_2, pip) ppm. ^{13}C NMR ($CDCl_3$): δ = 23.4 ($N(CH_2)_2CH_2$, pip), 25.1 ($NCH_2CH_2CH_2$, pip), 40.32 and 40.35 (N*C*H$_3$), 49.9 (N*C*H$_2$CH$_2$CH$_2$, pip), 162.8 (*C*N$_3$) ppm. ^{19}F NMR ($CDCl_3$): δ = −75.3 ppm. IR (NaCl): ν = 2951 (m), 2864 (m), 1569 (s), 1411 (m), 1347 (s), 1330 (s), 1176 (s), 1134 (s), 1053 (s) cm^{-1}. MS (CI): m/z = 184 (100%, [cation]$^+$). Anal. calcd. for $C_{12}H_{22}F_6N_4O_4S_2$ (464.44): C 31.03, H 4.77, N 12.06; found: C 31.03, H 4.68, N 12.25%.

Thermal properties of PipGuan-TFSI

DSC revealed a melting point of 3 °C as measured by DSC. It is lower than the one of *N*,*N*-diethyl-*N*′,*N*′,*N*″,*N*″-tetramethyl – or *N*,*N*,*N*′,*N*′-tetramethyl-*N*″,*N*″-dipropylguanidinium-TFSI (9.9 and 12.9 °C, respectively) but slightly higher than the one of *N*,*N*,*N*′,*N*′-tetramethyl-*N*″-ethyl-*N*″-propylguanidinium-TFSI (−1.6 °C).[29,30] In general, the melting point of ionic liquids increases for more symmetrical cations, because symmetry facilitates a closer packing of the ions. Leaving the methyl groups at *N* and *N*′ constant, the melting point tends to decrease with increasing chain length of the alkyl chain at *N*″, up to a critical molar mass.[30] Considering that the piperidinium contains five carbon atoms, the relative position of the melting point of PipGuan-TFSI is within the expected range.

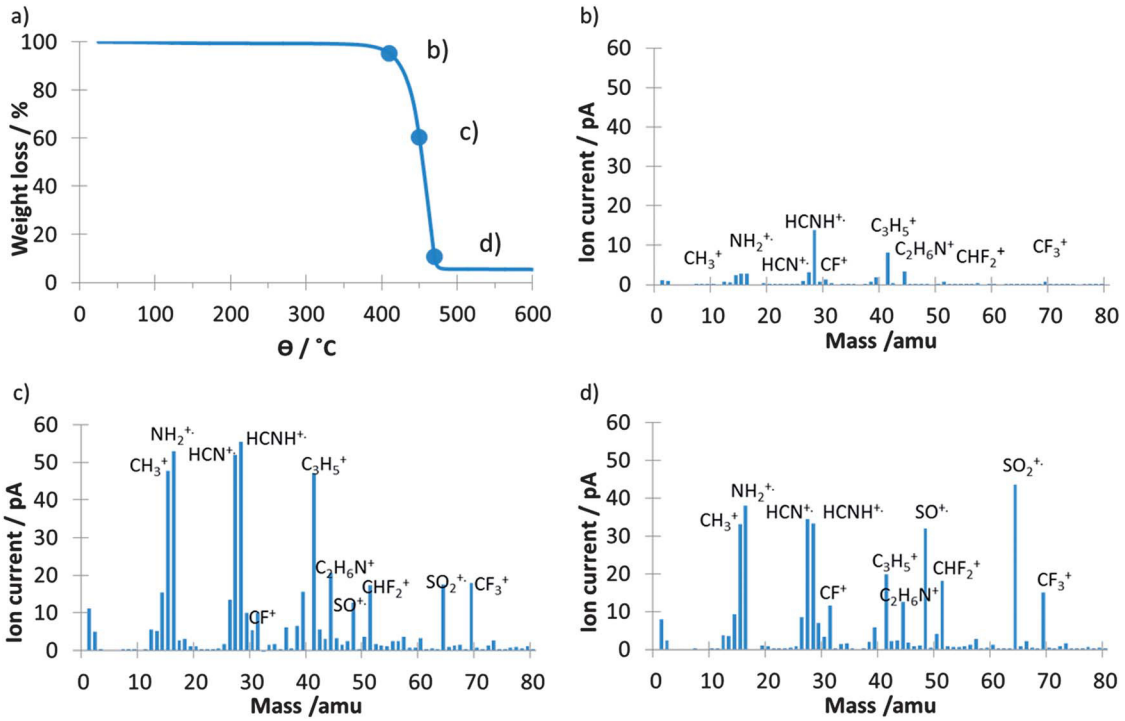

Fig. 3 (a) TGA of PipGuan-TFSI (5 K min^{-1}), (b) MS of PipGuan-TFSI at 410 °C, (c) MS of PipGuan-TFSI at 450 °C, (d) MS of PipGuan-TFSI at 470 °C.

TGA showed that PipGuan-TFSI is stable up to 415 °C (5% of mass loss). The temperature of highest decomposition gradient is at 463 °C. The mass spectra of the decomposition products were analysed at the onset, in the middle, and at the end of the decomposition (Fig. 3). In the beginning, the fragments seem to indicate the decomposition mainly of the cation (Fig. 3a), whereas at the end, the fragments are predominantly decomposition products of the anion (Fig. 3b). In the middle of decomposition, fragments from both cation and anion are present (Fig. 3c). Thus, it can be assumed that the cation is the limiting ion for thermal stability. Comparing this data with other ILs, PipGuan-TFSI is thermally more stable than other guanidinium ILs, but less stable than piperidinium based ILs.[30,34]

Viscosity and conductivity

Viscosities and conductivities were measured for pure PipGuan-TFSI and for a solution of 0.5 M LiTFSI, a potential LIB electrolyte. As found in similar systems,[9,27] the viscosity of the Li^+ containing solution is higher than that of the pure IL for all temperatures. For both samples, the viscosity decreases with increasing temperature (Fig. 4) according to a Vogel–Tammann–Fulcher relationship (eqn (1));[37,38] for the fitted parameters see Table 1.

$$\eta = \eta_0 \exp\left(\frac{B}{T - T_0}\right) \quad (1)$$

The values are comparable to those reported for hexaalkyl guanidinium-based ionic liquids with TFSI as the anion.[30]

Room temperature viscosities of previously reported hexaalkyl guanidinium[30] and piperidinium[34] based ILs are in the range of 58–113 mPa s and 190–370 mPa s, respectively. For PipGuan-TFSI, our measurements reveal 108 mPa s at 25 °C. As expected, this value lies between those for guanidinium and piperidinium. The viscosity of the 0.5 M LiTFSI electrolyte was found to be 164 mPa s at room temperature.

Conductivities were measured in an Ar filled glovebox at 28 °C. The measurements revealed 1.46 mS cm^{-1} and 0.74 mS cm^{-1} for pure PipGuan TFSI and the 0.5 M LiTFSI electrolyte, respectively. Again, the conductivity of the pure IL lies between the value ranges reported for *N*,*N*,*N*′,*N*′-tetramethyl-*N*″-alkyl^1-*N*″-alkyl^2 guanidinium-TFSI (alkyl$^{1/2}$ = methyl, ethyl, propyl and butyl), *i.e.*, 1.02–2.86 mS cm^{-1} (at 25 °C),[30] and for *N*-alkyl^1-*N*-alkyl^{2}piperidinium-TFSI (alkyl$^{1/2}$ = methyl, ethyl, propyl, butyl, pentyl, hexyl, or heptyl), which are $2.1 \cdot 10^{-5}$–0.92 mS cm^{-1} (at 20 °C),[34] respectively.

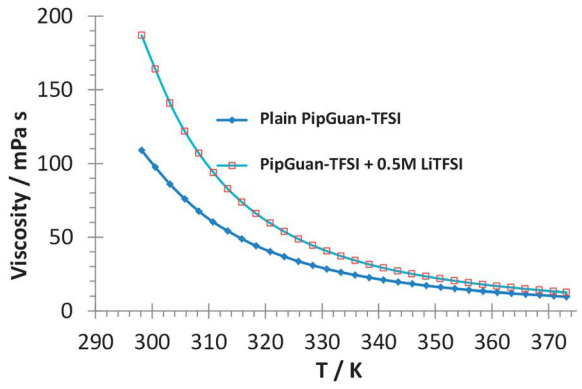

Fig. 4 Temperature dependence of viscosity for PipGuan-TFSI and 0.5 M solution of LiTFSI in PipGuan-TFSI.

Table 1 Parameters for the Vogel–Tammann–Fulcher equation for PipGuan-TFSI and the electrolyte (0.5 M solution of LiTFSI in PipGuan-TFSI)

	η_0/mPa s	B/K	T_0/K	R^2
PipGuan-TFSI	0.26 ± 7%	705 ± 2%	190 ± 1%	>0.9999
Electrolyte	0.17 ± 9%	797 ± 3%	174 ± 1%	>0.9999

Electrochemical measurements

Fig. 5a and b show the electrochemical window of PipGuan-TFSI measured in two different ways. Fig. 5a was measured with a three-electrode set-up, with glassy-carbon as the working, $Ag|AgNO_3$ as the reference, and platinum as the counter electrode. The three-electrode set-up shows an electrochemical window of 4.40 V between −2.55 V and 1.85 V *vs.* $Ag|Ag^+$, all for a cut-off current density of 0.5 mA cm^{-2}. For a cut-off at 0.1 mA cm^{-2}, the window narrows to 4.16 V with −2.50 V and 1.66 V *vs.* $Ag|Ag^+$ as cathodic and anodic limits, respectively (see Table 2). Fig. 5b shows the measurement in a coin cell to simulate working conditions in a LIB. The two-electrode set-up with stainless steel as a working and Li metal as a counter electrode showed an electrochemical window of 5.11 V (0.2 V … 5.31 V) for a cut-off current density of 0.5 mA cm^{-2}, and of 4.44 V (0.44 V… 4.88 V) for a cut-off at 0.1 mA cm^{-2}.

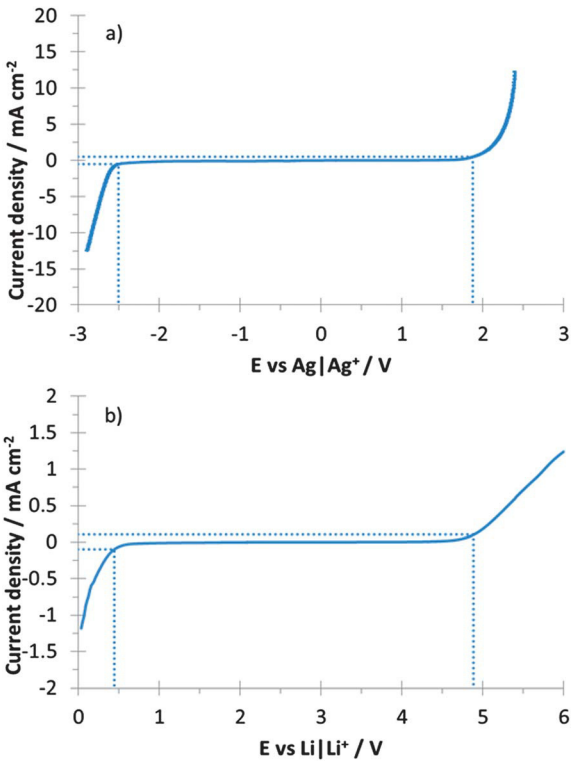

Fig. 5 (a) Electrochemical window of PipGuan-TFSI using a 3-electrode set-up with $Ag|AgNO_3$ as reference, glassy carbon as working and Pt as counter electrode, (b) electrochemical window of PipGuan-TFSI using a coin cell set-up with Li as combined counter&reference and stainless steel as a working electrode; the dotted lines represent a cut-off current density of 0.5 mA cm^{-2} for (a), and 0.1 mA cm^{-2} for (b).

Table 2 Electrochemical stability limits and electrochemical window for PipGuan-TFSI

	2 Electrodes, *vs.* $Li|Li^+$		3 Electrodes, *vs.* $Ag|Ag^+$	
Cut-off current density/mA cm^{-2}	0.1	0.5	0.1	0.5
Anodic limit/V	4.88	5.31	1.66	1.85
Cathodic limit/V	0.44	0.20	−2.50	−2.55
Electrochem. window/V	4.44	5.11	4.16	4.40

It should be pointed out that the Li reference potential obtained in these cells is not well-defined because there is no controlled Li^+ content in the Li-TFSI solution as required for a true $Li|Li^+$ system.[39] Nevertheless, the upper potential limit indicates that PipGuan-TFSI could be suitable for high-voltage battery cells.

For an application of PipGuan-TFSI in Li-ion batteries the electrochemical properties of the Li^+ containing electrolyte (PipGuan-TFSI + 0.5 M LiTFSI) are more important than those of the plain IL. Fig. 6 shows the first and second cycle of a freshly mounted coin cell with stainless steel as working and lithium as combined counter&reference electrode, respectively. Starting at 2 V, the first CV cycle shows broad cathodic features starting at 1.5 V in the negative going scan. Those presumably reflect electrolyte decomposition, in analogy to previous observations for other ILs.[24,27,40,41]

The fact that these features are only observed in the first negative going scan indicates that the product is a passivating layer (sometimes referred to as solid electrolyte interphase, SEI). In following cycles, no major features are visible until −0.08 V. Integration of oxidation and reduction charges shows that for the scan from −0.08 V to −0.25 V and back, the total cathodic charge adds up to about twice the total anodic charge that is regained above −0.08 V. The anodic charge is assigned to the stripping of Li layers that were plated onto the stainless steel

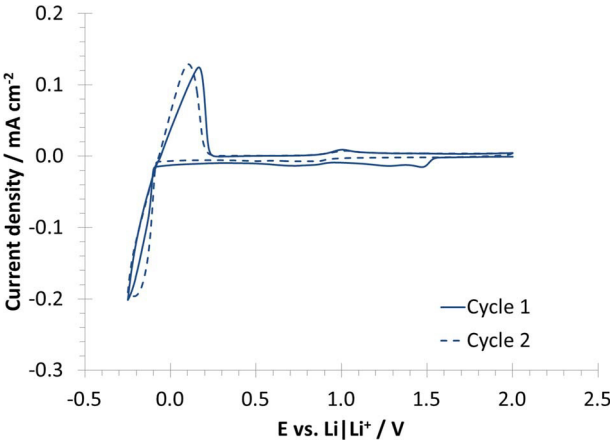

Fig. 6 Cyclic voltammogram for 0.5 M LiTFSI in PipGuan-TFSI in a coin cell set-up with stainless steel as a working and Li as a combined counter&reference electrode, respectively, with a scan rate of 0.3 mV s^{-1}.

electrode at $E < -0.08$ V. The cathodic charge thus splits into contributions from Li plating and electrolyte decomposition in coarsely equal shares. Scans to lower E revealed a more pronounced increase of the negative as compared to the positive charge in the anodic counter-peak, indicating that electrolyte decomposition becomes dominating at more negative potentials. Comparing the CV in Fig. 6 with the linear sweep scan of the plain IL in Fig. 5b, the onset of electrolyte decomposition seems to be shifted to more negative potentials in the presence of Li^+ ions in the solution.

It was speculated previously that the addition of LiTFSI enables the formation of a passivating layer that widens the potential window.[40,41] In-depth studies on the composition of this layer have been conducted earlier by other groups.[42–44]

As highlighted above, however, the Li based reference potentials in the plain and in the LiTFSI containing IL should not be directly compared: if the potential determining equilibrium reaction is $Li_{solid} \leftrightarrow Li^+ + e^-$, the Li^+ concentration in the neat IL is undefined and can easily be several orders of magnitude below the one in the electrolyte with 0.5 M LiTFSI.[39] According to the Nernst equation the pseudo-reference potential in the neat IL can thus be several multiples of 59 mV more negative than the $Li|Li^+$ potential in the electrolyte. Such a shift could be the main reason for the different onset potentials for cathodic IL decomposition without (Fig. 5b) and with (Fig. 6) LiTFSI in the solution. IUPAC recommends the utilization of dissolved redox couples (*e.g.*, ferrocene/ferrocenium) as internal references in such systems.[39,45–47] Using this method, we seek to clarify the actual effect of LiTFSI on the width of the potential stability window in upcoming experiments. As to the potential scale in Fig. 6, one should also emphasise that Li deposition and dissolution is setting in at −0.08 V in the negative and positive going scan, respectively, and not at 0 V as one should expect. This means that the $Li|Li^+$ potential is more negative for the freshly deposited Li film than for the Li foil used as combined counter&reference electrode. We tentatively assign this potential difference to a chemical modification of the surface of the Li foil due to (electro-)chemical side reactions as they will be discussed in more detail below. Apart from the open questions related to the electrochemical equilibrium potentials, however, the Li plating/stripping behaviour in Fig. 6 confirms transport of Li^+ between the two electrodes and thus the suitability of PipGuan-TFSI as electrolyte solvent for Li-ion batteries.

Apart from the Li^+ transport properties and the potential dependent electrochemical stability of PipGuan-TFSI we also studied its interaction with metallic Li. Specifically, we used EIS to analyse the charge transfer properties of the interface between metallic Li and PipGuan-TFSI + 0.5 M LiTFSI. Fig. 7 shows the evolution of the impedance response of a cell that was stored at room temperature under open circuit conditions, just interrupted by the EIS measurements. The intercept of the

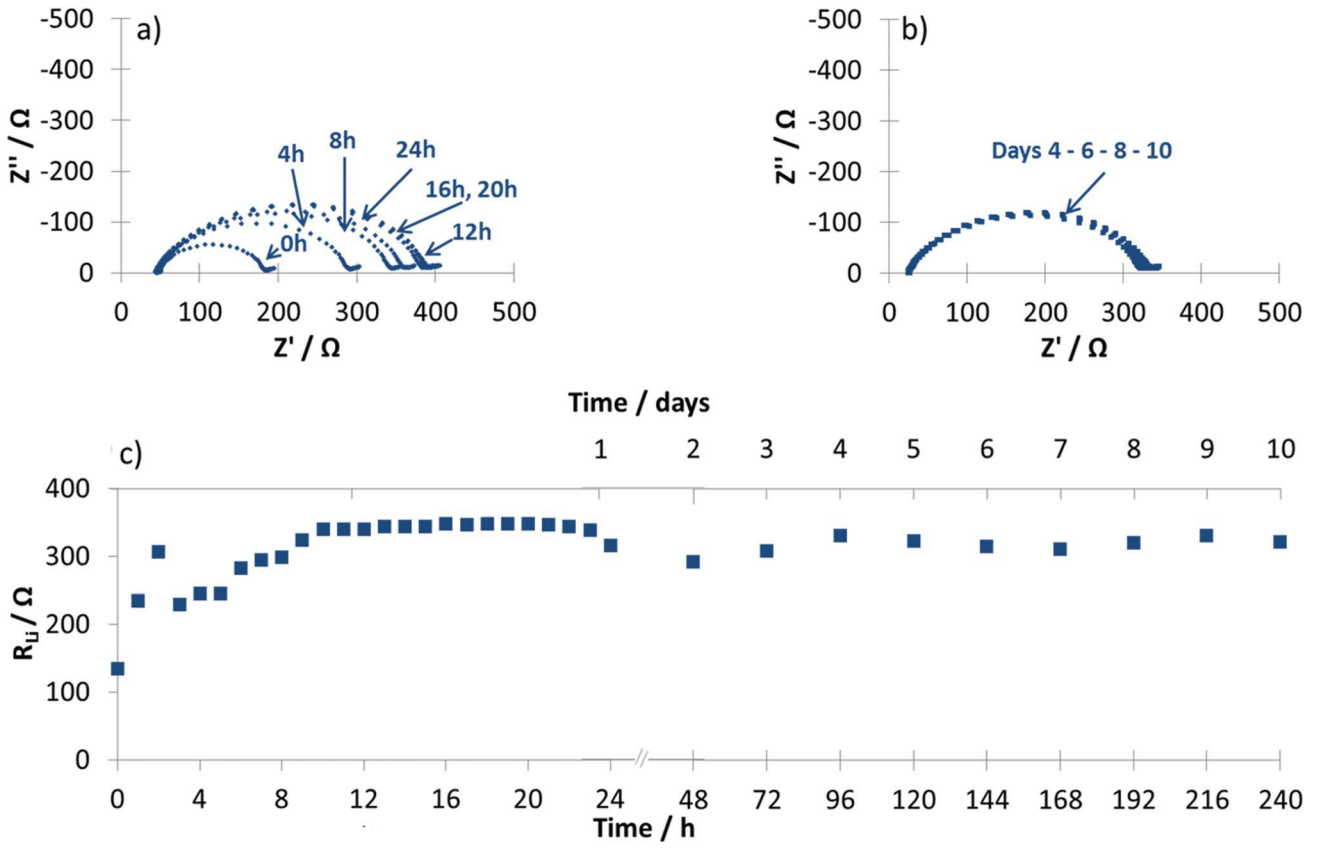

Fig. 7 Impedance response of a symmetrical Li|0.5 M LiTFSI in PipGuan-TFSI|Li cell stored at room temperature during the first (a) 12 hours, (b) 10 days, (c) time evolution of R_{Li}.

semicircles at high frequencies (left side) was associated with the bulk resistance. The difference between the two intercepts with the real axis was interpreted as the electrode-electrolyte resistance (R_{Li}), combining both the charge transfer and the passivating layer resistance. Of these two components, R_{Li} is probably dominated by the resistance of the passivating layer.[17,48,49] As can be seen from Fig. 7a, resistance stabilised after 12 hours. Fig. 7b shows the long-term impedance test over 10 days, which shows only little change in the R_{Li} resistance. This indicates that a passivating layer is forming at the lithium electrode during the first 12 hours, and that it stays stable afterwards. Due to the open circuit conditions, this formation must be a chemical or a corrosion type of reaction.

To complete the picture of PipGuan-TFSI as a suitable electrolyte solvent for Li-ion batteries we examined the charge/discharge behaviour of $LiFePO_4$ half cells at different *C*-rates and two different temperatures (24 and 55 °C). Coin cells were tested by running four cycles at every C-rate before increasing the C-rate. The presented capacities correspond to the fourth cycle for every C-rate. Fig. 8a shows a discharge capacity of 154 mA h g^{-1} for charge/discharge at 0.025 C. The same capacity was found in a test experiment with the same electrodes and commercial electrolyte (EC:DMC, 1 M $LiPF_6$) at 0.2 C. For 0.05 C and 0.1 C, the discharge capacities attained with the PipGuan-TFSI based electrolyte reduce to 143 mA h g^{-1} and 101 mA h g^{-1}, respectively. Such a negative correlation of *C*-rate and capacity is commonly observed and attributed to the high viscosity of ionic liquids.[9,19,50] This assignment fits

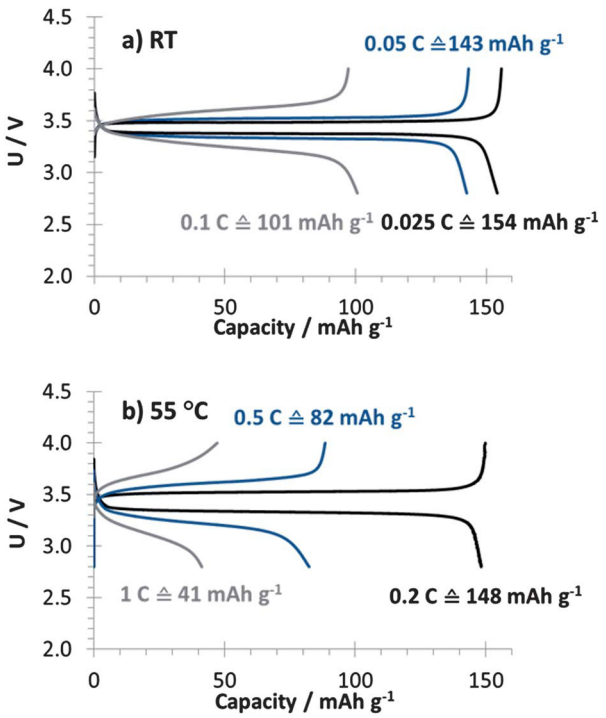

Fig. 8 Charge/discharge behaviour of 0.5 M LiTFSI in PipGuan-TFSI in a coin cell with lithium iron phosphate and lithium electrodes; (a) 24 °C, (b) 55 °C.

to the observed charge/discharge behaviour at 55 °C (Fig. 8b), where a capacity of 148 mA h g^{-1} is reached at 0.2 C. This capacity is almost 150% of the value obtained at 0.1 C and 24 °C. Furthermore, it is about the same capacity as we could reach for an identical half cell with standard electrolyte (1 M $LiPF_6$ in EC/DMC) at the same C-rate and at 24 °C (curve not shown here). In summary, the data in Fig. 8 indicate that the main disadvantage of PipGuan-TFSI as an electrolyte solvent for Li-ion batteries is a poor Li^+ conductivity due to a high viscosity. Increasing the temperature to 55 °C lowers the viscosity by about a factor of four, which must be the reason for the improved half-cell performance at that temperature.[29] Furthermore, the achieved discharge capacities for PipGuan-TFSI based electrolyte (143 mA h g^{-1} at 0.05 C, 101 mA h g^{-1} at 0.1 C at 24 °C) lay above the values of 93 mA h g^{-1} (0.05 C) and 80 mA h g^{-1} (0.1 C) that were reported for *N*-butyl-*N*-methyl-piperidinium-TFSI[19] and *N*-butyl-*N*,*N*′,*N*′,*N*″,*N*″-pentamethylguanidinium-TFSI,[32] respectively. In this respect, the performance of the PipGuan-TFSI based electrolyte does not lie between the two classes of material but is better than the respective individual performances.

Conclusions

A new ionic liquid that combines the structures of piperidinium and guanidinium based ionic liquids, PipGuan-TFSI, has been synthesised. The physical properties, *i.e.*, thermal stability, viscosity and conductivity of this new material lie between these two different classes of ionic liquids. PipGuan-TFSI has a large electrochemical window and is able to reversibly plate and strip lithium. Thus, it is promising as a new electrolyte in lithium ion batteries. Its performance in a half cell equals that of commercial electrolytes at low *C*-rates or at elevated temperatures. As PipGuan-TFSI outperforms other common guanidinium and piperidinium based ionic liquids with regard to achieved capacities of $LiFePO_4$ half cells, the synthesis goal has been exceeded. The approach of target oriented "genetic crossing" of structural elements in IL molecules is a promising complement to computational screening and incremental modification of existing ILs. We expect this approach to trigger further improvements in the development of advanced electrolytes in the near future.

Acknowledgements

The authors would like to thank Mr Jan Geder for helping with the TGA-MS measurements, Ms. Shubha Nageswaran for fruitful and interesting discussions regarding the work described in this article, and Mr Xiaohan Wu for his help in conducting the experiments. The authors would also like to thank SOLVAY SA for providing the LiTFSI-salt. Maria Arkhipova thanks the State of Baden-Wuerttemberg for a graduate fellowship. This work was financially supported by the Singapore National Research Foundation under its Campus for Research Excellence and Technological Enterprise (CREATE) programme.

Notes and references

1 A.-O. Diallo, A. B. Morgan, C. Len and G. Marlair, *Energy Environ. Sci.*, 2013, **6**, 699.
2 H. Ohno, *Electrochemical Aspects of Ionic Liquids*, John Wiley & Sons, Inc., Hoboken, NJ, USA, 2005.
3 P. Wasserscheid and T. Welton, *Ionic Liquids in Synthesis*, Wiley-VCH Verlag GmbH & Co. KGaA, Weinheim, Germany, 2007.
4 N. MacDowell, N. Florin, A. Buchard, J. Hallett, A. Galindo, G. Jackson, C. S. Adjiman, C. K. Williams, N. Shah and P. Fennell, *Energy Environ. Sci.*, 2010, **3**, 1645.
5 X. Zhang, X. Zhang, H. Dong, Z. Zhao, S. Zhang and Y. Huang, *Energy Environ. Sci.*, 2012, **5**, 6668.
6 J. F. Wishart, *Energy Environ. Sci.*, 2009, **2**, 956.
7 M. Galiński, A. Lewandowski and I. Stępniak, *Electrochim. Acta*, 2006, **51**, 5567–5580.
8 M. Armand, F. Endres, D. R. MacFarlane, H. Ohno and B. Scrosati, *Nat. Mater.*, 2009, **8**, 621–629.
9 A. Lewandowski and A. Świderska-Mocek, *J. Power Sources*, 2009, **194**, 601–609.
10 H. Sakaebe, H. Matsumoto and K. Tatsumi, *Electrochim. Acta*, 2007, **53**, 1048–1054.
11 F. Endres, *Phys. Chem. Chem. Phys.*, 2012, **14**, 5008–5009.
12 S. Passerini and W. A. Henderson, in *Encyclopedia of Electrochemical Power Sources*, ed. J. Garche, Elsevier B.V., 2009, vol. 5, pp. 85–91.
13 C. H. Hamann, A. Hamnett and W. Vielstich, *Electrochemistry*, Wiley VCH, Weinheim, 2007, vol. 2.
14 E. I. Izgorodina, *Phys. Chem. Chem. Phys.*, 2011, **13**, 4189–4207.
15 J. Scheers, P. Johansson and P. Jacobsson, *J. Electrochem. Soc.*, 2008, **155**, A628.
16 P. Johansson, L. E. Fast, A. Matic, G. B. Appetecchi and S. Passerini, *J. Power Sources*, 2010, **195**, 2074–2076.
17 A. Fernicola, F. Croce, B. Scrosati, T. Watanabe and H. Ohno, *J. Power Sources*, 2007, **174**, 342–348.
18 S. Seki, Y. Ohno, Y. Kobayashi, H. Miyashiro, A. Usami, Y. Mita, H. Tokuda, M. Watanabe, K. Hayamizu, S. Tsuzuki, M. Hattori and N. Terada, *J. Electrochem. Soc.*, 2007, **154**, A173–A177.
19 J. Jin, H. H. Li, J. P. Wei, X. K. Bian, Z. Zhou and J. Yan, *Electrochem. Commun.*, 2009, **11**, 1500–1503.
20 V. Borgel, E. Markevich, D. Aurbach, G. Semrau and M. Schmidt, *J. Power Sources*, 2009, **189**, 331–336.
21 M. Montanino, F. Alessandrini, S. Passerini and G. B. Appetecchi, *Electrochim. Acta*, 2013, **96**, 124–133.
22 M. Egashira, S. Okada, J. Yamaki, D. A. Dri, F. Bonadies and B. Scrosati, *J. Power Sources*, 2004, **138**, 240–244.
23 J. Sun, M. Forsyth and D. R. MacFarlane, *J. Phys. Chem. B*, 1998, **102**, 8858–8864.
24 S. Fang, Z. Zhang, Y. Jin, L. Yang, S. Hirano, K. Tachibana and S. Katayama, *J. Power Sources*, 2011, **196**, 5637–5644.
25 A. P. Lewandowski, A. F. Hollenkamp, S. W. Donne and A. S. Best, *J. Power Sources*, 2010, **195**, 2029–2035.
26 T. Waldmann, H.-H. Huang, H. E. Hoster, O. Höfft, F. Endres and R. J. Behm, *ChemPhysChem*, 2011, **12**, 2565–2567.
27 S. Fang, L. Yang, J. Wang, H. Zhang, K. Tachibana and K. Kamijima, *J. Power Sources*, 2009, **191**, 619–622.
28 W. Kantlehner, E. Haug, W. W. Mergen, P. Speh, T. Maier, J. J. Kapassakalidis, H.-J. Braeuner and H. Hagen, *Liebigs Ann. Chem.*, 1984, 108–126.
29 Y. Jin, S. Fang, L. Yang, S. Hirano and K. Tachibana, *J. Power Sources*, 2011, **196**, 10658–10666.
30 S. Fang, L. Yang, C. Wei, C. Jiang, K. Tachibana and K. Kamijima, *Electrochim. Acta*, 2009, **54**, 1752–1756.
31 M. Gnahm, C. Berger, M. Arkhipova, H. Kunkel, T. Pajkossy, G. Maas and D. M. Kolb, *Phys. Chem. Chem. Phys.*, 2012, **14**, 10647–10652.
32 X. Zhang, S. Fang, Z. Zhang and L. Yang, *Chin. Sci. Bull.*, 2011, **56**, 2906–2910.
33 H. Kunkel and G. Maas, *Eur. J. Org. Chem.*, 2007, 3746–3757.
34 M. Montanino, M. Carewska, F. Alessandrini, S. Passerini and G. B. Appetecchi, *Electrochim. Acta*, 2011, **57**, 153–159.
35 J. Reiter, M. Nádherná and R. Dominko, *J. Power Sources*, 2012, **205**, 402–407.
36 K. Liu, Y.-X. Zhou, H.-B. Han, S.-S. Zhou, W.-F. Feng, J. Nie, H. Li, X.-J. Huang, M. Armand and Z.-B. Zhou, *Electrochim. Acta*, 2010, **55**, 7145–7151.
37 O. O. Okoturo and T. J. VanderNoot, *J. Electroanal. Chem.*, 2004, **568**, 167–181.
38 M. L. F. Nascimento and C. Aparicio, *Phys. B*, 2007, **398**, 71–77.
39 A. a. J. Torriero, J. Sunarso and P. C. Howlett, *Electrochim. Acta*, 2012, **82**, 60–68.
40 P. Reale, A. Fernicola and B. Scrosati, *J. Power Sources*, 2009, **194**, 182–189.
41 J. Hassoun, A. Fernicola, M. A. Navarra, S. Panero and B. Scrosati, *J. Power Sources*, 2010, **195**, 574–579.
42 P. C. Howlett, N. Brack, A. F. Hollenkamp, M. Forsyth and D. R. MacFarlane, *J. Electrochem. Soc.*, 2006, **153**, A595.
43 P. C. Howlett, D. R. MacFarlane and A. F. Hollenkamp, *Electrochem. Solid-State Lett.*, 2004, **7**, A97.
44 L. Suo, Y.-S. Hu, H. Li, M. Armand and L. Chen, *Nat. Commun.*, 2013, **4**, 1481.
45 P. De Vreese, K. Haerens, E. Matthijs and K. Binnemans, *Electrochim. Acta*, 2012, **76**, 242–248.
46 A. Lewandowski, L. Waligora and M. Galinski, *Electroanalysis*, 2009, **21**, 2221–2227.
47 D. Weingarth, a. Foelske-Schmitz, a. Wokaun and R. Kötz, *Electrochem. Commun.*, 2012, **18**, 116–118.
48 J. Thevenin, *J. Power Sources*, 1985, **14**, 45–52.
49 S. Seki, Y. Ohno, H. Miyashiro, Y. Kobayashi, A. Usami, Y. Mita, N. Terada, K. Hayamizu, S. Tsuzuki and M. Watanabe, *J. Electrochem. Soc.*, 2008, **155**, A421.
50 H. Matsumoto, H. Sakaebe, K. Tatsumi, M. Kikuta, E. Ishiko and M. Kono, *J. Power Sources*, 2006, **160**, 1308–1313.

5 Conclusion

Research in sodium-ion batteries has surged in recent years, and understanding of the processes associated with the (de-)insertion of Na^+ into (from) host materials increases rapidly. However, one barrier to commercially viable NIBs is still cycling stability for the majority of materials. Layered transition metal oxides, specifically P2-Na_xMnO_{2+z}, are considered a very promising material class due to their good compromise between capacity and potential.

Several strategies have been presented to increase the cycling stability. The most prominent approach has been incorporation of different metals into the host lattice in order to increase stability, but also elevate the potential of redox processes. One route presented in this work is in line with this research direction. Namely, the substitution or doping of the layered manganese structure with a small amount of cobalt (~10%). In addition a new approach to improving stability was followed, namely optimisation of the morphology.

For Na_xMnO_2 flakes, NIB half-cells showed a considerable capacity fading after only 20 cycles. Interestingly, not only the main redox process of the $Mn^{2+|3+}$ redox couple was observed, but a variety of other processes which were attributed to Na^+-ordering processes between the MnO_2-layers. Incorporation of Co into the structure resulted in two effects: cycling stability was enhanced, and the aforementioned ordering processes were suppressed. As these differences were attributed to structural processes – or the lack thereof -, an electrochemical *in operando* XRD cell for laboratory-scale diffractometers was constructed. In contrast to a variety of electrochemical *in operando* XRD cells that had been reported before, this here presented cell distinguishes itself through the ability to use ultrathin aluminium (6 µm) as window material. This is achieved through various elements with regard to the construction of the cell, which alleviates the pressure on the X-ray window in the inner part of the cell. As the low thickness of the Al-foil reduces X-ray absorption, and contributes only very few reflections to the overall pattern, it ensures excellent signal quality and an excellent signal to noise ratio. Thus, initial measurements proved promising.

However, in order to ensure that the observed structural phenomena could indeed be attributed to processes occurring in the bulk of the material, and not only on the electrodes surface, synchrotron X-ray diffraction measurements were conducted. While Na_xMnO_2-flakes showed phase transition from the hexagonal $P6_3/mmc$ to the

orthorhombic *Cmcm* phase, this transformation is absent for the Co-doped version, $Na_xCo_{0.1}Mn_{0.9}O_2$. Even though this transition has been shown to be reversible, repeated structure changes still exert stress on the structure and the long-range order of the material. Reducing this stress through Co-doping results in higher cycling stability. This positive effect is augmented by the suppression of Na^+-ordering processes. Moreover, a positive effect of Co-doping on the Na-ion transport in the host structure has been found.

The other strategy to improve cycling stability was optimisation of the morphology. Instead of Na_xMnO_2 flakes, Na_xMnO_2 spheres were synthesised. This was based on the assumption that the spherical morphology can accommodate repeated (de-)insertion processes, and the concurrent volume changes, better. The spherical morphology not only increased capacity, it also retained this capacity better over the course of 100 cycles. *In operando* XRD measurements also showed structural changes for spherical Na_xMnO_2 at the end of the discharge 1.5 V. However, the change of the unit cell volume of the Na_xMnO_2 spheres was significantly smaller; concurrently, the strain within the unit cell seems to increase during Na^+-insertion. This suggests that sodium-insertion is (mostly) accommodated by volume changes inducing structural stress in the flakes, whereas for the spheres it is compensated by strain. As the capacity retention is higher for the spheres, it is concluded that compensation via the strain mechanism is less detrimental for the system. Thus, while the underlying cause for the improvement of cycling stability is different to results of Co-doping, the effect is similarly positive.

Ultimately, as both strategies contribute to improvements of cycling stability via two different effects, both were combined in the synthesised $Na_xCo_{0.1}Mn_{0.9}O_2$ spheres. They not only show an enhanced initial capacity over the NCO flakes, just like the NMO spheres did over the NMO flakes, but cycling stability was also improved as compared to NMO flakes, NCO flakes, and NMO spheres. Therefore, it can be concluded that both positive effects on cycling stability, suppression of structural transformation and better accommodation of inserted Na^+, can be combined to provide a superior NIB cathode material.

While Co has a positive effect on both, other works stressed either only the suppression of phase transitions (*e.g.* for Ni)[79,86,138,139], or the suppression of Na^+-ordering processes (*e.g.* for Fe)[88,140,141] as an effect of doping. Moreover, in contrast to previously reported results on incorporating Mn into a Co-based structure,[85] this

could be achieved with a Co-content as low as 10% into a Mn-based structure. In addition, unlike for the case of starting with Na_xCoO_2 and incorporating Mn,[85] the approach described in this work does not decrease the insertion potential significantly. The new descripted morphology optimisation adds another alternative to the repertoire of strategies to improve cycling stability which has not been investigated before for the class of layered transition metal oxides for NIBs. Combining both routes results in spherical $Na_xCo_{0.1}Mn_{0.9}O_2$, which results in an initial capacity of 180 mA h g^{-1} when cycled between 1.5 – 3.8 V *vs.* Na, of which approximately 120 mA h g^{-1} and 110 mA h g^{-1} are retained after 100 and 150 cycles, respectively, at a moderate rate of 50 mA g^{-1}. Furthermore, an excellent rate capability with capacities of roughly 140 mA h g^{-1}at 200 mA g^{-1} (~1.1C; 1C ≙ 186 mA h g^{-1}, calculation based on 0.7 Na^+ per formula unit) and 120 mA h g^{-1}at 400 mA g^{-1} (~2.2C) is achieved. These values exceed most materials presented in recent literature (Table 2). Among those, it is worth noting that Co-containing materials show the highest stabilities. This is in line with our findings and supports our hypothesis that the incorporation of cobalt has a decisive positive influence.

Material	Cycling rate / mA g^{-1}	Potential range / V	Initial capacity / mA h g^{-1}	Achieved capacity / mA h g^{-1} [cycle #]
$Na_{2/3}Ni_{1/3}Mn_{2/3}O_2$[139]	17	1.5 – 3.75	156	125 [50]
$Na_xMg_{0.11}Mn_{0.89}O_2$[90]	12	1.5 – 4.4	174	121 [100]
				97 [200]
$Na_{0.67}Mn_{0.5}Fe_{0.5}O_2$[140]	13	1.5 – 4.0	140	125* [30]
$Na_xFe_{0.5}Mn_{0.5}O_2$[88]	18* (0.1C)	1.5 – 4.0	140*	30* [80]
$Na_xFe_{0.5}Mn_{0.5}O_2$[35]	13	1.5 – 4.2	190	150* [30]
$Na_{0.7}Fe_{0.45}Mn_{0.45}Co_{0.2}O_2$[142]	10	1.5 – 4.5	190	110 [60]
$Na_{0.67}Mn_{0.65}Ni_{0.2}Co_{0.15}O_2$[143]	120	1.5 – 4.2	137	107 [100]
$Na_xNi_{0.22}Co_{0.11}Mn_{0.66}O_2$[93]	12	2.1 – 4.3	141	116 [150]
$Na_{0.5}$ $Mn_{0.63}Ni_{0.23}Fe_{0.13}O_2$[92]	50	1.5 – 4.6	195*	160* [70]
$Na_{0.67}Mn_{0.65}Ni_{0.15}Fe_{0.2}O_2$[140]	13	1.5 – 4.1	160	140* [30]

Table 2. Cycling performance overview of state of the art P2-type materials. Estimated values are denoted with (*).

In summary, for sodium-ion batteries to become a commercially attractive alternative to lithium-ion batteries, significant further improvements are necessary. In this work, two viable strategies that have the potential to bring sodium-ion batteries closer to commercial applications have been successfully demonstrated and explained.

6 References

[1] K. Kordesch, W. Taucher-Mautner, *Encycl. Electrochem. Power Sources* **2009**, 43.

[2] T. Takamura, *Encycl. Electrochem. Power Sources* **2009**, 28.

[3] E. Sayilgan, T. Kukrer, G. Civelekoglu, F. Ferella, A. Akcil, F. Veglio, M. Kitis, *Hydrometallurgy* **2009**, *97*, 158.

[4] G. Belardi, P. Ballirano, M. Ferrini, R. Lavecchia, F. Medici, L. Piga, A. Scoppettuolo, *Thermochim. Acta* **2011**, *526*, 169.

[5] B. Scrosati, *J. Solid State Electrochem.* **2011**, *15*, 1623.

[6] S. Yang, H. Knickle, *J. Power Sources* **2002**, *112*, 162.

[7] Q. Li, N. J. Bjerrum, *J. Power Sources* **2002**, *110*, 1.

[8] M. A. Rahman, X. Wang, C. Wen, *J. Electrochem. Soc.* **2013**, *160*, A1759.

[9] "Phinergy company web page," can be found under www.phinergy.com, **2013**. (Date Accessed: 2015-10-25)

[10] J. Yuan, J. S. Yu, B. Sundén, *J. Power Sources* **2015**, *278*, 352.

[11] F. W. Küster, A. Thiel, K. Fischbeck, *Rechentafeln Für Die Chemische Analytik*, DeGruyter, **2002**.

[12] R. Whitlock, "Alcoa and Phinergy to develop EV batteries that run on air and aluminium," can be found under http://www.renewableenergymagazine.com/article/alcoa-and-phinergy-to-develop-ev-batteries-20140206, **2014**. (Date Accessed: 2015-10-25)

[13] M. Ehsani, Y. Gao, A. Emadi, *Modern Electric, Hybrid Electric, and Fuel Cell Vehicles: Fundamentals, Theory, and Design*, CRC Press, **2009**.

[14] D. G. Enos, in *Adv. Batter. Mediu. Large-Scale Energy Storage* (Eds.: C. Menictas, M. Skyllas-Kazacos, L.T. Mariana), Elsevier, **2015**, pp. 57–71.

[15] P. T. Moseley, D. A. J. Rand, K. Peters, *J. Power Sources* **2015**, *295*, 268.

[16] L. Le Guenne, P. Bernard, *J. Power Sources* **2002**, *105*, 134.

[17] W. H. Zhu, Y. Zhu, Z. Davis, B. J. Tatarchuk, *Appl. Energy* **2013**, *106*, 307.

[18] B. Mebarki, B. Draoui, L. Rahmani, B. Allaoua, *Energy Procedia* **2013**, *36*, 130.

[19] M. Galeotti, C. Giammanco, L. Cinà, S. Cordiner, A. Di Carlo, *Energy Convers. Manag.* **2015**, *92*, 1.

[20] G. Lota, A. Sierczynska, I. Acznik, K. Lota, *Int. J. Electrochem. Sci.* **2014**, *9*, 659.

[21] M. V Lototsky, M. Williams, V. A. Yartys, Y. V Klochko, V. M. Linkov, *J. Alloys Compd.* **2011**, *509, Suppl*, S555.

[22] W. H. Zhu, Y. Zhu, Z. Davis, B. J. Tatarchuk, *Appl. Energy* **2013**, *106*, 307.

[23] C. A. Vincent, *Solid State Ionics* **2000**, *134*, 159.

[24] R. Ruffo, C. Wessells, R. A. Huggins, Y. Cui, *Electrochem. Commun.* **2009**, *11*, 247.

[25] S. Frangini, M. Carewska, S. Passerini, S. Scaccia, *J. New Mater. Electrochem. Syst.* **2001**, *4*, 83.

[26] N. Bucher, S. Hartung, A. Nagasubramanian, Y. L. Cheah, H. E. Hoster, S. Madhavi, *ACS Appl. Mater. Interfaces* **2014**, *6*, 8059.

[27] S. Hartung, N. Bucher, H.-Y. Chen, R. Al-Oweini, S. Sreejith, P. Borah, Z. Yanli, U. Kortz, U. Stimming, H. E. Hoster, M. Srinivasan, *J. Power Sources* **2015**, *288*, 270.

[28] M. S. Whittingham, *Prog. Solid State Chem.* **1978**, *12*, 41.

[29] K. M. Abraham, *Solid State Ionics* **1982**, *7*, 199.

[30] J. Emsley, *Nature's Building Blocks: An A-Z Guide to the Elements*, Oxford University Press, **2001**.

[31] H. Hofbauer, *Factsheet: Lithium*, Global 2000 Verlagges. M. B. H., Vienna, **2013**.

[32] N. Yabuuchi, K. Kubota, M. Dahbi, S. Komaba, *Chem. Rev.* **2014**, *114*, 11636.

[33] S. Komaba, W. Murata, T. Ishikawa, N. Yabuuchi, T. Ozeki, T. Nakayama, A. Ogata, K. Gotoh, K. Fujiwara, *Adv. Funct. Mater.* **2011**, *21*, 3859.

[34] S. Komaba, T. Ishikawa, N. Yabuuchi, W. Murata, A. Ito, Y. Ohsawa, *ACS Appl. Mater. Interfaces* **2011**, *3*, 4165.

[35] N. Yabuuchi, M. Kajiyama, J. Iwatate, H. Nishikawa, S. Hitomi, R. Okuyama, R. Usui, Y. Yamada, S. Komaba, *Nat. Mater.* **2012**, *11*, 512.

[36] D. Kundu, E. Talaie, V. Duffort, L. F. Nazar, *Angew. Chemie Int. Ed.* **2015**, *54*, 3431.

[37] Y. Hamon, T. Brousse, F. Jousse, P. Topart, P. Buvat, D. M. Schleich, *J. Power Sources* **2001**, *97-98*, 185.

[38] S. P. Ong, V. L. Chevrier, G. Hautier, A. Jain, C. Moore, S. Kim, X. Ma, G. Ceder, *Energy Environ. Sci.* **2011**, *4*, 3680.

[39] C. Masquelier, L. Croguennec, *Chem. Rev.* **2013**, *113*, 6552.

[40] M. Dollé, J. Hollingsworth, T. J. Richardson, M. M. Doeff, *Solid State Ionics* **2004**, *175*, 225.

[41] M. Dollé, S. Patoux, M. M. Doeff, *Chem. Mater.* **2005**, *17*, 1036.

[42] T. A. Eriksson, Y. J. Lee, J. Hollingsworth, J. A. Reimer, E. J. Cairns, X. F. Zhang, M. M. Doeff, *Chem. Mater.* **2003**, *15*, 4456.

[43] K. Kuratani, N. Uemura, H. Senoh, H. T. Takeshita, T. Kiyobayashi, *J. Power Sources* **2013**, *223*, 175.

[44] M. Okoshi, Y. Yamada, A. Yamada, H. Nakai, *J. Electrochem. Soc.* **2013**, *160*, A2160.

[45] Y. Yamada, Y. Koyama, T. Abe, Z. Ogumi, *J. Phys. Chem. C* **2009**, *113*, 8948.

[46] Y. Yamada, Y. Iriyama, T. Abe, Z. Ogumi, *Langmuir* **2009**, *25*, 12766.

[47] V. Palomares, P. Serras, I. Villaluenga, K. B. Hueso, J. Carretero-González, T. Rojo, *Energy Environ. Sci.* **2012**, *5*, 5884.

[48] V. Palomares, M. Casas-Cabanas, E. Castillo-Martínez, M. H. Han, T. Rojo, *Energy Environ. Sci.* **2013**, *6*, 2312.

[49] B. L. Ellis, L. F. Nazar, *Curr. Opin. Solid State Mater. Sci.* **2012**, *16*, 168.

[50] H. Pan, Y.-S. Hu, L. Chen, *Energy Environ. Sci.* **2013**, *6*, 2338.

[51] S.-M. Oh, S.-T. Myung, J. Hassoun, B. Scrosati, Y.-K. Sun, *Electrochem. Commun.* **2012**, *22*, 149.

[52] M. Casas-Cabanas, V. V. Roddatis, D. Saurel, P. Kubiak, J. Carretero-González, V. Palomares, P. Serras, T. Rojo, *J. Mater. Chem.* **2012**, *22*, 17421.

[53] K. Zaghib, J. Trottier, P. Hovington, F. Brochu, A. Guerfi, A. Mauger, C. M. Julien, *J. Power Sources* **2011**, *196*, 9612.

[54] B. L. Ellis, W. R. M. Makahnouk, Y. Makimura, K. Toghill, L. F. Nazar, *Nat. Mater.* **2007**, *6*, 749.

[55] N. Recham, J.-N. Chotard, L. Dupont, K. Djellab, M. Armand, J.-M. Tarascon, *J. Electrochem. Soc.* **2009**, *156*, A993.

[56] Y. U. Park, D. H. Seo, H. S. Kwon, B. Kim, J. Kim, H. Kim, I. Kim, H. I. Yoo, K. Kang, *J. Am. Chem. Soc.* **2013**, *135*, 13870.

[57] R. A. Shakoor, D.-H. Seo, H. Kim, Y.-U. Park, J. Kim, S.-W. Kim, H. Gwon, S. Lee, K. Kang, *J. Mater. Chem.* **2012**, *22*, 20535.

[58] W. Song, X. Ji, Z. Wu, Y. Zhu, F. Li, Y. Yao, C. E. Banks, *RSC Adv.* **2014**, *4*, 11375.

[59] C. Zhu, K. Song, P. A. Van Aken, J. Maier, Y. Yu, *Nano Lett.* **2014**, *14*, 2175.

[60] M. Xu, L. Wang, X. Zhao, J. Song, H. Xie, Y. Lu, J. B. Goodenough, *Phys. Chem. Chem. Phys.* **2013**, *15*, 13032.

[61] M. Reynaud, M. Ati, S. Boulineau, M. T. Sougrati, B. C. Melot, G. R. J.-N. Chotard, J.-M. Tarascon, *ECS Trans.* **2013**, *50*, 11.

[62] P. Barpanda, G. Oyama, S. Nishimura, S.-C. Chung, A. Yamada, *Nat. Commun.* **2014**, *5*, 4358.

[63] Y. Lu, L. Wang, J. Cheng, J. B. Goodenough, *Chem. Commun.* **2012**, *48*, 6544.

[64] Y. You, X.-L. Wu, Y.-X. Yin, Y.-G. Guo, *Energy Environ. Sci.* **2014**, *7*, 1643.

[65] L. Wang, Y. Lu, J. Liu, M. Xu, J. Cheng, D. Zhang, J. B. Goodenough, *Angew. Chemie Int. Ed.* **2013**, *52*, 1964.

[66] H.-W. Lee, R. Y. Wang, M. Pasta, S. W. Lee, N. Liu, Y. Cui, *Nat. Commun.* **2014**, *5*, 5280.

[67] T. Matsuda, M. Takachi, Y. Moritomo, *Chem. Commun.* **2013**, *49*, 2750.

[68] K. West, B. Zachau-Christiansen, T. Jacobsen, S. Skaarup, *J. Power Sources* **1989**, *26*, 341.

[69] K. West, B. Zachau-Christiansen, T. Jacobsen, S. Skaarup, *Solid State Ionics* **1988**, *28-30*, 1128.

[70] S. Hartung, N. Bucher, J. B. Franklin, A. M. Wise, L. Y. Lim, H.-Y. Chen, M. F. Nelson Weker, Johanna Michel-Beyerle, Maria-E. Toney, M. Srinivasan, *Adv. Energy Mater.* **2015**, Submitted manuscript.

[71] S. Tepavcevic, H. Xiong, V. R. Stamenkovic, X. Zuo, M. Balasubramanian, V. B. Prakapenka, C. S. Johnson, T. Rajh, *ACS Nano* **2012**, *6*, 530.

[72] S. Hartung, N. Bucher, V. S. Nair, Y. L. Cheah, Y. Wang, H. E. Hoster, M. Srinivasan, *Chemphyschem* **2014**, *15*, 2121.

[73] D. Nguyen, J. Gim, V. Mathew, J. Song, S. Kim, D. Ahn, J. Kim, *ECS Electrochem. Lett.* **2014**, *3*, A69.

[74] H. Kang, Y. Liu, M. Shang, T. Lu, Y. Wang, L. Jiao, *Nanoscale* **2015**, *7*, 9261.

[75] Y. Dong, S. Li, K. Zhao, C. Han, W. Chen, B. Wang, L. Wang, B. Xu, Q. Wei, L. Zhang, X. Xu, L. Mai, *Energy Environ. Sci.* **2015**, *8*, 1267.

[76] M. Guignard, C. Didier, J. Darriet, P. Bordet, E. Elkaïm, C. Delmas, *Nat. Mater.* **2012**, *11*, 1.

[77] C. Delmas, J. J. Braconnier, C. Fouassier, P. Hagenmuller, *Solid State Ionics* **1981**, *3-4*, 165.

[78] C. Delmas, C. Fouassier, P. Hagenmuller, *Phys. B+C* **1980**, *99*, 81.

[79] D. H. Lee, J. Xu, Y. S. Meng, *Phys. Chem. Chem. Phys.* **2013**, *15*, 3304.

[80] K. Kubota, N. Yabuuchi, H. Yoshida, M. Dahbi, S. Komaba, *MRS Bull.* **2014**, *39*, 416.

[81] J. Parant, R. Olazcuaga, M. Devalette, C. Fouassier, P. Hagenmuller, *J. Solid State Chem.* **1971**, *3*, 1.

[82] J. J. Braconnier, C. Delmas, P. Hagenmuller, *Mater. Res. Bull.* **1982**, *17*, 993.

[83] J. Molenda, C. Delmas, P. Hagenmuller, *Sol. Stat. Ion.* **1983**, *10*, 431.

[84] A. Mendiboure, C. Delmas, P. Hagenmuller, *J. Solid State Chem.* **1985**, *57*, 323.

[85] D. Carlier, J. H. Cheng, R. Berthelot, M. Guignard, M. Yoncheva, R. Stoyanova, B. J. Hwang, C. Delmas, *Dalt. Trans.* **2011**, *40*, 9306.

[86] Z. Lu, J. R. Dahn, *J. Electrochem. Soc.* **2001**, *148*, A1225.

[87] K. Park, D. Han, J. Shon, S. G. Doo, S. Lee, *RSC Adv.* **2015**, *5*, 6340.

[88] W. K. Pang, S. Kalluri, V. K. Peterson, N. Sharma, J. Kimpton, B. Johannessen, H. K. Liu, S. X. Dou, Z. Guo, *Chem. Mater.* **2015**, *27*, 3150.

[89] N. Sharma, N. Tapia-Ruiz, G. Singh, A. R. Armstrong, J. C. Pramudita, H. E. A. Brand, J. Billaud, P. G. Bruce, T. Rojo, *Chem. Mater.* **2015**, *27*, 6976.

[90] D. Buchholz, C. Vaalma, L. G. Chagas, S. Passerini, *J. Power Sources* **2015**, *282*, 581.

[91] J. Billaud, G. Singh, A. R. Armstrong, E. Gonzalo, V. Roddatis, M. Armand, T. Rojo, P. G. Bruce, *Energy Environ. Sci.* **2014**, *7*, 1387.

[92] I. Hasa, D. Buchholz, S. Passerini, B. Scrosati, J. Hassoun, *Adv. Energy Mater.* **2014**, *4*, 1400083 (1.

[93] L. G. Chagas, D. Buchholz, C. Vaalma, L. Wu, S. Passerini, *J. Mater. Chem. A* **2014**, *2*, 20263.

[94] M. F. Toney, in *Encycl. Mater. Charact.* (Eds.: C. Evans, S. Wilson, R. Brundle), Boston: Butterworth-Heinemann ; Greenwich, CT: Manning, **1992**, pp. 198–213.

[95] Y. Waseda, E. Matsubara, K. Shinoda, *X-Ray Diffraction Crystallography*, Springer, Berlin, Heidelberg, **2011**.

[96] C. Suryanarayana, M. G. Norton, *X-Ray Diffraction: A Practical Approach*, Springer US, Boston, MA, **1998**.

[97] H. Dittrich, A. Bieniok, *Encycl. Electrochem. Power Sources* **2009**, 718.

[98] G. E. Nauer, *Encycl. Electrochem. Power Sources* **2009**, 813.

[99] N. Yagi, in *Compr. Biomed. Phys.* (Ed.: A. Brahme), Elsevier B.V., **2014**, p. 4056.

[100] J.-P. Itie, F. Baudelet, V. Briois, E. Elkaim, A. Nadji, D. Thiaudiere, in *X-Rays Mater.* (Eds.: G. Philippe, R. Guinebretière), London : Iste ; Hoboken, NJ : Wiley, 2012, **2012**, pp. 1–48.

[101] H. Wiedemann, *Synchrotron Radiation*, Springer, Berlin, Heidelberg, **2003**.

[102] C. Hammond, *The Basics of Crystallography and Diffraction*, Oxford University Press, Oxford, UK, **2015**.

[103] R. F. Egerton, *Physical Principles of Electron Microscopy - An Introduction to TEM, SEM, and AEM*, Springer US, Boston, MA, **2005**.

[104] R. Marassi, F. Nobili, *Encycl. Electrochem. Power Sources* **2009**, 758.

[105] R. Marassi, F. Nobili, *Encycl. Electrochem. Power Sources* **2009**, 769.

[106] D. C. Bell, N. Erdman, *Low Voltage Electron Microscopy : Principles and Applications*, John Wiley & Sons, Ltd, Chichester, **2013**.

[107] Y. Leng, *Materials Characterisation: Introduction to Microscopic and Spectroscopic Methods*, JohnWiley & Sons (Asia), Singapore, **2008**.

[108] E. Margui, R. Van Grieken, *X-Ray Fluorescence Spectrometry and Related Techniques: An Introduction*, Momentum Press, New York, NY, **2013**.

[109] R. Jenkins, *X-Ray Fluorescence Spectrometry*, John Wiley & Sons, Ltd, New York, NY, **1999**.

[110] R. H. Geiss, in *Encycl. Mater. Charact.* (Eds.: R.C. Brundle, C.A.J. Evans, S. Wilson), Elsevier, Greenwich, CT, **1992**, pp. 120–134.

[111] J. M. Mermet, *Encycl. Anal. Sci.* **2005**, 210.

[112] G. Currell, *Analytical Instrumentation: Performance, Characteristics and Quality*, John Wiley & Sons, Ltd, Chichester, **2000**.

[113] B. M. Mckenna, J. G. Lyng, in *Instrum. Assess. Food Sens. Qual.* (Ed.: D. Kilkast), Woodhead Publishing Limited, Cambridge, UK, **2013**, pp. 129–162.

[114] M. Wagner, *Thermal Analysis in Practice*, Mettler Toledo, **2009**.

[115] R. Bottom, in *Princ. Appl. Therm. Anal.* (Ed.: P. Gabbott), Blackwell Publishing Ltd, Oxford, UK, **2008**, pp. 87–118.

[116] C. Daniel, J. O. Besenhard, *Handbook of Battery Materials*, Wiley Online Library, Weinheim, Germany, **2011**.

[117] M. Schmid, *Studies on Cathode Materials Based on α-Na 0.7 MnO 2 for Sodium Ion Batteries (Internship Report)*, **2015**.

[118] A. J. Bard, L. R. Faulkner, *Electrochemical Methods : Fundamentals and Applications*, John Wiley & Sons, Ltd, New York, NY, **2001**.

[119] D. W. Dees, S. Kawauchi, D. P. Abraham, J. Prakash, *J. Power Sources* **2009**, *189*, 263.

[120] W. Weppner, R. A. Huggins, *J. Electrochem. Soc.* **1977**, *124*, 1569.

[121] K. M. Shaju, G. V. Subba Rao, B. V. R. Chowdari, *Electrochim. Acta* **2004**, *49*, 1565.

[122] E. Markevich, M. D. Levi, D. Aurbach, *J. Electroanal. Chem.* **2005**, *580*, 231.

[123] J. Wang, *Analytical Electrochemistry*, Wiley VCH, Hoboken, NJ, **2006**.

[124] S.-I. Pyun, H.-C. Shin, J.-W. Lee, J.-Y. Go, *Monogr. Electrochem.* **2012**, 11.

[125] G. Bontempelli, R. Toniolo, *Encycl. Electrochem. Power Sources* **2009**, 643.

[126] Z. B. Stoynov, D. E. Vladikova, *Encycl. Electrochem. Power Sources* **2009**, 632.

[127] R. Berthelot, D. Carlier, C. Delmas, *Nat. Mater.* **2011**, *10*, 74.

[128] T. A. Platova, I. R. Mukhamedshin, H. Alloul, A. V. Dooglav, G. Collin, *Phys. Rev. B* **2009**, *80*, 224106.

[129] P. Zhang, R. Capaz, M. Cohen, S. Louie, *Phys. Rev. B* **2005**, *71*, 153102.

[130] Y. P. Wu, E. Rahm, R. Holze, *Electrochim. Acta* **2002**, *47*, 3491.

[131] J. Dong H, Y. J. Shin, S. M. Oh, *J. Electrochem. Soc.* **1996**, *143*, 2204.

[132] S. Fang, Z. Zhang, Y. Jin, L. Yang, S. Hirano, K. Tachibana, S. Katayama, *J. Power Sources* **2011**, *196*, 5637.

[133] M. Montanino, M. Carewska, F. Alessandrini, S. Passerini, G. B. Appetecchi, *Electrochim. Acta* **2011**, *57*, 153.

[134] J. Jin, H. H. Li, J. P. Wei, X. K. Bian, Z. Zhou, J. Yan, *Electrochem. Commun.* **2009**, *11*, 1500.

[135] S. Fang, L. Yang, J. Wang, H. Zhang, K. Tachibana, K. Kamijima, *J. Power Sources* **2009**, *191*, 619.

[136] S. Fang, L. Yang, C. Wei, C. Jiang, K. Tachibana, K. Kamijima, *Electrochim. Acta* **2009**, *54*, 1752.

[137] X. Zhang, S. Fang, Z. Zhang, L. Yang, *Chinese Sci. Bull.* **2011**, *56*, 2906.

[138] D. Yuan, X. Hu, J. Qian, F. Pei, F. Wu, R. Mao, X. Ai, H. Yang, Y. Cao, *Electrochim. Acta* **2014**, *116*, 300.

[139] Y. Wen, B. Wang, G. Zeng, K. Nogita, D. Ye, L. Wang, *Chem. Asian J.* **2015**, *10*, 661.

[140] L. Nazar, E. Talaie, V. Duffort, H. Smith, B. Fultz, *Energy Environ. Sci.* **2015**, *8*, 2512.

[141] B. Mortemard de Boisse, D. Carlier, M. Guignard, L. Bourgeois, C. Delmas, *Inorg. Chem.* **2014**, *53*, 11197.

[142] Y. H. Jung, A. S. Christiansen, R. E. Johnsen, P. Norby, D. K. Kim, *Adv. Funct. Mater.* **2015**, *25*, 3227.

[143] Z.-Y. Li, R. Gao, L. Sun, Z. Hu, X. Liu, *J. Mater. Chem. A* **2015**, *3*, 16272.

7 List of Acronyms

Al-Air/O_2	aluminium air/oxygen battery
BSE	back scattering electron
CE	counter electrode
CV	cyclic voltammogram/cyclic voltammetry
DC	direct current
e.g.	*exempli gratia,* for example
ect.	*Et cetera*, and so on
EDS	energy dispersive spectoscropy
EIS	electrochemical impedance spectroscopy
FWHM	full width half maximum
i.e.	*id est*, that is
ICP-OES	Inductively Coupled Plasma Optical Emission Spectroscopy
IL	ionic liquid
Li-AirO_2	aluminium air or oxygen battery
LIB	lithium-ion battery
LSV	linear sweep voltammetry
MH	metal hydride alloy
NCO	P2-Na_xMnO_2
NIB	sodium-ion battery
Ni-Cd	nickel-cadmium battery
Ni-MH	nickel-metal hydride battery
NMO	P2-Na_xMnO_2

NMP	N-Methyl-2-Pyrrolidone
OCV	open circuit voltage
Pb-acid	lead-acid battery
PipGuan-TFSI	*N,N,N',N'*-tetramethyl-*N'',N''*-pentamethylene-guanidinium bis(trifluoromethylsulfonyl)imide
PVDF	polyvinylidene difluoride
RE	reference electrode
SEI	solid electrolyte interphace
SEM	scanning electron microscopy
SHE	standard hydrogen electrode at standard conditions of 298.15 K, 1 atm H_2 pressure and an effective concentration of 1 mol dm^{-3} H^+ in aqueous solution
TEM	transmission electron microscopy
TFSI	bis(trifluoromethylsulfonyl)imide
TGA	thermogravimetric analysis
UPS	uninterruptible power sources
vs.	*versus*
WE	working electrode
XRD	X-ray diffraction
XRF	X-ray fluorescence
Zn-Mn	zinc-carbon battery
Zn-OH	alkaline Battery

8 List of Figures

Figure 1. Schematic of an insertion type battery (cathode: Na_xMnO_2[26], anode: $Na_6V_{10}O_{28}$[27]). A prototype of this full-cell configuration has been published by Hartung *et. al.*.[27] 10

Figure 2. Number of publications for the specific search term: "sodium ion batter*" in the Scopus database, including truncation (*). # until date of search: 22.11.2015. 11

Figure 3. Schematic illustration of the different stacking types for MO_6 octahedra (grey). Orange spheres correspond to sodium atoms, red to oxygen atoms. For reasons of clarity only the Na_e are indicated 16

Figure 4. Geometric relation of a crystal structure and incident X-rays. 21

Figure 5. Generation of X-rays in a copper anode. 22

Figure 6. Set-up of an optical light microscope (LM), a transmission electron microscope (TEM), and a scanning emission microscope (SEM). The indicated detectors are secondary electron (SE), energy dispersive spectroscopy (EDS), back scattered electron (BSE) and a fluorescence screen. 24

Figure 7. Different ways of electron – matter interaction. 25

Figure 8. X-ray – matter interaction resulting in fluorescence. 27

Figure 9. Schematic circuit of a three (left) and a two (right) electrode cell. (A): current-, (V): potential measurement. 30

Figure 10. Illustration of a coin-cell setup: 1) bottom part, 2) cathode electrode, 3) separator, 4) Na-metal anode, 5) spacer, 6) spring, 7) top part (schematic adapted from [117]). 31

Figure 11. Applied current pulse and subsequent relaxation period in an actual GITT experiment performed under Chapter 4.4. ΔEt is the total transient voltage change for the current pulse and ΔEs is the steady state voltage change of the step. 34

Figure 12. Left side shows the applied voltage scan; right side the respective voltammogram. 35

Figure 13. Electrical circuit scheme equivalent for interfacial electrochemical reactions, where R_Ω corresponds to the Ohmic resistance, C correspond to the double layer capacitance and R_{CT} corresponds to the charge transfer resistance. 36

Figure 14. *In operando* experiment of $Na_{0.6}MnO_2$ flakes. New occurring reflections are indicated in red. Note: Electrochemical cell for in operando X-ray diffraction measurements on a conventional X-ray diffractometer 63

9 List of Tables

Table 1. Overview of different battery chemistries and their theoretical energy density.[13] (*Calculated for a maximum of x = 0.5; y = 0)..... 6

Table 2. Cycling performance overview of state of the art P2-type materials. Estimated values are denoted with (*)..... 103

10 List of Publications

(13 Publications, 3 Conference Talks)

Submitted Mar 2016 — Han-Yi Chen, **Nicolas Bucher**, Steffen Hartung, Jochen Friedl, Huei- Ping Liou, Linlin Li, Chia-Liang Sun, Ulrich Stimming, Madhavi Srinivasan "A multi-walled carbon nanotube core with graphene oxide nanoribbon shell as anode material for sodium ion batteries" *Adv. Energy Mater.* **2016**, *under review*

Mar 2016 — **Nicolas Bucher**, Steffen Hartung, Joseph B. Franklin, Anna M. Wise, Linda Y. Lim, Han-Yi Chen, Johanna Nelson Weker, Michael F. Toney, Madhavi Srinivasan "P2-$Na_xCo_yMn_{1-y}O_2$ (y = 0, 0.1) as Cathode Materials in Sodium-Ion Batteries – Effects of Doping and Morphology To Enhance Cycling Stability" *Chem. Mater.* **2016**, DOI: 10.1021/ acs.chemmater.5b04557

Mar 2016 — Steffen Hartung, **Nicolas Bucher**, Joseph B. Franklin, Anna M. Wise, Linda Y. Lim, Han-Yi Chen, Johanna Nelson Weker, Maria-E. Michel-Beyerle, Michael F. Toney, Madhavi Srinivasan "Mechanism of Na^+ Insertion in Alkali Vanadates and its Influence on Battery Performance" *Adv. Energy Mater.* **2016**, DOI: 10.1002/aenm.201502336

Aug 2015 — Steffen Hartung, **Nicolas Bucher**, Ramona Bucher, Madhavi Srinivasan "Electrochemical cell for *in operando* X-ray diffraction measurements on a conventional X-ray diffractometer" *Rev. Sci. Instrum.* **2015**, 86, 086102-1 – 3

Aug 2015 — Steffen Hartung, **Nicolas Bucher**, Han-Yi Chen, Rami Al-Oweini, Sivaramapanicker Sreejith, Parijat Borah, Yanli Zhao, Ulrich Kortz, Ulrich Stimming, Harry E. Hoster, Madhavi Srinivasan "Vanadium-based polyoxometalate as new material for sodium-ion battery anodes" *J. Power Sources* **2015**, 288, 270 - 277

Sep 2014 — Jan Szabo, Kerstin Karger, **Nicolas Bucher**, Gerhard Maas "Derivatives of the triaminoguanidinium ion, 3. Multiple *N*-functionalization of the triaminoguanidinium ion with isocyanates and isothiocyanates" *Beilstein J. Org. Chem.* **2014**, *10*, 2255–2262

Jul 2014 — Steffen Hartung, **Nicolas Bucher**, Vivek Sahadevan Nair, Cheah Yan Ling, Yuxi Wang, Harry E Hoster, Madhavi Srinivasan "Sodium Vanadium Oxide - a New Material for High-Performance Symmetric Sodium Ion Batteries" *ChemPhysChem.* **2014**, *15* (10), 2121–2128

May 2014 — **Nicolas Bucher**, Steffen Hartung, Arun Nagasubramanian, Yan-Ling Cheah ,Harry E. Hoster, Madhavi Srinivasan "Layered Na_xMnO_{2+z} in Sodium Ion Batteries–Influence of Morphology on Cycle Performance" *ACS Appl. Mater. Interfaces* **2014**, *6* (11), 8059–8065

Apr 2014	Vivek Nair, Sivaramapanicker Sreejith, Parijat Borah, Steffen Hartung, **Nicolas Bucher**, Yanli Zhao, Madhavi Srinivasan" Crystalline $Li_3V_6O_{16}$ Rods as High-Capacity Anode Materials for Aqueous Rechargeable Lithium Batteries (ARLB)" *RSC Adv.* **2014**, *4*, 28601-28605
Mar 2014	Vanchiappan Aravindan, Wong Chui Ling, Steffen Hartung, **Nicolas Bucher**, Srinivasan Madhavi "Carbon-Coated $LiTi_2(PO_4)_3$: An Ideal Insertion Host for Lithium-Ion and Sodium-Ion Batteries" *Chem. Asian J.***2014**, *9*, 878–882
Feb 2014	**Nicolas Bucher**, Steffen Hartung, Vivek Sahadevan Nair, Cheah Yan Ling, Yuxi Wang, Harry E Hoster, Madhavi Srinivasan "$Na_2V_6O_{16}$ – a New Material for Sodium-ion Battery Cathodes and Symmetric Full Cells", oral contribution *Singapore Battery Meeting*, **2014**, Singapore
Nov 2013	**Nicolas Bucher**, Steffen Hartung, Arun Nagasubramanian, Yan-Ling Cheah ,Harry E. Hoster, Madhavi Srinivasan "Layered Na_xMnO_{2+z} in Sodium Ion Batteries–Influence of Morphology on Cycle Performance", oral contribution *The 7th Asian Conference on Electrochemical Power Sources*, **2013**, Osaka, Japan
Jul 2013	**Nicolas Bucher**, Steffen Hartung, Maria Arkhipova, Denis Yu, Philipp Kratzer, Gerhard Maas, Madhavi Srinivasan, Harry E. Hoster "A novel Ionic Liquid for Li Ion Batteries–Uniting the Advantages of Guanidinium and Piperidinium Cations" *RSC Adv.* **2014**, *4*, 1999-2003
Apr 2013	**Nicolas Bucher**, Steffen Hartung, Maria Arkhipova, Phillip Kratzer, Irina Gocheva, Harry E Hoster, Madhavi Srinivasan, Gerhard Maas "Guanidinium based Ionic Liquids as new Electrolytes for Energy Storage Systems", oral contribution *13th Topical Meeting of the International Society of Electrochemistry*, **2013**, Pretoria, South Africa
Jan 2013	**Nicolas Bucher**, Steffen Hartung, Irina Gocheva, Yan L. Cheah, Madhavi Srinivasan, Harry E. Hoster "Combustion-Synthesized Sodium Manganese (Cobalt) Oxides as Cathodes for Sodium Ion Batteries" *J Solid State Electrochem* **2013,** *17,* 1923-1929
Apr 2012	**Nicolas Bucher**, Jan Szabo, Iris M. Oppel, Gerhard Maas "Derivatives of the Triaminoguanidinium Ion, 1. Synthesis, Crystal and Molecular Structures of 1,2,3-Tris-(benzylamino)guanidinium Salts", *Z. Naturforsch.* **2012**, *67b*, 631-642